High Temperature Ceramic Membrane for CO_2 Reuse and Syngas Production

By

Le Chang

B.S. Mechanical Engineering

University of Illinois at Urbana-Champaign, 2011

SUBMITTED TO THE DEPARMENT OF MECHANICAL ENGINEERING

IN PARTIAL FULFILLMENT OF THE REQUIREMENTS FOR THE

DEGREE OF

MASTER OF SICENCE IN MECHANICAL ENGINEEARING

at the

MASSACHUSETTS INSTITUTE OF TECHNOLOGY

September 2013

Author .....
Department of Mechanical Engineering
August 8, 2013

Certified by .....
Ahmed F. Ghoniem
Ronald C. Crane ('72) Professor
Thesis Supervisor

Accepted by .....
David E. Hardt
Chairman, Department Committee on Graduate Theses

High Temperature Ceramic Membrane for CO_2 Reuse and Syngas Production

by

Le Chang

Submitted to the Department of Mechanical Engineering
on August 8, 2013, in partial fulfillment of the
requirements for the degree of
Master of Science in Mechanical Engineering

Abstract

In recent years, membrane based technologies have attracted much attention thanks to their simplicity in reactor design. The concept proposed is to use mixed ionic-electronic conducting membrane (MIEC) in CO_2 reuse and syngas production by taking the advantage of low quality energy resource. The membrane under investigation is a $La_{0.9}Ca_{0.1}FeO_{3-\delta}$ (LCF) perovskite membrane. Membranes with perovskite structure have shown high oxygen permeability and 100% oxygen selectivity. These membranes have also been demonstrated to produce H_2 by water splitting. During the reaction, H_2 is produced on the membrane feed side and the resultant oxygen is transported to the membrane sweep side, thus shifting the water splitting reaction towards hydrogen production. Under the same principle, CO is also likely to be produced from CO_2 dissociation in the membrane reactor. The produced H_2 can be further processed with CO_2 to yield hydrocarbon fuel. In this way, the usual products of combustion, H_2O and CO_2, can be reused by the membrane reactor.

In this thesis, a literature review of the existing technologies of hydrogen production and CO_2 reduction is presented. The reviewed technologies are compared to our proposed method for water splitting and CO_2 reuse. A bench scale reactor was built to test the LCF membrane in order to understand the characteristics of the membrane. Tests are also done for the proposed water splitting reaction. The reactor design, experimental set-ups and experimental procedures are also presented in this thesis. The results of the experiments are analyzed and future work for improving the membrane reactor is proposed.

Thesis Supervisor: Ahmed F. Ghoniem
Title: Ronald C. Crane ('72) Professor

Acknowledgements

I would like to thank my advisor, Professor Ahmed Ghoniem, for his guidance and support during my two years at MIT. His advice is invaluable for the success of my master's research.

I would also like to thank Dr. Patrick Kirchen for his guidance and support. He has always been a great resource of help and advice. I won't be able to complete the construction of the reactor without his wisdoms.

I would like to thank my colleagues Dr. Jongsup Hong, Anton S. Hunt, Tianjiao Chen and Xiaoyu Wu. I am grateful that I can work with these excellent people and have their support when I needed. I also want to acknowledge Xiaoyu Wu for his help in the SEM and Auger Electron Microscopy images of the membrane.

I would like to thank Mruthunjaya Uddi and Santosh Shanbhogue for their help and support to the experiments.

I would like to thank all my colleagues in the reacting gas dynamics laboratory and my friends at MIT for the wonderful two years of my master's program.

I would like to thank my research sponsors Shell and KFUPM.

Finally, I would like to thank my parents and my family for their love and support.

Contents

ABSTRACT 3

ACKNOWLEDGEMENTS 4

NOMENCLATURE 7

CHAPTER 1. INTRODUCTION 10

1.1 Motivation 10

1.2 Ion Transport Membrane 11

1.3 ITM CO_2 reuse 12

CHAPTER 2. LITERATURE REVIEW 16

2.1 OTM water splitting 17

2.1.1 OTM Materials 18

2.1.2 Water splitting membranes experiments 20

2.1.3 Carbon Stability 24

2.2 Electrolysis 27

2.2.1 Alkaline Water Electrolysis 27

2.2.2 Solid Oxide Electrolyzers 29

2.2.3 PEM Electrolyzers 35

2.2.4 Photoelectrolysis 42

2.3 Methane Reforming Technologies 44

2.3.1 CO_2 reforming of methane 44

2.3.2 Steam methane reforming 54

2.3.3 Combined Steam Dry Reforming of Methane 56

2.4 Comparison of Hydrogen Production Technologies 58

2.4.1 Calculation of Membrane Reactor Efficiency 58

2.4.2 Comparison with Methane Reforming Methods 67

2.4.3 Comparison with Water-Splitting Methods 68

2.5 Reactor Design 71

CHAPTER 3. EXPERIMENT 78

3.1 Experiment Set-up 79

3.1.1 Reactor Design 79

3.1.2 Connections 84
3.1.3 Instrumentation and Data Acquisition 87
3.1.4 Sealing 90

3.2 Experimental Methodology and Procedures **91**
3.2.1 Sealing 91
3.2.2 Inert Gas Permeation Experiments 92
3.2.3 Fuel Assisted Permeation Experiments 92
3.2.3 Water Splitting Experiments 93

3.3 Methodology of Analysis **94**

3.4 Error Analysis **96**

CHAPTER 4. RESULTS AND DISCUSSION **99**

4.1 Sealing **99**

4.2 Inert Gas Permeation Experiments **103**

4.3 Hydrogen Sweep Experiments **123**

4.4 Water Splitting Experiments **126**

4.5 Post-experiment Investigations **132**

CHAPTER 5. CONCLUSIONS AND FUTURE WORK **137**

REFERENCES **140**

Nomenclature

Abbreviation

CGO	Gadolinium-doped CeO_2
DRM	dry reforming of methane
HER	hydrogen evolution reaction
HHV	higher heating value
ITM	ion transport membrane
LCF	$La_{09}Ca_{0.1}FeO_{3-\delta}$
LHV	lower heating value
LSCF	$La_{0.7}Sr_{0.3}Cu_{0.2}Fe_{0.8}O_{3-\delta}$
MIEC	mixed ionic-electronic conducting
OER	oxygen evolution reaction
OTM	oxygen transport membrane
PEM	proton exchange membrane
PEME	proton exchange membrane electrolysis
sccm	standard cubic centimeters per minute
SDRM	steam-dry reforming of methane
SFC	$SrFeCo_{0.5}O_x$
SOE	solid oxide electrolyser
SRM	steam reforming of methane

Symbols

C_i	molar concentration of gas species i
c_p	heat capacity
D_v	bulk diffusivity
D_{12}	gas diffusivity of a binary system
E_a	activation energy
E_{rev}	reversible voltage

E_{th}	thermoneutral voltage
e^{-1}	electron
F	faraday constant
ΔG	change in Gibbs free energy
g_m	mass transfer coefficient
ΔH	change in enthalpy
h_i	enthalpy of gas i, including heat of formation
h_{i_f}	heat of formation for gas i
J_i	flow of gas i per second per unit area of membrane
K_{ex}^{sweep}	sweep side surface exchange rate
K_{ex}^{feed}	feed side surface exchange rate
k_r	reverse surface reaction rate
k_f	forward surface reaction rate
L_c	membrane critical thickness
$\dot{m}_i$	mass flow rate of gas i
Nu	Nusselt number
P_{O2}^{sweep}, P''_{O2}	sweep side oxygen partial pressure
P_{O2}^{feed}, P'_{O2}	feed side oxygen partial pressure
Pr	Prandtl Number
Q_i	flow rate of gas i
R	ideal gas constant
R^2	coefficient of determination
Re	Reynolds number
ΔS	change in entropy
Sc	Schmidt number
t	tolerance factor
V_o^{oo}	oxygen vacancy
σ_i	ionic conductivity
σ_e	electronic conductivity

ε_c electrolysis current efficiency

ε_{th} electrolysis cell efficiency

ε_E electrolysis electrical efficiency

Chapter 1. Introduction

1.1 Motivation

Over the past century, fossil fuels have brought human society enormous progress thanks to their high energy content, ease of access and large reserve over the globe. The use of fossil fuels accounted for over 82% of the world's energy consumption in 2011 according to EIA[1]. The primary sources of fossil fuels are coal, petroleum and natural gas. Despite their high energy content, the combustion of fossil fuel produce large amounts of CO_2, which is often emitted directly into the atmosphere. In 2010, 30.3G metric ton of carbon dioxide was emitted into the atmosphere globally [2]. In the U.S., 96.7% of its CO_2 emission was from combustion of fossil fuel according to EPA's report in 2013[3]. Among the CO_2 emissions from fossil fuel, 40% are from electricity generation. Thus a small alleviation of CO_2 emission from power generation can result in huge reduction of CO_2.

Carbon dioxide is one of the major greenhouse gases, accounting for 84% of the total greenhouse emission, which also includes methane, nitrous oxide and fluorinated gases [3]. Due to the large amount of CO_2 emission since the onset of the industrial revolution, the global average temperature has increased by 0.8℃ over the past century. Besides the increased temperature, the global warming also brings more frequent extreme weather, higher sea level, more super storms, etc. As a result, 191 countries and states including the Europe Union have signed the Kyoto Protocol in an effort to reduce global warming. Political efforts like this have created regulations that pose higher cost on hydrocarbon combustion, usually in the form of carbon tax for power plants. Thus, the reduction or the recycle of CO_2 combustion will not only bring environmental benefits but also economic benefits for energy production.

1.2 Ion Transport Membrane

In this report, we propose a method for CO_2 recycling using mixed ionic-electronic conducting (MIEC) ceramic membranes, or simply, ion transport membranes (ITM). The types of ITM are many. The membrane used in this thesis is a $La_{0.9}Ca_{0.1}FeO_{3-\delta}$ (LCF) perovskite membrane. Perovskite membranes are commonly known for their mixed conducting properties due to the perovskite structure and their high oxygen permeability.

Experiments on certain perovskite membranes such as $SrFeCo_{0.5}O_x$ (SFC) [4], $BaCo_xFe_yZr_{1-x-y}O_{3-\delta}$[5] and $Co_xFe_yZr_{0.9-x-y}Pd_{0.1}O_{3-\delta}$[6] have all demonstrated their ability to dissociate water at high temperature. For example, a 0.95mm thick $SrFeCo_{0.5}O_x$ demonstrated hydrogen production rate of 7.4μmol/s/cm^2 at 900°C. The water splitting phenomenon come from the ITM's oxygen transporting property. As depicted in Figure 1-1, during water splitting, water vapor is fed to the feed side of the membrane at the temperature around 900°C to 1000°C, and dissociate into oxygen ions and hydrogen gas:

$$H_2O(g) + V_o^{oo} + 2e^- \rightarrow O^{2-} + H_2(g) \quad (1\text{-}1)$$

In equation (1-1), V_o^{oo} is oxygen vacancy in the membrane and e^- represents electron. Water is split and hydrogen is produced near the membrane surface on the feed side. Oxygen ions are adsorbed into the membrane lattice oxygen vacancy and diffuse to the sweep side of the membrane under oxygen ion concentration gradient. When diffused oxygen ions reach the surface of the sweep side, they are carried away by inert sweep gases or react with a fuel. To enhance the oxygen gradient that favors diffusion of oxygen ions, fuel can be used to consume the oxygen on the sweep side. In this thesis, we propose using CH_4 as the fuel:

$$O^{2-} + CH_4 \rightarrow CO + 2H_2 + V_o^{oo} + 2e^{-1} \quad (1\text{-}2)$$

Equation (1-2) is the desired reaction in the sweep side. If insufficient methane is present at the sweep side, complete combustion occurs and H_2O and CO_2 are produced. Complete combustion of methane should be avoided, since the aim is to reduce CO_2 in the products and produce syngas, which is a mixture of CO/H_2. As Reaction (1-2) is slightly exothermal, some heat can be provided to the reaction on the feed side. The details of this process will be discussed in later chapters.

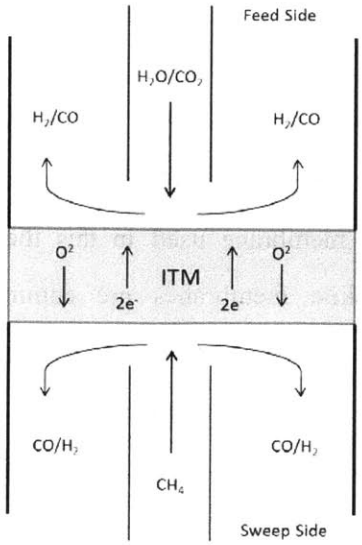

Figure 1-1 ITM water splitting. The gas on the feed side and sweep side may be balanced by inert gas.

1.3 ITM CO_2 reuse

In the proposed membrane reactor, a mixture of H_2O and CO_2, the typical composition of exhaust gas, is fed to the reactor, as shown in Figure 1-2. Ideally, most H_2O and CO_2 dissociate into H_2 and CO so that the outlet gas is H_2, CO, H_2O and CO_2, where H_2O can be easily condensed. The dissociation of CO_2 is described in Reaction (1-3). The resulting $H_2/CO/CO_2$ gas can go through a water-gas shift reaction (Reaction (1-4)) to produce more CO.

$$CO_2(g) + V_o^{oo} + 2e' \rightarrow O^{2-} + CO(g) \quad (1\text{-}3)$$

$$CO_2 + H_2 \leftrightarrow CO + H_2O \qquad \Delta H = 41.1 kJ/mol \quad (1\text{-}4)$$

On the other hand, the gas can simply be stored into a storage tank for further use as syngas, as shown in Figure 1-1. The key step in the reactor is to produce hydrogen through water splitting as described in Reaction (1-1). With hydrogen available, CO_2 can be processed into higher hydrocarbons. Moreover, hydrogen is by itself a valuable source of clean energy. Thus the primary focus of the thesis is water splitting using the membrane.

Most of the hydrogen produced in industry is through methane steam reforming. Alternatively, CO_2 can be used with methane through dry reforming to produce hydrogen and CO. The two reactions are described below:

Methane steam reforming: $CH_4 + H_2O \leftrightarrow CO + 3H_2 \quad \Delta H = 41.1kJ/mol$ (1-5)

CO_2 methane reforming: $CH_4 + CO_2 \leftrightarrow 2H_2 + 2CO \quad \Delta H = 247.4kJ/mol$ (1-6)

As can be seen in Figure 1-3, the feed gases of the reaction are CH_4 and H_2O or CO_2. The temperature of the reaction is 800°C to 900°C and the pressure is up to 30bar. The methane and H_2O/CO_2 is catalytically reformed into syngas and water in a packed bed reactor. The reforming reaction can produce high conversion ratios according to the equilibrium. Shown in Figure 1-4 is the CO_2 methane reforming equilibrium under different temperatures. At 950°C, about 99% of CH_4 is converted into H_2. Figure 1-5 shows the equilibrium of steam reforming. At 950°C, about 99% of CH_4 is converted into H_2. Commercially, the conversion rate of methane can be about 90% using these two technologies. In the case of hydrogen production, a water gas shift reactor is used to produce more hydrogen.

To test the membrane hydrogen production and compare it to methane steam reforming, a disk membrane reactor is constructed as shown in Figure 1-1. The gas-tight reactor is separated into two chambers by the LCF disk membrane. The feed side of chambers is where the oxygen concentration is high, and the sweep side is where the oxygen concentration is low. In the case of a water splitting experiment, the water vapor and the carrier gas is fed to the membrane feed side. The inert gas is fed to the sweep side to decrease the oxygen concentration. In the case of a fuel assisted experiment, fuel like H_2 or CH_4 is added to the sweep side to further enhance the water splitting rate. Besides water splitting experiments, oxygen permeation tests were also done to understand the characteristics of the membrane.

The second section of this thesis discusses existing water splitting and hydrogen production technologies. The third section presents the experimental setup, the experimental procedures, and the methods that were used to test and analyze the LCF membrane. The fourth section presents the results and discussions of the experiments. The fifth section summarizes the findings from the experiments and future work that needs to be done to improve the feasibility of the membrane CO_2 reuse concept.

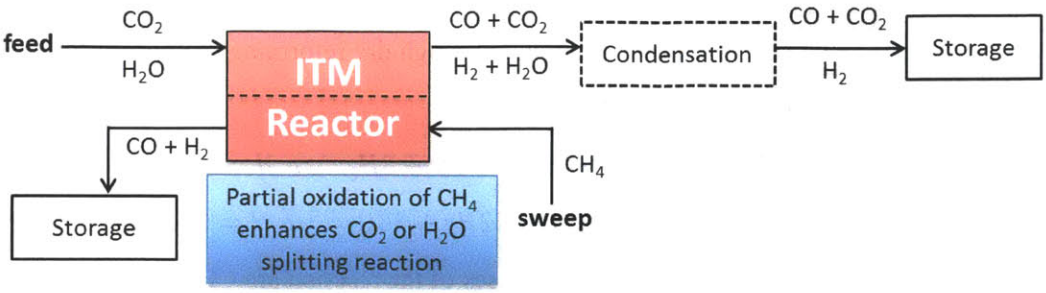

Figure 1-2. The concept of the CO_2 reuse system.

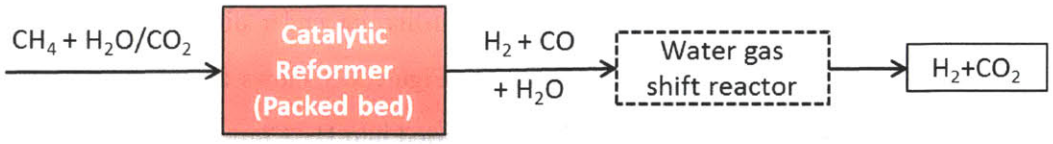

Figure 1-3. Conventional catalytic steam or dry methane reformer

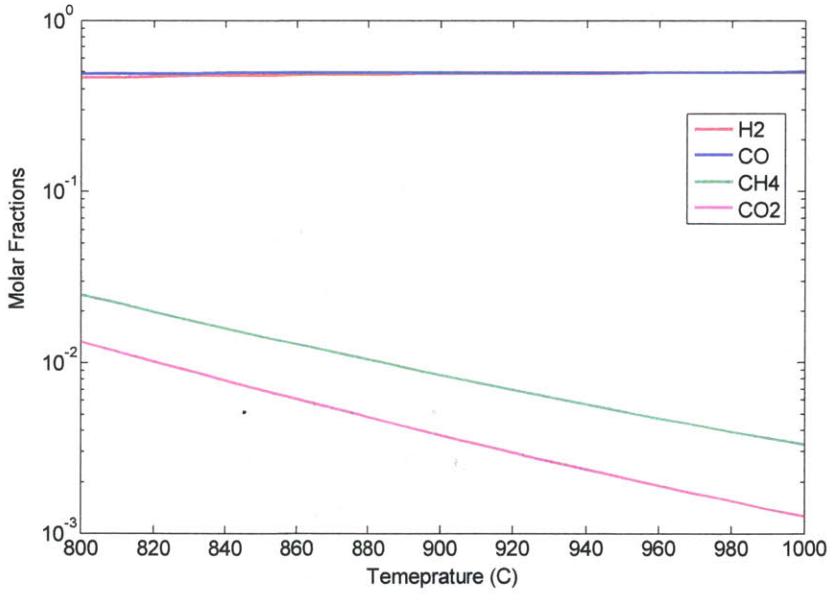

Figure 1-4. Equilibrium of CO_2 methane reforming

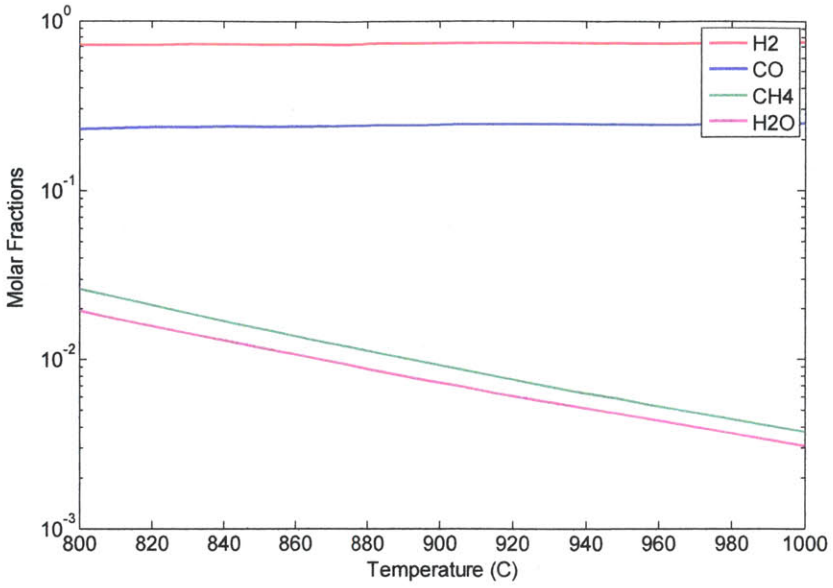

Figure 1-5. Equilibrium of steam methane reforming

Chapter 2. Literature Review

The key reaction in the proposed CO_2 reuse system is water splitting. The recycling of CO_2 becomes possible when water vapor is dissociated into hydrogen and oxygen and oxygen separated from the rest of the gas. Thus an appropriate water splitting method is needed for the system. The available choices include thermolysis, thermochemical cycles, alkaline water electrolysis, proton exchange membrane electrolysis, solid oxide electrolysis, photoelectrolysis and high temperature mixed conducting membrane. Thermolysis requires a temperature higher than 1200°C because of the low equilibrium hydrogen production rate, and as a consequent complex thermo-management and high temperature material. On the other hand, thermochemical cycles require more complicated reactor design and production process. Thus only alkaline water electrolysis, proton exchange membrane electrolysis, solid oxide electrolysis, photoelectrolysis and high temperature mixed conducting membranes will be reviewed in this report.

Membranes are composed of special materials that can selectively transport ions through. The membranes we will discuss here include oxygen ion transport membranes and proton transport membranes. Compared to water electrolysis that uses electricity, membrane reactors only require heat, which is a much less costly energy source. And unlike thermolysis, the temperature typically required by membranes is around 1000°C, which is a much lower quality heat compared to over 2000°C that is required by thermolysis. Thus, the requirement for material and thermal management is much less restrict in the case of membrane reactors. Last but not least, the design of a membrane reactor is much simpler than that of thermochemical cycles, which also has a strict requirement for thermal management.

On the other hand, the steam methane reforming and CO_2 methane reforming are more mature methods of hydrogen production. The success of these two technologies is due to the simplicity of the reaction and relatively low energy requirement. A comparison of the efficiencies between the existing technologies and the proposed membrane reactor will be presented near the end of this chapter. Several possible reactor designs are also reviewed in the last section of this chapter.

2.1 OTM water splitting

Oxygen transport membrane (OTM) is a promising candidate for water dissociation. An OTM is a special type of ITM that transports oxygen through the membrane. The material used to construct an OTM can vary. The most promising candidates for OTM material are perovskite membrane and dual-phase membrane. In the case of OTM's, H_2O can be dissociated near or at the surface of the membrane and oxygen ions are transported through the membrane. The overall dissociation reaction is shown as follow:

$$H_2O \rightarrow H_2 + \frac{1}{2}O_2 \qquad \Delta H = 241.82kJ/mol \qquad (2\text{-}1)$$

The equilibrium of reaction (2-1) under increasing temperatures is plotted in Figure 2-1. As shown in the figure, dissociation only happens at a significant extent at temperatures above 2000°C. At 900°C, only 0.00053% mole fraction of hydrogen is present under equilibrium. With the help of an OTM, oxygen is transported to the other side of the membrane, thus the dissociation reaction is shifted to the right-hand side. Near the surface of the feed side of the membrane, H_2 is produced. This process can happen at a temperature of above 800°C when OTM is involved in the reaction.

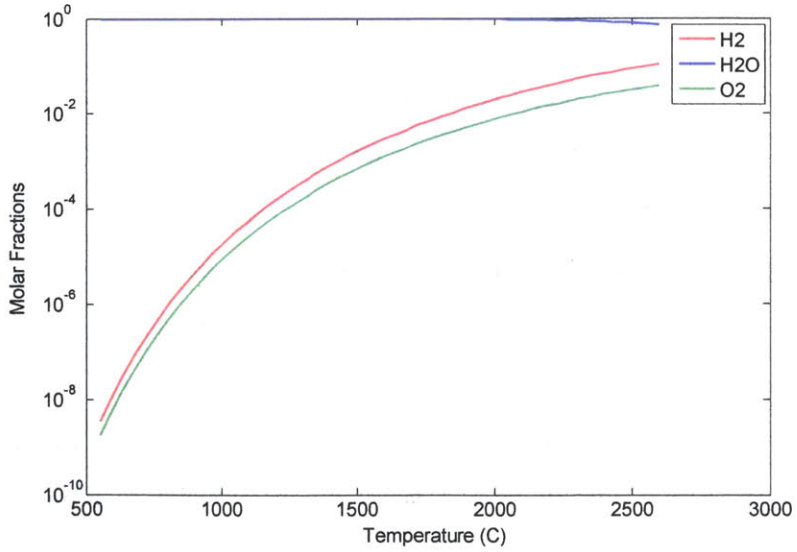

Figure 2-1. Water dissociation equilibrium

2.1.1 OTM Materials

Perovskite

A perovskite membrane is composed of the crystal structure a composition of $ABO_{3-\delta}$, as shown in Figure 2-2. . The typical perovskite materials are $CaTiO_3$ and $SrTiO_3$ [7]. In such a structure, the A site is occupied by a large ion that is usually a rare earth metal and the B site is occupied by a medium size ion that is transition metal. The δ in the formula represents the oxygen deficiency. This oxygen deficiency produces oxygen vacancies that are responsible for oxygen ion transports. The transient metal in the B site can have more than one state of valence so that it can donate free electrons, providing electronic conductivity. Equipped with ionic and electronic conductivities, perovskite membranes can permeate oxygen ions in the presence of an oxygen gradient. While membranes with pure perovskite material are not of much use for our purpose, a membrane made with defected perovskite material is an ideal candidate as a mixed ionic-electronic conducting (MIEC) membrane.

Nevertheless, with just $ABO_{3-\delta}$ structure, the membrane may not have enough electronic conductivity or ionic conductivity. Fortunately, it was found that the perovskite structure is very tolerant for substitutions, as long as Eq. (4) is satisfied:

$$0.8 < t = \frac{R_A + R_O}{\sqrt{2}(R_B + R_O)} < 1 \qquad (2\text{-}2)$$

The relation in Eq. (2-2) is proposed by Goldschmidt[8], who is known to have founded the science of crystal. t is called the tolerance factor , and R_A, R_B, R_O are the ion radii of A, B and the oxygen ion, respectively. By doping the compound with different dopants, the oxygen transporting properties of the OTM can be modified, creating compounds with the formula $A_{1-x}A'_xB_{1-y}B'_yO_{3-\delta}$. In particular, if A site is doped with lower valence cations, the ionic conductivity of the membrane can be improved [9]. Partial substitution of A site cation with higher valence metal ions increases the phase stability, while compromising some ionic conductivity [7]. And partial substitution of A site with ions of higher radii increases both the chemical and structural stability of the membrane although it may decrease the oxygen permeability [7]. The typical occupants for A site are Ba, Sr, La, Ga, Cr, Na, Gd, Pr, etc. The typical B site occupants are Co, Fe, Zn, Ni, Cu, Mn etc.

Because of perovskite's special property, the membrane acts as a closed circuit, with

negatively charged oxygen ions moving from feed side to the sweep side of the membrane and electrons moving from the sweep side to the feed side. Thus no external wiring is needed in the case of an OTM process. And unlike the reaction in an electrolyser, which is driven by an electric potential, the reaction in an OTM is driven by the oxygen gradient. Thus in order to initiate the reaction, the gas in the feed side must have greater oxygen partial pressure than the sweep side. Usually this is accomplished by feeding inert gas to the sweep side to carry away the permeated oxygen or a fuel such as methane balanced by inert gas to consume oxygen on the sweep side.

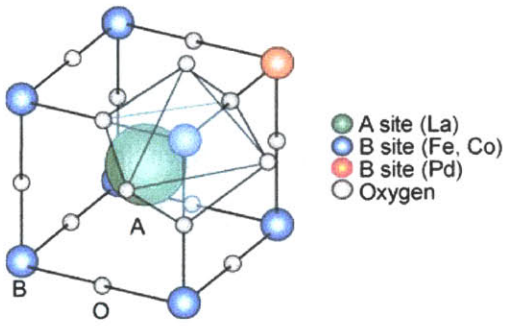

Figure 2-2. Perovskite Structure [55]

Dual-phase composite membrane

Another type of membrane that could be used as an oxygen transport membrane is a dual-phase composite membrane. Unlike a perovskite membrane that has ionic and electronic conductivity from its structural property, a dual-phase membrane takes ionic and electronic conductivities from two different materials. A metal phase or sometimes a ceramic phase with high electronic conductivity provides free electrons while a ceramic phase provides the oxygen ion vacancies. Because the membrane is composed of two different materials, they can be carefully chosen to bare high electronic and ionic conductivity at the same time. Moreover, dual-phase composite membranes have good chemical and mechanical stability under high oxygen gradient [52]. Noble metals such as Pt, Ag can be used as the electron conductor phase[7]. Sometimes Ni, In or Pd are also chosen. Two often used oxygen ion conductors are yattria stabilized zirconia and bismuth oxide, which demonstrate high oxygen

conductivity. Some other high oxygen permeable oxides like $Ce_{0.8}Gd_{0.2}O_{2-\delta}$ and $Ce_{0.8}Sm_{0.2}O_{2-\delta}$ have also been used as oxygen ionic conductors [53]. Ceramics like $La_{0.8}Sr_{0.2}CrO_{3-\delta}$, and $La_{0.8}Sr_{0.2}MnO_{3-\delta}$ can also provide electronic conductivity in order to replace noble metal.

2.1.2 Water splitting membranes experiments

Because of OTM's oxygen permeability, it is able to promote water dissociation by shifting reaction (2-1) to the right side. Several researchers have investigated the water dissociation characteristics of OTM. In 1995, Naito and Arashi[10] used a ZrO_2-TiO_2-Y_2O_3 mixed conducting membrane to produce hydrogen from water splitting. The experiment tested a tubular membrane as illustrated in Figure 2-3, with the feed gas inside the tube and the sweep gas outside. They used Ar to carry water vapor on the feed side and a H_2/CO_2 mixture to produce oxygen deficiency on the sweep side. Their membrane reached its highest hydrogen production rate of 0.47μmol/s/cm^2 at 1956K. The low hydrogen production rate was because of the low oxygen ionic conductivity and the large thickness (2mm) of the tubular membrane.

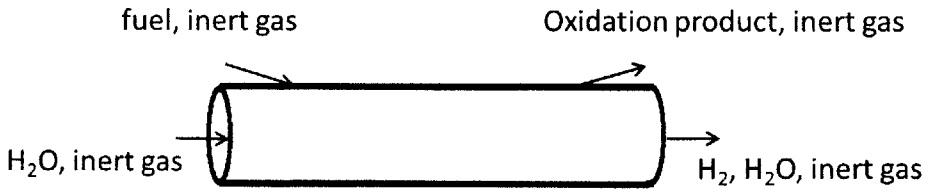

Figure 2-3. Tubular membrane

The performance of the water splitting membranes was improved by using better material. Balachandran et al[11] investigated the water splitting ability of a dual phase mixed conducting membrane that was made of Gadolinium-doped CeO_2 (CGO) and nickel, using a

disk membrane setup as in Figure 1-1. A H_2/He mixture was used as the fuel to establish the oxygen gradient, and the operating temperature of the mixed conducting membrane was 700°C-900°C. By changing the membrane thickness, it was observed that the transition from bulk diffusion limited reaction to surface kinetics limited reaction happened at around 0.5mm for the particular material. The best hydrogen production rate 6ml/min/cm^2 (4.5μmol/s/cm^2) was achieved using a 0.13mm membrane with porous support at 900°C. The feed gas was 49%H_2O balanced N_2 and the sweep gas was 80% H_2 balanced He. Later in 2007, Balachandran et al[12] published another paper on water dissociating membrane. Two types of membranes were tested: one was CGO/Ni mixed conducting membrane but with finer microstructure, the other was a perovskite membrane $SrFeCo_{0.5}O_x$ (SFC2). Using the same feed gas and sweep gas as in his previously published experiment, the best hydrogen production rate was 10ml/min/cm^2 (7.4μmol/s/cm^2) using 1mm thick SFC2 at 900°C. It was found that the hydrogen production rate was limited by bulk diffusion for the SFC2 membrane. The performance of CGO/Ni membrane was significantly improved with a finer microstructure, but was less productive than SFC2 at temperatures higher than 850°C. SFC2 had a high hydrogen production rate because of its high oxygen permeability. Unfortunately, SFC2 is not chemically stable especially under CO_2 rich environment. The Co and Sr content of the material makes it unstable.

Investigations on other perovskite membranes rather than SFC2 have also been done, but the hydrogen production rates of these materials are not as good. A. Evdou et al[13] tested a 3mm thick $La_{0.3}Sr_{0.7}FeO_{3-\delta}$ perovskite membrane using disk membrane set up as in Figure 1-2. The membrane demonstrated a 0.0145ml/cm^2/min (0.01μmol/s/cm^2/) rate of hydrogen production using CO as the reducing gas at 860°C. The much lower rate may be caused by the larger thickness of the LSF membrane compared to the SFC2 membrane as well as CO being a weaker reductant compared to hydrogen. Moreover, the La substitution of Sr also lowered the oxygen permeability because La was more stable but with lower conductivity than Sr. In a more recent report by Balanchandran et al [94], $La_{0.7}Sr_{0.3}Cu_{0.2}Fe_{0.8}O_{3-\delta}$ membrane was used for water splitting in an effort to improve the stability of previously tested SFC2 membrane by La substitute. The configuration was a tubular membrane as illustrated in Figure 2-3. The tubular LSCF membrane was 30μm thick on porous support. It achieved a

hydrogen production rate of 11ml/min/cm^2 (0.95μmol/s/cm^2) under 150sccm N_2 with 0.49atm vapor pressure and 99.5%CO balanced CO_2 sweep gas. They reported that the tubular LSCF membrane was stable during a 80hr of operation at 900°C. Although La and Cu substitute lowered the hydrogen production rate, the stability of the membrane was improved significantly.

Another perovskite membrane $BaCo_xF_yZr_{1-x-y}O_{3-\delta}$ was tested by Heqing Jiang, et al[14]. Jiang's membrane was tubular. The outer diameter was 1.1mm and the inner diameter was 0.76mm. The sweep gas which contained 20% CH_4, 78% He and 2% Ne was fed to the outside of the tubular membrane. The feed gas, which contained 60% H_2O and 40% He was fed to the inside of the tube. The total flow rate of both feed and sweep gas was 50sccm. The experiment found an increasing hydrogen production rate with temperature, which was expected. It was also found that by adding a Pd containing porous BCFZ layer to the outer surface improved the hydrogen production rate from 0.7ml/min/cm^2 (0.52μmol/s/cm^2) to 2.1ml/min/cm^2 (1.56μmol/s/cm^2) at 950°C.The paper explained that the increased flux was caused by the catalytic activity of the Pd toward methane oxidation, so that the oxygen gradient was further increased by the catalytic coating of Pd porous layer.

A research done by Wang et al[15] investigated a dual-phase mixed conducting membrane $Gd_{0.2}Ce_{0.8}O_{1.9-\delta} - Gd_{0.08}Sr_{0.88}Ti_{0.95}Al_{0.05}O_{3\pm\delta}$. During high temperature, $Gd_{0.2}Ce_{0.8}O_{1.9-\delta}$ (GDC) functioned mainly as an oxygen ionic conductor and $Gd_{0.08}Sr_{0.88}Ti_{0.95}Al_{0.05}O_{3\pm\delta}$ (GSTA) functioned mainly as an electronic conductor. Two types of membranes were fabricated, one was 1.2mm thick self-supported membrane and the other was thin membrane (45μmm and 25μmm) supported on porous substrates made of the same materials. In the experiment, the reactor temperature was controlled at 900°C and the flow rates of both feed and sweep gas was 400sccm. By varying the fuel concentration (H_2) in the sweep side and steam content in the feed side, they recorded the area specific hydrogen flux (μmol/s/cm^2) versus $(1/\sqrt{P_{O2}^{sweep}} - 1/\sqrt{P_{O2}^{feed}})$ plot and applied to the following equations:

$$J_{o2} = \frac{(\frac{K_r}{K_f})(1/\sqrt{P_{O2}^{sweep}} - 1/\sqrt{P_{O2}^{feed}})}{\left(\frac{1}{K_{ex}^{sweep}}\right)+\left(\frac{2L}{D_v}\right)+\left(\frac{1}{K_{ex}^{feed}}\right)} \quad (2\text{-}5a)$$

$$K_{ex}^{swep} = k_f\sqrt{P_{O2}^{sweep}} \quad (2\text{-}5b)$$

$$K_{ex}^{feed} = k_f\sqrt{P_{O2}^{feed}} \quad (2\text{-}5c)$$

Here, J_{O2} is the oxygen flux, which corresponds to J_{H2} hydrogen production rate by a factor of 2. K_{ex}^{sweep} and K_{ex}^{feed} are the sweep side and feed side surface exchange rate respectively, and the inverse of them are surface exchange resistances. $2L/D_v$ is the oxygen bulk diffusion resistance and the oxygen partial pressures $P_{O2}^{permeat}$ and P_{O2}^{feed} were calculated from the sweep side and feed side outlet gas content and reaction equilibrium constants near each side of the membrane. This equation assumed that the gas concentrations measured from the outlet gases is similar to the gas concentrations near the membrane surfaces, which is true under high flow rates. Equation (2-5a) demonstrates how the three resistances affect the oxygen flux under the oxygen partial pressure gradient. Here the D_v, K_r, and K_f, are bulk diffusivity, reverse surface reaction constant and forward surface reaction constant respectively. The magnitudes of these three basic membrane parameters depend on the temperature according to:

$$k = Ae^{-E_a/RT} \quad (2\text{-}6)$$

Where A is pre-exponential constant, E_a is the activation energy and R is gas constant.

By manipulating the terms the equation, one can come to the following equation:

$$J_{O2} = \frac{D_V k_r (P_{O2}^{\prime 0.5} - P_{O2}^{\prime\prime 0.5})}{2LK_f (P_{O2}^{\prime} P_{O2}^{\prime\prime})^{0.5} + D_V (P_{O2}^{\prime 0.5} + P_{O2}^{\prime\prime 0.5})} \quad (2\text{-}7)$$

Where $P_{O2}^{\prime}$ and $P_{O2}^{\prime\prime}$ represent P_{O2}^{feed} and $P_{O2}^{permeate}$ respectively. From the data collected in Wang et al's experiment, it was concluded that while the thick self-supported membrane had dominant bulk diffusion resistance, the thin membranes (25μmm and 45μmm) were under the combined effect of bulk diffusion and surface resistances. The highest hydrogen flux was found to be 7.5μmol/s/cm^2 (11ml/min/cm^2) for the 25μmm membrane and about 0.6μmol/s/cm^2 (0.88ml/min/cm^2) for the thick self-supported membrane.

Research on water dissociation membranes show that much work still needs to be done to increase the hydrogen production rate and to understand the water dissociation reactions near the membrane surfaces. The challenge is to produce thinner membranes with higher mixed ionic-electronic conductivity and higher surface reaction rate but at the same time high

chemical and mechanical stability to sustain in the operating environment. The task is not easy, but using chemically stable material on porous support is the direction most researchers are heading. Doping materials like Pd, Ni can also be used to improve the surface reaction rate with CH_4.

Table 2-1. List of existing water splitting OTM's.

Membrane	T °C	Thickness (mm)	Feed	Sweep	Hydrogen Flux (ml/min/cm^2)	Hydrogen Flux (umol/s/cm^2)	Ref.
GDC-GSTA	900	0.025	Ar/H_2O/0.2%H_2	H_2/Ar/3%H_2O	11	7.5	[15]
CGO/NiO	900	0.25	N_2/H_2O	H_2/He	10	7.4	[12]
$SrFeCo_{0.5}O$	900	0.95	N_2/H_2O	H_2/He	10	7.4	[12]
LaSrCuFeO	900	0.03	N2/H_2O	99%CO/CO_2	11	0.95	[94]
BaCoFZrO	950	0.17	He/H_2O	CH_4/He/Ne	2.1	1.56	[14]
ZrO_2-TiO_2-Y_2O_3	1683	2	Ar/H_2O	H_2/CO_2	0.62	0.47	[10]
$La_{0.3}Sr_{0.7}FeO_{3-\delta}$	860	3	Ar/H_2O	CH_4/He	0.0145	0.01	[13]

2.1.3 Carbon Stability

Another issue that concerns most OTM, especially perovskite membranes, is carbon stability. A site rare-earth metals like Sr and Ba are prone to form carbonate layers, and B site metals like Co and Fe tend to form Fe_3O_4 and CoO [54]. These chemical instabilities are detrimental to the oxygen permeation flux. Since CO_2 is used in the feed gas of the proposed reactor, it is important to consider the chemical stability of various materials in CO_2 rich environment.

It has been observed that an A site substitution with higher valence cation in perovskite membrane improves the chemical stability although sacrificing the oxygen permeability [7]. Cations like La, Ti, Cr, Ga are more stable than Ba and Sr, though Sr containing perovskites are known to have high oxygen permeability. Figure 2-4 and 2-5 show the experiments done by Tan et al[54]. The feed gas was air while the sweep gas was CO_2/He. It can be seen from the graphs that although the La containing SCF membrane, $La_{0.6}Sr_{0.4}Co_{0.8}Fe_{0.2}O_{3-\delta}$ demonstrates decaying performance with increasing CO_2 content in sweep gas, the oxygen permeation never goes to zero. For Ba containing SCF, The oxygen flux quickly decays after

increasing amount of CO_2 in the sweep gas. Thus, with a larger La substitution, higher stability is expected.

The B site metal also contributes to stability issues by forming oxides. It has been observed that by substituting the B site with higher radii atoms can improve the stability of the membrane, although decreasing the oxygen flux. Figure 2-6 shows the results of an oxygen permeation experiment done by Schulz et al [55] where CO_2/N_2 was used as the sweep gas. The test was done on $SrCo_{0.48}Fe_{0.12}Ti_{0.4}O_{3-\delta}$ (SCFT414), $SrCo_{0.64}Fe_{0.16}Ti_{0.2}O_{3-\delta}$ (SCFT612), and $SrCo_{0.72}Fe_{0.18}Ti_{0.1}O_{3-\delta}$ (SCFT711). It can be observed from the figure that increasing the amount of Ti decreases the oxygen flux. However, when compared with the BSCF reference membrane, a higher stability is evident. Luo et al[56] compared the oxygen flux and stability of various OTM's under CH_4 fuel assisted oxygen permeation. It can be concluded from the comparison that substituting Ba-containing perovskite membrane with Ni, Ti, and Zr increases the stability, since the covalent radius of Zr (175pm) is larger than Ti (160om) and that of Ti is larger than Ni (124).

K.Efimov et al[107] showed that $La_{1-x}Ca_xFeO_{3-\delta}$ (x=0.4-0.6) had high stability when CO_2 was used as the sweep gas. Comparing literature results, the $La_{0.9}Ca_{0.1}FeO_{3-\delta}$ (LCF) membrane used in this thesis have a relatively high stability under carbon rich environment, though it shows lower oxygen permeation rate than membranes such as SFC.

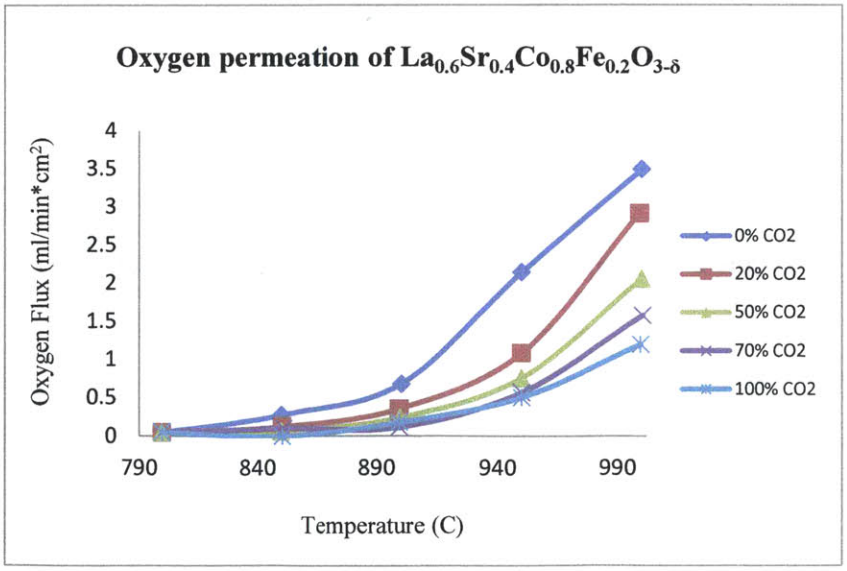

Figure 2-4. Oxygen permeation flux of LSCF membrane under increasing CO_2 content in sweep gas.

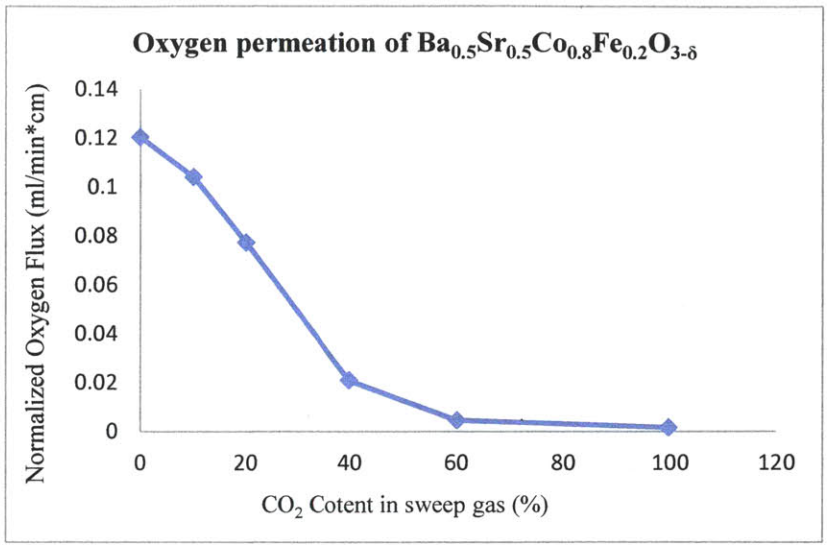

Figure 2-5. Oxygen permeation flux of BSCF membrane under increasing CO_2 content in sweep gas.

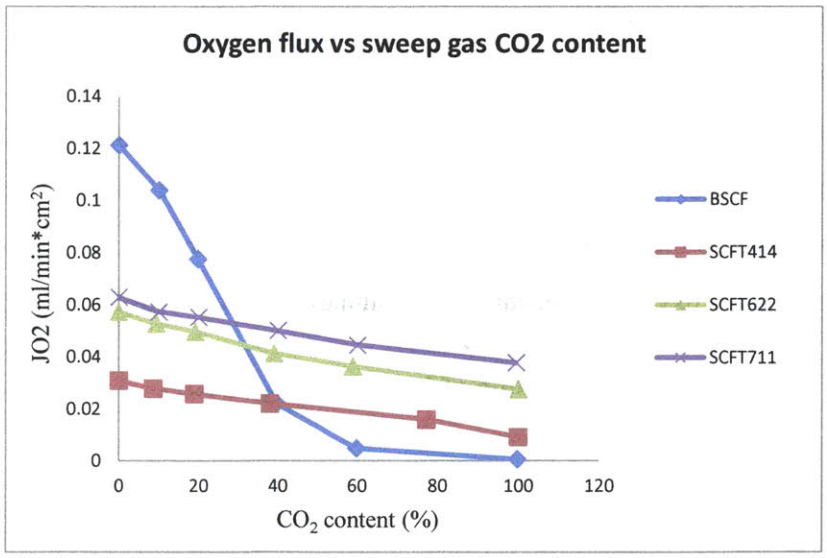

Figure 2-6. Comparison of oxygen flux for varying Ti content.

2.2 Electrolysis

The traditional way to produce hydrogen is through electrolysis. Compared to high temperature water dissociation membranes, which use heat as the sole energy source, water electrolysis utilizes electricity and sometimes heat as well. As long as the electricity comes from a renewable energy source such as wind power or nuclear energy, the electrolysis hydrogen production is considered a clean energy method of hydrogen production.

At the moment two electrolysis methods are mature: The first one is alkaline water electrolysis, in which liquid water is used as the hydrogen source. The second one is PEM electrolysis, in which liquid water is also used as the hydrogen supplier and the electrolyte is a proton exchange membrane (PEM).

Two other electrolysis hydrogen production methods are high-temperature electrolysis and photoelectrolysis, which are still under development, but are promising technologies. In high-temperature electrolysis, the electrolyte is solid oxide membrane, and water vapor is used as the hydrogen supply. High temperature water electrolysis is more of a hybrid reaction, where energy is from both heat and electricity. In photoelectrolysis, voltage from photovoltaic cells is used to drive the water dissociation. There have been some progress recently in photoelectrolysis, but it still suffers from high cost and low efficiency. Although traditional alkaline water electrolysis is a more common and developed technology, this section will mainly focus on high temperature electrolysis and PEM electrolysis, due to their similarity to the membrane reactor proposed in terms of membrane facilitated water dissociation.

2.2.1 Alkaline Water Electrolysis

Water electrolysis has been a traditional way of producing hydrogen from water. The method was discovered in the nineteenth century and has become a mature technology to produce hydrogen in industry since the mid-20th century [16]. The idea is to use electrical power to supply the energy needed in water dissociation. A water electrolysis unit consists of

an anode, a cathode, an electrolyte, a diaphragm and a power supply. The dissociation of water is achieved by applying a DC voltage across the anode and the cathode, which enables the following reactions occur under the potential:

Cathode: $2H^+(l) + 2e^- \rightarrow H_2(g)$ (2-8a)

Anode: $2OH^-(l) \rightarrow \frac{1}{2}O_2(g) + H_2O(l) + 2e^-$ (2-8b)

The electrodes are in direct contact with the electrolyte. Since usually KOH and NaOH solutions are used as the electrolyte, the electrodes must have good corrosion resistance and high conductivity [17]. Usually Ni is selected for its good conductivity and corrosion resistance as well as the relatively low cost compared to noble metal [16]. The diaphragm is a barrier that separates the hydrogen and oxygen but does not disturb ionic transport [18]. Like the electrodes, the diaphragm must be corrosion resistant, and it must have low ionic resistance to avoid limiting the reaction rate, thus polymers are often used.

The thermodynamics of the electrolysis follow these rules:

$$\Delta G = \Delta H - Q_h = \Delta H - T\Delta S$$

(2-9)

$$\Delta G = nFE_{rev} \quad (2\text{-}10)$$

$$\Delta H = nFE_{th} \quad (2\text{-}11)$$

where ΔG is the Gibbs free energy, Q_h is thermal energy, which is the product of the operational temperature and the entropy change, ΔH is the change of enthalpy of the reaction, n is the mole of electrons transferred during the reaction, F is the Faraday constant, E_{rev} is reversible voltage and E_{th} is thermoneutral voltage. E_{th} is the reaction voltage that is required if all the energy of reaction is from electricity, which is 1.48V at 25°C. The reversible voltage required by Gibbs free energy change is 1.23V at 25°C. With higher temperature, the Gibbs free energy requirement decreases while the enthalpy change increases, thus less voltage is required and more heat is used by the electrolyzer at higher temperature.

When alkaline water electrolysis was first commercialized, asbestos was used as the diaphragm, but was gradually replaced by polymers due to its toxic effects. Polymers such as perluorosulphonic acid, arylene ether and polytetrafluoroethylene are becoming more popular

diaphragm materials [16]. Steel has traditionally been used as the electrodes, but it has low alkaline corrosion resistance. To compensate this drawback of steel, Nickel and Noble metals are used to coat or replace steel. Due to its low cost, Ni has been more popular as the electrode material than noble metal. As for the electrolyte, KOH has been by far the most popular material used.

Since the alkaline water electrolysis uses liquid water as the hydrogen source rather than high temperature vapor, it will not be discussed in further detail in this thesis.

2.2.2 Solid Oxide Electrolyzers

Solid oxide electrolyzer (SOE) is the electrolyzer used for high temperature electrolysis (HTE). They are built using the same material as solid oxide fuel cells (SOFC) and work on the reverse mode of SOFC. At the cathode, steam is fed to the surface and the following reaction takes place:

Cathode: $H_2O + 2e^- \rightarrow H_2 + O^{2-}$ (2-12)

The oxygen ion is transported to the anode through the electrolyte driven by the potential applied across the two sides of the electrolysis. At the anode, the following reaction takes place:

Anode: $O^{2-} \rightarrow 2e^- + \frac{1}{2}O_2$ (2-13)

The minimal voltage, or the reversible voltage, required by Gibbs free energy change to drive this reaction is 0.91V at 1000°C [19][20], which is much lower than 1.23V that is required at 25°C. Assuming that the hydrogen production current is 1A and the total resistance of the electrolyzer is 1Ω, the minimal electrical energy required for room temperature water electrolysis is $1A \cdot 1.23V + 1\Omega \cdot (1A)^2 = 2.23W$ while the energy required for high temperature electrolysis at 1000°C is $1A \cdot 0.91V + 1\Omega \cdot (1A)^2 = 1.91W$. On the other hand, the themoneutral voltage increases by a small amount with increasing temperature. At 1000°C, the thermal neutral voltage of an electrolyzer is about 1.5V. So the percentages of dissociation energy that must come from electricity can be calculated by E_{rev}/E_{th}, which come to 1.23V/1.48V=83% and 0.91V/1.5V=61% for low and high temperature electrolyzers

respectively. Thus, with higher temperature, more of the energy required by water dissociation is taken from heat and less electricity is required. In addition, at high temperature, the electronic resistance is lower [16], so that high temperature electrolyte can save even more energy.

The electrolyte commonly used in SOE electrolyzer is Y_2O_3-stabilized ZrO_2 (YSZ). The anode is usually composed of the same material as electrolyte but doped with Ni or noble metal such as Pt to prevent thermal stress and catalyze the reaction at the same time. The cathode is often made of $LaMnO_3$ while doped with metal such as Pt, Ni, Sr [22]- [26]. Nearly all the research on HTE proposed using electricity and heat produced by nuclear plants, as the heat from cooling liquid of the nuclear reactor is readily available at a high temperature [22]-[26].

The reaction in terms of Gibbs free energy can be expressed by the following reaction:

$$\Delta G = \Delta G_o + RTln(\frac{P_{H_2}P_{O2}^{\frac{1}{2}}}{P_{H2O}}) \tag{2-14}$$

Where ΔG is the Gibbs free energy change, ΔG_o is the Gibbs free energy change in a reference temperature. R is the gas constant; T is the temperature; P_{H2}, P_{H2O} and P_{O2} represent partial pressure of hydrogen and steam on the cathode, and partial pressure of O_2 on the anode respectively.

According to Eq. (2-10) and Eq. (2-14), the Faraday law, the Gibbs free energy can be expressed in terms of reversible voltage across the electrolyser:

$$E = E_o + \frac{RT}{2F} ln\left(\frac{P_{H_2}P_{O2}^{\frac{1}{2}}}{P_{H2O}}\right) + \eta \tag{2-15}$$

Where E is the open-cell potential. E_o is the potential at reference state, 1.23V at 25°C. F is the Faraday constant and η is overpotential caused by reasons such as resistance in the circuit, resistance interconnections, activation energy barrier, shortage of steam concentration, etc[22].

The overpotential η is a useful term to look at when considering the efficiency of the SOEC in terms of voltage. Another often-used concept in SOEC is current efficiency, which gives insight to the efficiency of the current usage:

$$\varepsilon_c = \frac{n_{H2}/2F}{I*N} \tag{2-16}$$

Where I is the current in a cell unit, N is the number of cell units connected in series, n_{H2} is the hydrogen production rate in moles per second, and F is faraday constant unity. The current efficiency looks at how efficiently the electric current is used in the cell to produce hydrogen. Ideally, all the current should be used to produce hydrogen, making the current efficiency unity. The current efficiency is usually close to unity for a reasonably operated system. The loss of current efficiency comes from back permeation of gases, low ion conductivity or low proton conductivity.

The energy efficiency is usually defined as the higher heating value of the hydrogen produced over the energy used during the reactions:

$$\varepsilon_{th} = \frac{HHV*J_{H2}}{IE} = \frac{E_{th}}{E} \tag{2-17a}$$

$$\varepsilon_E = \frac{G*J_{H2}}{IE} = \frac{E_{rev}}{E} \tag{2-17b}$$

Where Q is hydrogen production rate in mole/s. ε_{th} is the cell efficiency calculated based on high heating value of hydrogen, and it can also be calculated based on the cell voltage and thermalneutral voltage if the current efficiency is close to 100%. ε_E is the electrical efficiency, which can be calculated from the Gibbs free energy or the actual and thermalneutral voltage if the current efficiency is close to 100%. The cell efficiency ε_{th} defined in (2-17a) can have a value larger than one in high temperature electrolysis, because part of the energy to split water comes from heating and is not taken into account by this definition. By tuning the operating voltage, high temperature electrolysis can operate at high efficiency but relatively low production rate or vice versa.

In the early 1980s, Doenitz et al [23][24] tested a tubular solid oxide electrolyser in which the electrolyte was composed of yattria(Y_2O_3)-stabilized zirconia (ZrO_2)(YSZ). The anode was nickel-containing YSZ and the cathode was strontium-doped $LaMnO_3$. Argon was used as the carrier gas of the steam and air was used as the sweep gas. The electrolyte was about 0.3mm thick, the anode was about 0.25mm thick and the cathode was about 0.1mm thick. Both of the cathode and the anode were made porous for better surface reaction. The electrolyser cell was able to achieve a current density of 370mA/cm^2 at 997°C and 1.32V. This rate corresponds to a hydrogen production rate of 2.55ml/min/cm^2 (1.73μmol/s/cm^2).

Depending on the operating temperature, the author estimated the cell could operate at up to 61.5% ε_E according to the efficiency definition in Eq. (2-17b).

Much recent experiments on a similar tubular SOE were conducted by Hino et al[22] at temperatures of 850°C, 900°C and 950°C. The cathode was made of $LaCoO_3$, the electrolyte was made of YSZ and the anode was made of Ni-doped YSZ. Argon was used as the carrier gas of the steam and air was used as the sweep gas. The maximum hydrogen production rate increased from 0.4ml/min/cm^2 at 850°C and current density of 108mA/cm^2 to 0.73ml/min/cm^2 at 950°C and current density of 131mA/cm^2. The correlation between temperature, current density and production rate predicted a production rate of 2.53ml/min/cm^2 at 997°C and 370mA/cm^2, which agreed well with that of Doenitz[23][24]. The author also observed increase in electrical efficiency ε_E with increasing temperature, which is well predicted by the thermodynamics according to Eq. (2-9). Even though the electrolyser achieved a reasonable hydrogen production rate, the current efficiency ε_C was quite low, around 51% at the highest production rate at 950°C, and the electrical efficiency ε_E was only 36 % as a result. The loss in current may have been caused by low oxygen ionic conductivity according to the author.

Researchers in Idoha National Lab also tested a solid oxide electrolysis unit [25]. The configuration was a cross flow planar cell. The electrolyte was made of scandia-stabilized zirconia (ScSZ), the anode was made of strontium-doped manganite, and the cathode was made of nikel-zirconia cermet with a Ni coating on the outside surface. Air was used as the sweep gas and a mixture of nitrogen, hydrogen and steam was used as the feed gas. The electrolyser reached a hydrogen production rate of 2.34ml/s/cm^2 (1.6μmol/s/cm^2) at 800°C. According to the 1.4V cell voltage reported at 900°C, the electrical efficiency ε_E was 65%.

Schefold et al[27] ran a 4000hr test on a solid oxide electrolyser cell stack at 820°C under a current density of 0.4A/cm^2 at 98% current efficiency ε_C as defined in Eq. (2-16). They observed a voltage degradation of 2% per 1000hr during the 4000hr operation. The electrolyser cell they used was a bit different in that the cathode was made using a doped perovskite $La_{0.6}Sr_{0.4}Co_{0.2}Fe_{0.8}O_3$ instead of $LaCoO_3$. Between the cathode and electrolyte was an $Y_{0.2}Ce_{0.8}O_{1.9}$ protective layer. The electrolyte was a 90μm YSZ, and the anode was a 40μm thick layer of Ni-doped CGO. The feed side of the electrolysis was fed with humidified

hydrogen and the sweep side was fed with air. The result showed a maximum hydrogen production rate of 2.76ml/s/cm^2 (1.88μmol/s/cm^2). The electrical efficiency was 77% at 820°C. The degradation during the 4000h test was mostly due to instability at interconnection points.

Kim et at[29] tested a 3-cell flat-tubular SOEC stack. The tubular cells were NiO-YSZ (8mole% Y_2O_3 zirconia) anode supported. The cathode was made of $La_{0.8}Sr_{0.2}MnO_3$ coating, and the electrolyte was YSZ. The maximum hydrogen production rate achieved by this SOEC was 2.33ml/min/cm^2 (1.58μmol/s/cm^2). The operating condition was 750°C with H_2O/H_2/Ar as the feed gas and air as sweep the gas. They achieved a current efficiency ε_C of 97.61%. The results also indicated that by increasing the steam content, the electrolysis of water can be enhanced and the activation energy for water electrolysis at high temperature can be reduced. Because of this high electricity to hydrogen energy efficiency, they were able to produce hydrogen at a low electricity cost of 3.07kWh/m^3 H_2 at a relatively low temperature, which corresponded to 71% electrical efficiency ε_E at 750°C.

Xing et al[30] tested a promising new material for electrodes. $La_{0.75}Sr_{0.25}Cr_{0.5}Mn_{0.5}O_{3-\delta}$ powder was mixed with yttria stabilized zirconia on a 1:1 weight ratio to form a LSCM-YSZ cathode. The electrolyte was YSZ and the anode was prepared by a mixture of $La_{0.8}Sr_{0.2}MnO_{3-\delta}$ and YSZ according to a weight ratio of 1:1. The feed gas on the cathode side was 30sccm hydrogen with varying humidity and N_2 as the carrier gas. The results showed that the electrolyser can generate hydrogen at a rate of 9.35ml/min/cm^2 (6.36μmol/s/cm^2) at 850°C with a voltage of 1.6V and current density of 0.96A/cm^2. Although the high production rate is due to the high voltage level, calculations show that the electrolyser takes only 2.73kWh electricity to generate 1m^3 hydrogen, which is lower than most of the electrolysers using Ni based electrodes. At 850°C, the electrical efficiency ε_E was 58%. The efficiency was obtained assuming a 100% current efficiency and using a high voltage.

An even more interesting solid oxide electrolysis design was done by Tao et al[28]. They used a hybrid design of planar solid oxide fuel cell (SOFC) and solid oxide electrolysis cell (SOE) to produce hydrogen as well as electrical power. In the SOEC, fuel was fed to the sweep side to facilitate stronger drive for water dissociation. At the cathode of the SOE, water was dissociated into hydrogen and oxygen ions, as with traditional electrolysis. At the anode,

however, instead of air, syngas was fed as the sweep. Thus the following reactions took place at the anode:

$$H_2 + O^{2-} \rightarrow H_2O + 2e^- \quad (2\text{-}18)$$

$$CO + O^{2-} \rightarrow CO_2 + 2e^- \quad (2\text{-}19)$$

The electrolyte they used was the typical YSZ, fuel side electrode (anode for SOE) was Ni+YSZ two-phase mixture, and the oxygen supplying side (cathode for SOE) was composed of $LaSrCrMnO_3$. 20 layers of the planar cross flow fuel cell were used as the SOE, and 13 layers as SOFC, each of $100cm^2$ active area. In the SOE, a mixture of hydrogen and steam was used as the feed gas, and in the SOFC, air was used as the feed gas. For both SOFC and SOE, syngas was used as the fuel. Operating the hybrid system at 770°C, 35A, they achieved a net output of 130W electrical power. 125W from the SOFC was used in the SOE to produce hydrogen at 5.4ml/min, which is $2.7ml/min/cm^2$ ($1.83\mu mol/s/cm^2$), corresponding to 75% energy efficiency based on HHV of hydrogen. They also observed that at currents below 10A, both SOE and SOFC generated power. This research shows a promising future for solid oxide fuel cells where electricity generation can be combined with hydrogen production.

A comparison of the research and the highest hydrogen production rates as well as the efficiencies they obtained is listed in Table 2-2. The efficiency ε_{th} is calculated using Eq.(2-17a) according to the higher heating value of hydrogen and ε_E is calculated using Eq. (2-17b) according to the Gibbs free energy of water dissociation. For many electrolysers, the efficiency ε_{th} is higher than 100% because part of the energy for dissociation was supplied by environment heat and was not included in the energy consumption.

The option of solid oxide electrolysers looks attractive for high temperature applications, however, the cost estimated by researches can be as high as 1000$/kW [21]. Thus using the SOEs is still far from a mature technology. Furthermore, as can be seen from table 2-2, although the energy for water dissociation is compensated by heat, the electrical efficiency ε_E of most of the electrolysers is far less than 100%. This lower-than-expected electrical efficiency is largely due to overvoltage in the cells, which makes the cell voltage much higher than around 0.93V that is expected by reversible voltage at 900°C. Thus, further research is needed to improve the reactively of the SOE membrane, especially the catalytic materials in the anode and cathode.

Table 2-2. Comparison of high temperature solid electrolysis

Anode Electrolyte Cathode	T°C	Voltage (V)	Current Density (A/cm^2)	Hydrogen Production Rate ($umol/s\ cm^2$)	ε_c Eq (2-16)	ε_{th} Eq (2-17a)	ε_E Eq (2-17b)	Ref.
YSZ Y_2O_3+Zr/YSZ $LaMnO_3$	997	1.32	0.37	1.73	90.2%	104%	61.56%	[24]
Ni-YSZ YSZ LaCoO	950	1.31	0.13	0.35	51.9%	60%	36.28%	[22]
Y-ZrO_3 ScSZ LSM	900	1.4	0.38	1.94	98.5%	107%	65.43%	[25]
Ni-CGO $Y_{0.2}Ce_{0.8}O_{1.9}$ LSCF	820	1.22	0.4	2.04	98.4%	122%	76.94%	[27]
Ni+YSZ YSZ LSM+YSZ	750	1.3	0.32	1.58	95.2%	111%	71.44%	[29]
LSM-YSZ YSZ LSCM-YSZ	850	1.6	1.25	6.36	98.2%	93%	57.98%	[30]
Ni-YSZ YSZ $LaSrCrMnO_3$	770	1.29	0.35	1.82	100%	117%	75.11%	[28]

2.2.3 PEM Electrolyzers

Another popular method of water dissociation is proton exchange membrane (PEM) water electrolyers. It is considered a mature technology for hydrogen production because of its high efficiency and high hydrogen production purity.

The electrolyzer dissociates liquid water when a voltage difference is established across the proton exchange membrane, which acts as the electrolyte. Materials in the anode catalyze the water dissociation and the protons are transported through the membrane to the cathode,

where protons recombine with electrons to form hydrogen. The reaction on the anode side is often named oxygen evolution reaction (OER) because oxygen is formed at the anode during operation. On the other hand, the reaction on the cathode side is termed hydrogen evolution reaction (HER). In order to catalyze the reaction at low temperature, noble metal must be used in the electrodes because of the highly acidic environment. The OER electrode usually contains Ir, Ru, or their oxide; the HER electrode usually contains Pt. The use of noble metal in the electrodes is the reason why the PEM electrolyzers involve high capital cost. The third part of the electrolyser is the current collector. Current collectors are usually made of porous Ti. In some electrolysers, the electrode material is printed directly on the two sides of the PEM and carbon collectors are hot-pressed to the membrane electrode assembly (MEA), in other cases, the electrode materials are sprayed onto the current collectors, which then are hot pressed to the membrane.

Nafion is used as the material for proton exchange membranes in nearly all the researches and commercialized models. It is a synthetic polymer developed by DuPont in the late 1960's, with the chemical formula of $C_7HF_{12}O_5S{\bullet}C_2F_4$. During electrolysis, Nafion is fully saturated with water, and the water molecules are dragged across the membrane along with protons. Thus, at temperatures higher than 100°C, Nafion will loss conductivity due to dehydration [33]. The typical conductivity of a Nafion membrane ranges from 0.1 to 0.3 S/cm, which is higher than most materials. Due to its high conductivity as well as high thermal and chemical stability, Nafion remains almost the only choice for electrolyte [31]. However, because of its low operating temperature, most of the energy for PEM water dissociation must come from electricity. Besides, catalysts must be used in the anode and cathode to improve the chemical reactivity of the electrolyzer. These drawbacks increase the operating and capital costs of PEM electrolyzers. Research efforts are being made to find electrolytes with higher operation and chemical reactivity as well as cheaper manufacturing cost.

Alternative electrolyte materials are also under development. Sulfonated aromatic material membranes such as polyether ether ether keone (PEEK) and S-PSF membranes also depend on water to connect the sulfonic groups, so the operating temperature must be under the boiling point of water [32]. In addition, PEEK is highly soluble in water due to its high degree of sulfonation, which degrades its mechanical strength. Others material such as

polybenzimidazole (PBI) can use H_3PO_4 as the proton carrier and thus operate in temperatures higher than 180°C. However, both PEEK and PBI are less conductive than Nafion, with conductivity ten times lower [32]. Researches have shown that covalently cross-linking sulfonated polyether ether keone/tungstophosporic(CL-SPEEK/TPA) acid has higher thermal and mechanical stability because of the cross-linked structure. And the addition of TPA further improves the conductivity, which makes the CL-SPEEK/TPA reaches a conductivity of 0.128S/cm at 80°C[34], close to the lower end of Nafion conductivity range.

Another category of material that has the potential to replace Nafion is solid acids. They usually take the form of $M_xH_y(AO_4)_z$. Here M is alkali metal or NH_4 and A is S, Se, P or As. These materials have low proton conductivity at temperatures under 100°C but have satisfactory (10^{-4}-10^{-2}S/cm) conductivity at intermediate temperature of 150°C-300°C. The mechanism behind the proton conductivity enhancement at elevated temperature is still a subject under study. The highest conductivity measured with solid acid membranes was around 2.2E10^{-2}S/cm with CsH_2PO_4 using at 230°C [35]. RbH_2PO_4 also demonstrates a conductivity of 10^{-2}S/cm at 276°C [36]. Though this conductivity is still low compared to that of Nafion, they provide the possibility to operate water electrolysis at elevated temperatures, which lowers the use of electricity. Nevertheless, both the conductivity and mechanical property still need to be improved for solid acid membrane to become a mature technology [32].

Currently, the focus of research regarding PEM water electrolysis is to reduce the over-potential during operation. Ideally, the cell voltage should be 1.23V at 25°C to achieve a 100% electrical efficiency at 25°C according to Eq. (2.17b). The overpotential comes from electric resistances and the activation energy barrier of the surface reactions. During high current density operation, the over-potential can also be caused by mass transport limitations.

The biggest source of over-potential in the electrolyzer comes from the reaction on the anode side, where water is dissociated into protons and oxygen. The most commonly used catalytic materials for this reaction are iridium and ruthenium due to their chemical stability and high catalytic reactions. Kötz et al[35] tested alloys of Ru_xIr_{1-x} and pure ruthenium by voltammetry. The tests showed that with only Ru, RuO_4 formed quickly and hindered the reaction. With a small amount of Ir alloyed to the Ru, the oxidation of Ru was inhibited, and

the stability of the alloy increased with increasing Ir. However, the addition of Ir reduced the reactivity of the electrode and thus increased the over-potential. It is also known that IrO_2 is more stable than RuO_2 although the later has higher conductivity, thus the IrO_2 is the preferred material in making anode [36].

Rasten et al[36] tested a PEM electrolysis cell with IrO_2 electrode sprayed on the Nafion membrane as the anode and 10%Pt/Vulcan spayed on the other side as cathode. The cell achieved a voltage of 1.65V with $1A/cm^2$ current density at 80°C with total noble metal loading of $2.4mg/cm^2$. In PEM, production rate of hydrogen is controlled by the current. Thus the performance of PEM cells is evaluated by the cell potential under a standard current density of $1A/cm^2$. The 1.65V cell potential corresponds to 74.55% electrical efficiency according to the definition in Eq. (2-17b). Song et al[37] tested single cell electrolyzers with anodes made of different materials: Ru, Ir, RuO_2, IrO_2 and $Ru_{0.5}Ir_{0.5}O_2$; and the cathode made of 28%Pt/C. The results indicated that the oxides were more active than metal because of more active sites. Among these five anode materials, Ir was the most stable yet least active while Ru was the most active but had dramatic performance loss after only 400 voltammetry cycles. Their test on IrO_2 electrode showed 1.63V voltage at $1A/cm^2$, which was 78.5% electrical efficiency. The better performance and lower over-voltage compared to that of Rasten et al may be contributed to heavier noble metal deposition of $3mg/cm^2$ and $0.5mg/cm^2$ at anode and cathode respectively [37].

To further improve the performance and reduce the cost of the anode electrode, some researchers have tried doping RuO_2 and IrO_2 with Ta, Sn, Nb or Sb, which may enhance both the conductivity and the stability. Marshall et al[38] tested the anode electrode using $Ir_xRu_yTa_zO_2$ catalysts. The research showed that a Ru/Ir mixture had an increasing conductivity with increasing Ru contain up to 40mol% Ru. Tantalum can be added to the mixture up to 20mol% without significantly affecting the electrode performance. The best result was found using $Ir_{0.6}Ir_{0.4}O_2$ at the anode and 20wt%Pt/C at the cathode amounting to $2.1mg/cm^2$ total noble metal loading. The electrolysis cell could operate at only 1.567V with $1A/cm^2$ current density. Wu et al[39] demonstrated an electrolysis cell with RuO_2/SnO_2 mixture oxide as the anode. The RuO_2 powder was mixed with Sb doped SnO_2 (ATO) at a weight ratio of 1:4. The results demonstrated that the mixture could obtain a low voltage of

1.56V at 1A/cm^2 with 2mg/cm^2 RuO_2 loading. The inert ATO support material enhanced the electrode performance probably because of increased electron conduction and reduced agglomeration.

Recently, Kadakia et al[40] investigated the effect of doping Sn and Nb into IrO_2 catalyst. Nb_2O_5 was doped in place of Ta because it had similar properties as Ta_2O_5 but cheaper price. The electrode was made by loading 0.3mg/cm^2 $(Ir_{1-x}Sn_xNb_x)O_2$ onto Ti foils. Current density was measured as a function of increasing Sn/Nb contain under a constant voltage of 1.75V. The results showed that the electrode could tolerate a 60mol% addition of $(Sn,Nb)O_2$ without significant degradation in the conductivity and up to 80mol% addition with only 20% loss of current density at 1.75V. This result was a promising sight that substituting the noble metal in the anode with cheaper metal could largely reduce the cost of the electrode.

Besides doping the catalytic material with inert metals, improving the process of making the electrode can also help enhance the reactivity. Slavcheva et al[41] had tested electrolyzers with MEA prepared using reactive magnetron sputtering. IrO_2 was spurted onto 50nm Ti films to be prepared as thin film electrodes with thicknesses varying from 250nm to 1000nm. These electrodes were then hot pressed onto a Nafion membrane. The best performance was obtained using the 500nm thick film with only 0.2mg/cm^2 catalyst coating, showing a current density of 0.3A/cm^2 at 1.55V. Unfortunately, the research did not present tests with high current density (1A/cm^2), but the low catalyst coating showed hopes in future improvement with MEA assembly process.

Efforts have also been made to reduce the noble metal loading of the cathode. The conventional material for cathode catalyst is Pt, due to its stability in an acidic environment and its catalytic effect toward HER. Grigoriev et al[41] compared PEM electrolysis cells with electrodes made of 40wt%Pt and 40wt%Pd sprayed on carbon-supported nanoparticles (CSNs). The experiment showed that Pt was more efficient than Pd as the cathode catalyst. At 1A/cm^2 current density, the cell with Pt electrode had a voltage of 1.66V and that with Pd electrode had a voltage of 1.72V. Millet et al[42] tested boron-capped tris (glyoximato) cobalt complexes (Co(dmg)) and tungstosilicic acide hydrate (α-$H_4SiW_{12}O_{40}$) as the anode catalysts.. The Co(dmg) was absorbed onto a carbon surface (Vulcan XC-72) and mixed with 5wt% Nafion to form the electrode. Though the Co/Ir cell was much less efficient compared with

Pt/Ir electrolysis cell, it reached 80% electrical efficiency ε_E at 500mA/cm^2. At 1A/cm^2, the Co/Ir electrolyzer demonstrated a voltage of 2.4V while the voltage of Pt/Ir reference electrolyzer cell voltage was 1.79V. On the other hand, α-$H_4SiW_{12}O_{40}$ anode showed more promising results. An anode with 0.8mg/cm^2 α-$H_4SiW_{12}O_{40}$ loading obtained 1.81V cell voltage, which corresponds to 80% electrical efficiency ε_E and was very close to the performance of the reference Pt/Ir cell.

Another aspect of PEM electrolysis research focuses on high-pressure operation. The idea of high-pressure electrolysis is to reduce the total cost of producing hydrogen, as the energy needed for high-pressure hydrogen storage may be reduced by directly producing hydrogen at elevated pressure. Figure 2-4 shows the total power requirement with respect to increasing electrolysis pressure. It has been observed that the energy cost of moving the protons across a pressure gradient is smaller than that of a multi-stage compressor [43]. Medina et al [44] tested a stack electrolyzer prototype Giner Gs-10 provided by Giner Electrochemical Systems LLC at mid-high pressure. The anode was under atmospheric pressure while the cathode was at elevated pressure so that the protons were driven across the pressure gradient. The results showed that at 42°C and 1A/cm^2, the voltage per cell was 2.05V if the cathode pressure was 7 bar and was 2.2V if the pressure was 70 bar. Interestingly, by increasing the temperature to 58°C, the voltage at the 70 bar cathode decreased to 2.1V, which was very close to that at 7 bar and 42°C. Thus, the increased reactivity by increased temperature offset the decrease in efficiency. Marangio et al[45] calculated the optimal pressure for a 600 bar hydrogen storage under 0.79A/cm^2 current density. The optimal pressure was found around 30 to 45 bar due to a balance between electrolyzer power and compressor power. The optimal pressure decreased with increasing current density. These results show that high-pressure electrolysis can be a power saving method for commercialized hydrogen production.

Table 2-7 shows a summary of PEM electrolysis data collected from literature. The efficiency of the electrolyzers depends on the operating voltage of each cell and can be calculated according to Eq. 17 using the voltage information. It can be observed from the literature that most improvements in efficiency come from improvements in the anode catalysts. The efficiency can be chosen in an electrolyzer, where increasing the current

density increases the production rate but decreases the efficiency and vice versa. The drawbacks of PEM electrolyzer include dependence on electricity and high noble metal loading.

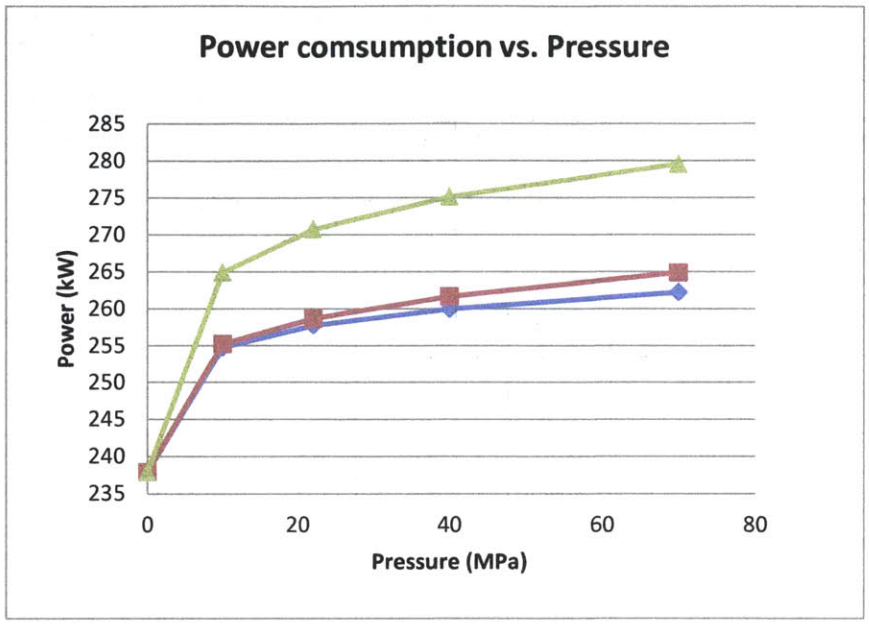

Figure 2-7, Power consumption of electrolysis for different hydrogen storage pressure. ♦-- High pressure with pater pump (balanced pressure). ■-- High pressure with water pump (unbalanced pressure). ▲—Atmospheric electrolysis plus compression

Table 2-3. Efficiency E is electricity efficiency, determined by Gibbs free energy of water dissociation. Efficiency is determined by HHV of hydrogen.

Anode	Cathode	Electrolyte	T (C)	Cell Voltage (V)	ε_{th} Eq (2-17a)	ε_E Eq (2-17b)	Ref.
IrO_2	10%Pt Vulcan	Nafion	80	1.65	89.70%	74.55%	[36]
$Ir_{0.6}Ru_{0.4}O_2$	20%Pt/C	Nafion 115	90	1.567	94.45%	78.49%	[38]
IrO_2	Pt/C	Nafion 112	80	1.63	90.80%	75.46%	[37]
$Ir_{0.5}Ru_{0.5}O_2$	Pt/C	Nafion 112	80	1.65	89.70%	74.55%	[37]
Ir	Pt/C	Nafion 112	80	1.72	86.05%	71.51%	[37]
Ru	Pt/C	Nafion 112	80	1.79	82.68%	68.72%	[37]
IrO_2 nano film	20%Pt/C	Nafion 117	80	1.83	80.87%	67.21%	[41]
Ir Black	Pt/Vulcan XC72	Nafion 115	90	1.7	87.06%	72.35%	[41]
Ir Black	Pd/Vulcan XC72	Nafion 115	90	1.67	88.62%	73.65%	[41]
Ir Black	Co(dmg)	Nafion 115	90	2.45	60.41%	50.20%	[42]
Ir Black	α-$H_4SiW_{12}O_{40}$	Nafion 115	90	2	74.00%	61.50%	[42]
20%RuO_2/ATO (SnO_2)	50%Pt/C	Nafion 212	80	1.56	94.87%	78.85%	[39]
Ir/Ru oxide	Pt Black	Nafion 117	50-60	1.98	67.27%-74.75%	55.91%-62.12	[45]

2.2.4 Photoelectrolysis

In practice, electrolysis can be powered using solar energy electricity from photovoltaic cells. A photoelectrolysis device combines the solar power conversion with water electrolysis by directly splitting water on a photoelectrode. Thus the voltage that drives dissociation comes directly from the photons hitting the electrode. This device is also called a photoelectrochemical (PEC) cell, and the photoelectrode can either be the cathode or the anode. In order to make the electrolyzer efficient, the band gap produced by the electrode must be lower than 2.2eV [19], and higher than 1.23eV in order for water dissociation to happen.

In order to catalyze water splitting on the surface, the electrode must be coated or doped

with some form of catalyst. The coating/doping is applied on the band gap semiconductors that absorb the sunlight and generate voltage. Many researchers prepare the electrode in tandem configuration, where several band gap semiconductors are stacked in series and each of them is specialized in absorbing light within a range of wavelength. This important electrode can be the cathode, in which case it is called photocathode; or it can be the anode, in which case it is called photoanode.

When a cathode is used for photoelectric effect, it facilitates hydrogen production where protons are reduced into hydrogen. Pt or Ni is usually used for catalyzing this reaction [51] while the semiconductor can be a p-$GaInP_2$ connected to p-n GaAs, which was demonstrated by Khaselev[47]. The photoelectrolyser showed a high solar energy to chemical energy conversion efficiency of 16% based on Gibbs free energy and radiation power. Materials such as P, In, Ga, As, Cd, Te are often used for photocathode and Pt is most often used as the catalyst.

The photoanode can be made using transition metal. The most common materials include Ce, Ti, Zr, Nb, Ta, Zn, Fe, Ga, Ge, Sn and Sb[46]. Yasser et al[49] reported a photoelectrolyser using Si doped carbon modified n-Fe_2O_3 as photoanode and Pt as the cathode. The highest solar to chemical energy conversion efficiency of 3.1% was reported. This efficiency is lower than that of indium based electrode that is commonly used for photoanode. InP with Rh as the catalyst was reported to have 12% efficiency [46]. However, the use of Fe in n-Fe_2O_3 photoanode can have a significant reduction in the cost of manufacturing.

Recently a breakthrough in photoelectrolysis was made by Nocera et al[50]. Instead of noble metals that are used in most photoelectrolyzers, they managed to make a water splitting electrolyzer out of relatively cheap materials like Ni, Mo, Zn, Co, Si and Ge. The photoanode was consisted of 3jn-a-Si layers with an ITO (indium tin oxide) coating layer and Co as the catalyst on the coating. A NiMoZn compound was used as the catalyst on the Ni based cathode side. The electrolyzer was able to achieve solar to chemical energy conversion efficiency of 4.7%.

As it can be observed from the above-mentioned research, the efficiency of photoelectrolysis is still low compared to PEM or high temperature electrolysis. The high cost materials that are usually used to make photoelectroyzers add to the disadvantages of its

low efficiency. Thus photoelectrolysis still has a long way to go before it can be a method comparable to other electrolysis methods. Meanwhile, PV powered alkaline water or PEM electrolysis may be a better solution for hydrogen production.

2.3 Methane Reforming Technologies

Despite the popularity of research on electrolysis of water, methane reforming is still the most important source of hydrogen. The use of water splitting as a hydrogen source may sound attractive but is also very energy demanding. Methane as the hydrogen source, on the other hand, uses less energy and can be reformed using catalysts. The most traditional way of methane reforming is steam methane reforming, which yield high concentration of hydrogen. However, CO_2 reforming as gained much attention in research in recent years because of the CO_2 problem the world is facing. The section will introduce the research on CO_2 methane reforming first and then steam methane reforming.

2.3.1 CO_2 reforming of methane

Reforming of CH_4 with CO_2 to produce syngas can produce hydrogen as well as recycle CO_2. This process was developed decades ago and has been a popular research topic on CO_2 recycling. The advantage of the process is that it produces a molar ratio of CO and H_2 close to unity. Such a mixture of CO_2 and H_2 is ideal for Fischer-Tropsch synthesis of long-chain hydrocarbons. The reforming of CH_4 with CO_2 is represented by:

$$CH_4 + CO_2 \leftrightarrow 2H_2 + 2CO \qquad \Delta H°=59.1\text{kcal/mol} \qquad (2\text{-}20)$$

However, in a high temperature (600-900°C) CO_2 rich environment, H_2 will reactor with CO_2 according to reverse water-gas shift (RWGS) process:

$$CO_2 + H_2 \leftrightarrow CO + H_2O \qquad \Delta H°=41.2\text{ kJ/mol} \qquad (2\text{-}21)$$

The RWGS produces additional CO, which leaves the product syngas with a ratio of H_2/CO less than unity. This is actually not a bad combination of the two gases because during

alkane production, not only synthesis of CO and H_2 (2-22) but also the water-gas shift (2-23) reaction takes place:

$$nCO + (2n + 1)H_2 \rightarrow C_nH_{2n+2} + nH_2O \quad (2\text{-}22)$$

$$H_2O + CO \rightarrow CO_2 + H_2 \quad (2\text{-}23)$$

The overall reaction of these two comes to:

$$2nCO + (n + 1)H_2 \rightarrow C_nH_{2n+2} + nCO_2 \quad (2\text{-}24)$$

Consequently the desirable syngas composition of H_2/CO is (n+1)/2n, which is always less or equal to unity, and is the expected in the products of methane CO_2 reforming. Because CH_4 reforming with CO_2 recycles two greenhouse gases simultaneously, the reaction has been studied by many researches.

Most of the researches focus on the synthesis of novel catalysts to promote CO_2 and CH_4 conversion. Metal catalysts such as Ru, Rh, Pt, Ni[57] have been tested. The effect of Ni on reactivity is prominent. However, deactivation of the catalytic activity is also significant due to carbon formation on surface Ni particles. The carbon formed is produced from CO and CH_4 decomposition according to following two reactions:

$$2CO \rightarrow CO_2 + C \qquad \Delta H=-171kJ/mol \quad (2\text{-}26)$$

$$CH_4 \rightarrow 2H_2 + C \qquad \Delta H=75kJ/mol \quad (2\text{-}27)$$

Since the decomposition of CH_4 is an endothermic reaction, it is more likely to happen at higher temperature [58]. Compared to Ni, noble metals Rh and Ru show greater reactivity and more resistance to coke formation [59]. Other two noble metals Pt and Pd are also more resistant to carbon formation and have comparable activity to that of Ni. However, noble metals are less available and more expensive, which makes Ni the most reasonable choice for catalyst. Consequently, preventing coke formation from CH_4 decomposition on Ni has been a main focus of catalyst research in the recent decade.

Rostrupnielsen et al[59] investigated the performance of different catalyst in a fixed bed reactor. The different catalysts are Ru, Rh, Ni, Ir, Pt and Pd. About 10-50mg of each metal is impregnated into MgO support. The impregnated MgO is fragmented and packed into the reactor. During the test, the inlet gas passes through the porous catalyst cluster to the outlet. The reactor was heated up to 500°C, 650°C and 700°C. In the CO_2 reforming test, a $CO_2/CH_4/H_2$ ratio of 4/1/0.4 was fed to the reactor at a rate of 360ml/min. The conversion

rate of CH_4 and CO_2 indicated a catalytic reactivity of Ru≈Rh>Ni>Ir≈Pt≈Pd. Tests on the same catalysts on steam reforming and reverse water gas shift reaction also showed the same trend of reactivity. After the CO_2 reforming test, highest carbon formation was found on Ni, with 4.4mg of total carbon formed, while 3.5mg, 0.6mg and 0.4mg carbon was found on Pd, Ir and Pt catalyst respectively. No carbon formation was found on Ru and Rh.

Though using noble metal has a stabilizing effect on the reaction, Ni is the most popular catalyst because of its low cost. Several methods have been tried in an attempt to improve the stability of Ni while maintaining or improving the catalytic activity. Researchers have tried to improve carbon resistance while maintaining reactivity by experimenting with different: 1, Support materials; 2, Catalytic metal alloys; 3, Catalyst synthesis methods; 4, Novel reactor configurations.

Support material

The first thing to look at is the selection of metal oxide support materials. The most common support material that has been used is Al_2O_3 due to its high mechanical strength, high surface area and low price. MgO, TiO, SiO_2, ZrO_2 and La_2O_3 have all been seen in the literature. Zhang et al[60] reported that the reactivity of different support oxides have the order: ZrO_2>TiO_2>Al_2O_3>La_2O_3≈SiO_2>MgO. Ruckenstein et al [61] reported that the reactivity of metal oxide support was in the order of Al_2O_3 >SiO_2>TiO_2 under 790°C with Ni catalyzed CO_2 reforming of CH_4. An experiment done by Yokota et al[62] using Rh catalyst suggested the reactivity order to be: TiO_2>La_2O_3=CeO_2>ZrO_2=MgO=SiO_2=MCM-41>γ-Al_2O_3. Disagreements in experiment results have not been rationalized. The possible causes for this may be different operating conditions, preparation methods, degree of deactivation and even experimental errors [63].

The support material affects the reactivity as well as the stability of the catalyst. In a report by Horiuchi et al [64], basic metal oxides, Na_2O, MgO, K_2O, CaO are each added to Ni/Al_2O_3 catalyst and tested at 800°C under CO_2 reforming. According to the results, Horiuchi suggested that the addition of basic metal oxides suppressed the dehydrogenation of CH_4 and increased the reaction of CO_2 with carbon deposits thus improving carbon stability. It is possible that the basic metal oxide increased the carbon stability due to structural change of the Ni particles. Masai et al [65] found that metal dispersion has strong dependency on the

support's Lewis acidity. Other tests have shown that Pt, and Ni supported on ZrO_2 and TiO_2 demonstrated great stability [63]. The phenomenon, explained by Bradford et al, is due to elimination of large metal atom ensembles under the influence of TiO_2. And it is well established that the carbon formation on metal catalysts are structurally sensitive. Figure 2-8 is used by Zhu et al [58] in their recent paper to explain the effect of particle size on carbon formation. During methane decomposition, carbon layers form on the Ni particles at the catalyst surface. The carbon deposits will react with CO_2 to form CO. The rate of carbon gasification and carbon formation determines the amount of carbon deposition. At surfaces where Ni atoms form bulk ensembles, the carbon will accumulate on the Ni particle or diffuse through the Ni particles until reaching the Ni-support interface. In the first case where carbon forms on Ni, Ni particle is encapsulated. The carbon will block Ni interaction with the reforming gas. In the second case carbon from CH_4 dissociation diffuses through Ni, the particle is lifted from the interface, thus filamentous carbon is formed. In this case, the reforming reaction may still happen where Ni is exposed. On the other hand, if Ni particles are well dispersed over the support with smaller size, the activation energy for carbon formation will be higher, thus much less carbon is formed. The importance of Ni-support interaction is reported by Chen and Ren [66]. In their study, Ni/Al_2O_3 catalysts were calcinated at different temperatures tested. It turned out that the catalyst with higher calcination temperature bare higher carbon resistance, which suggested that a higher $Ni\text{-}Al_2O_3$ interaction increases the carbon resistance.

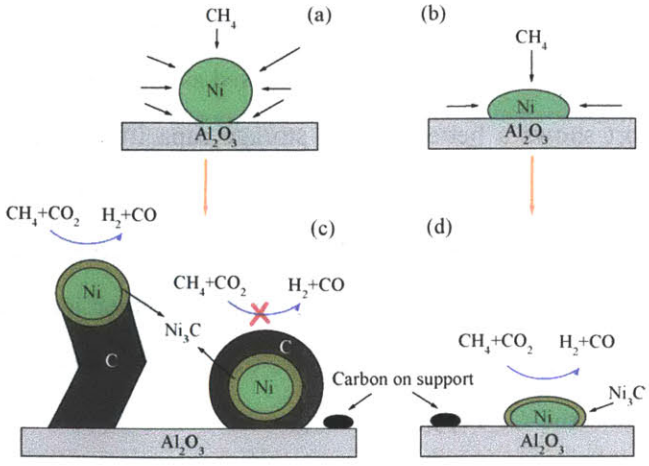

Figure 2-8 Carbon formation mechanism.

As previously mentioned, the performance of the catalysts can be improved by altering the composition of the support. Martínez et al investigated the effect of adding La_2O_3 to Al_2O_3 support by testing the wt% of the lanthanum addition at 0wt%, 4wt%, 8wt% and 12wt% while keeping the Ni catalyst at 33 wt%. The experiment was done in a fixed-bed microreactor (8mm inner diameter, 500mm length) at 700°C with 300sccm of 1:1:4 $CH_4/CO_2/N_2$. The study found that carbon deposition decreased as the lanthanum increased up to 8wt%, above which concentration the carbon deposition increased again. The best CH_4 and CO_2 conversion on the 8%La catalyst was found to be 63.8% and 70.1% respectively. This study demonstrated the stabilizing effect of La against carbon formation as well as the importance of Ni particle size in determining the stability.

In summary, the support material affects both the stability and reactivity of the material. A careful selection of support plays an important part in a good CO_2 reforming catalyst. To improve the carbon resistance, basicity, acidity, crystal structure, and metal-support interaction all need to be taken into consideration.

Catalytic metal alloys

The catalytic metal is critical to reactivity and stability of the catalyst. As mentioned above, the most common transition metals used are in the reactivity order: Ru≈Rh>Ni>Ir≈Pt≈Pd. Ru and Rh are also superior in their stability. However, due the high cost and scarcity of noble metal, most researches focus on Ni. Often Ni is used with other metals to yield better performance. Some of the most common alloys to Ni, besides the above-mentioned metals, are alkali (K, Ca, Ba, Mg) and rare earth metal (La, Ce or Zr) [67].

In a recent report by Koubaissy et al [68], Ni is used as the catalytic metal on a CeO_2-ZrO_2 support. The support shows a better oxygen storage capacity and thus a higher ability for dissociative adsorption of CO_2. The best composition of support material with Ni was found to be $Ce_2Zr_{1.51}Ni_{0.49}$, which showed a CO_2 and CH_4 conversion rate of 81% and 72% respectively at 750°C with 1:1:8 $CO_2/CH_4/Ar$. Then the author introduced 0.5wt% Rh and 2wth% Co into the catalyst. The $Ce_2Zr_{1.51}Ni_{0.49}Co_{0.29}$ demonstrated that CO_2 conversion increased to 83%, and the $Ce_2Zr_{1.51}Ni_{0.49}Rh_{0.03}$ made the CO_2 conversion rate increased to 90%. Furthermore, Rh incorporated catalysts show a supreme stability. The $Ce_2Zr_{1.51}Ni_{0.49}Rh_{0.03}$ catalyst maintained CO_2 conversion rate at 80% up to 200 hours of

operation under 750°C while the conversion without Rh decreased to 30% after 20 hours. This result showed that alloying Ni with superior noble metal like Rh increases the catalytic performance both in terms of conversion ratio and stability.

Pawelec et al[69] used a Pt/Ni catalyst supported on ZSM-5 (aluminosilicate zeolite) and varied the Pt/Ni ratio to study the effect of Pt on Ni activity. ZSM-5 was chosen in this study because of its well-defined structure and large specific surface area. The catalyst was tested in a fixed-bed continuous flow reactor in a quartz tube. 100sccm of reactant gas with $CO_2/CH_4/N_2$ ratio of 2:2:6 was introduced to the reactor. The study showed a decrease in CH_4 and CO_2 conversion with increasing percentage of Pt but a increasing stability. The author finds the optimal balance between stability and conversion at Pt/Ni weight ratio of 1:6. The CH_4 conversion ratio of this catalyst maintained 6% after 380 hours of operation at 500°C (highest is 10.9% at 500°C). The author attributes the stability of Pt/Ni with 1:6 ratio to the homogeneous surface distribution of Ni. Since the catalytic activity primarily takes place at the Ni-Pt boundary, the carbon deposition on Ni crystallites does not significantly affect the reactivity.

In summary, alloying Ni with other catalytic metal can improve the performance of Ni. The addition of Ru or Rh increases both stability and performance while certain arrangements with Pt and Pd improve the performance depending on the crystal structure. Other metals such as Co, Fe, Mg etc. also have the potential to improve the catalyst. The selection of metal alloys must consider the catalytic reactivity, the stability and the cost of material.

Synthesis method

Since the catalytic particle size has a significant influence on the carbon formation, many recent researches looked into ways to improve the crystal by altering surface structure. The surface features that aid CO_2 reforming with CH_4 include high specific surface area, fine crystalline structures and homogeneous distribution of the metal particles.

Shen and coworkers [70] used ordered mesoporous Al_2O_3 supported Ni catalyst in their recent study. Four different catalysts were prepared: mesoporous Al_2O_3 with 7wt% Ni (Ni/MA), mesoporous Al_2O_3/20mol%Mg with 7wt%Ni (Ni/Mg/MA), Ni/Al_2O_3 without mesopores (Ni/Al) and Ni/$MgOAl_2O_3$ without mesopores (Ni/Mg/Al). 10mg of each catalyst was tested in a fixed-bed reactor with 25sccm CH_4, 25sccm CO_2 and 35sccm N_2. The

mesoporous structured Ni/MA and Ni/MgMA showed initial CH_4 conversion ratio around 90%. The methane conversion ratios of Ni/Al and Ni/MgAl without mesopores were only 32% and 9% respectively. The mesoporous structure was also more stable. After 26 hours of operation, the CH_4 conversion on Ni/MA and Ni/MgMA was 78% and 64% respectively. During the stability test only trace amount of coke was found on Ni/MA and no coke was found on Ni/MgMA. The high initial conversion rate of Ni/MA and Ni/MgMA was due to the higher specific area. According to the study, the mesopores prevents Ni nano-particles from sintering thus the Ni particles remained small (5-10nm), while the Ni particle size on catalysts without mesopores increased from 3nm to 30nm after dry reforming. Thus the study shows that inhibition of Ni sintering by novel synthesis method can be a solution to coke formation.

Another mesoporous support, ZSM-5, was tested by Sarkar et al [71]. 200mg of the catalyst with 5wt% Ni was tested in a fixed-bed down flow reactor at atmospheric pressure. High CH_4 conversion of 96.2% was achieved due to the large surface area. After 9h of operation, the conversion of CH_4 went down to 72.9% due to formations of coke and $NiCO_3$. Other mesoporous materials, Pt/ZrO_2 [72], $Ni/CaO\text{-}Al_2O_3$ [73], $Ni/CaOZrO_2$ [74] have been tested. The results suggested that mesoporous structure enhanced metal dispersion as well as improved the surface area. Besides, the "confinement effect" of the mesopores limits the growth of metal particles, leading to better resistance to metal sintering and ultimately to better stability [75].

Besides mesoporous structure, the other treatment that has been used by researchers is plasma treatment. The H_2 or Ar plasma is used to reduce the catalyst metal and support. The traditional way to reduce the catalyst is by flowing H_2 through the sample at an elevated temperature (~600°C). The advantage of plasma treatment is better dispersed active metal species. Zhu and coworkers [58] tested a $5wt\%Ni/Al_2O_3$ catalyst reduced by argon glow discharge plasma. The catalyst powder was prepared by impregnation of Ni to Al_2O_3, and loaded into a discharge cell at 100-200Pa. The argon discharge was initialed by a 900V voltage amplifier operating at 100Hz frequency. In comparison, a Ni/Al_2O_3 catalyst without plasma treatment was also tested. The tests revealed that at the same experimental conditions, both conversion ratios and stability are higher in the case of plasma treated sample compared

to normal samples. The reason for enhanced performance, according to the authors, is smaller Ni size and stronger Ni-support interaction. TEM image showed that the plasma treated Ni/Al_2O_3 had an average particle size of 7.4nm while the other one had a size of 12nm.

Similar argon discharge plasma treatment was done by Wang et al [76]. They used Rh/Al_2O_3 as the catalyst and compared thermally hydrogen-reduced catalyst with argon plasma reduced catalyst. Their test showed similar performance of the two catalysts. The particle size of plasma-reduced catalyst in this case was slightly higher (1.2nm) compared to that of thermally reduced (0.8nm). The authors rationalize that the uniform distribution of particles was due to static electric repulsion between the metal particles. And the higher particle size of plasma treated catalyst did not help improve the performance.

Similar plasma synthesis methods were also applied on Pd/Al_2O_3, Ni/SiO_2, Pd/HZSM-5, Pt/NaZSM [77], and they all show enhanced low temperature activity and higher coke resistance due to better crystalline structure.

To conclude on the synthesis method, the trend of improvements is to prepare catalysts that have small active metal particle size, high surface area and strong metal-support interaction.

Novel reactors

Other than improving the catalyst performance in a fixed-bed reactor, researchers have also tried novel idea on the reactor design to make the conversion more complete and faster.

In a recent study, Labrecque and Lavoie [78] used an electrothermal process for dry reforming of carbon dioxide. The reactor was still a fixed-bed continuous flow reactor, but the catalyst used was steel wool. During reaction, electrical current ran in the steel wool to promote the reforming reaction. During the test, a flow of 375sccm CO_2 and 250sccm CH_4 was fed to the reactor at 750°C. Electrical current of 2.2V and 100-150A was applied to the steel wool during the reaction. They observed that the electrical current significantly increased the CH_4 conversion by the fact that CH_4 content in the outlet gas decreased from 36% to 11.5 % when current was applied, which corresponded to CH_4 conversion increase from 50% to 75%. It was also shown that addition of 50% water vapor enhanced CO_2 conversion from 50% to 88.3% and CH_4 conversion from 75% to 94%. The results indicate that electrical current enhance the catalytic reactions on the catalyst. It also showed that by adding water

into the reaction, the CH_4 and CO_2 conversion both increased. Although the authors did not explain the reason behind water enhance, it was likely an effect of RWGS and steam reforming of CH_4.

Another interesting concept was developed by Gallucci et al[79]. In their work, Ni/Al_2O_3 catalyst is combined with membrane reactor to yield higher conversion. Three reactors were tested in the project. The first reactor was a traditional tubular fixed-bed reactor (TR), the second one was a porous membrane reactor (porous MR) made of Pd-Ag membrane, and the third one was a dense Pd-Ag membrane (dense MR). In the membrane reactors, Ni based catalysts were packed in the membrane tubes and N_2 gas ran on the outside of the tubes. When fed with 1:1 CH_4 and CO_2 gas at 450°C atmospheric pressure, the CO_2 conversion for TR, porous MR and dense MR were 14.02%, 20.6% and 13.2% respectively. The conversion of CH_4 was 17.4%, 8.4% and 17.9% for TR, porous MR and dense MR respectively. The higher CO_2 conversion in porous MR is rationalized as the CO permeating through the membrane whereas the CO_2 stays, thus increasing the flow rate. The higher CH_4 conversion in dense MR was rationalized as the H_2 permeating through the Pd-Ag membrane, thus increasing the CH_4 conversion. Another interesting observation from the tests was that carbon deposition on the dense membrane was lower than those on porous MR and TR. The reason was not clearly understood, but one hypothesis was the equilibrium shift of the following reaction:

$$CO_2 + H_2 \leftrightarrow H_2O + C \qquad \Delta H=-84kJ/mol \qquad (2\text{-}28)$$

With hydrogen permeating through the dense membrane, carbon deposition reacts with the water vapor produced from reverse water-gas shift reaction.

The low conversion enhancement from the membrane reactors of Gallucci et al was probably due to low permeation rate of the membrane. In fact, similar experiment was done by Galuszka et al [80] with Pd/Al_2O_3 and Pd dense membrane. In the result, both CO_2 and CH_4 conversion was increased by about 8% at 600°C. However, the Pd membrane was deactivated after long term test due to carbon deposition. Nevertheless, the idea of using gas selective membrane to enhance the conversion and reaction rate is a promising concept. Combining membrane with catalysts, one can control the composition of gas products from methane dry reforming, or even reduce the amount of carbon deposition as demonstrated in the study.

To summarize the current research area in dry reforming, efforts are made in the following focuses:

1. The synthesis of novel catalyst promoters by alloying noble metal or alkaline earth metal.
2. Improvement on support material by alloying Al_2O_3 with transient metals, by using defined structures like perovskite and spinel, or by using nano-structure.
3. Investigations into novel preparation methods such as combustion, microwave radiation and plasma treatment.
4. Innovations in reactor design such as using selective membrane and electrothermal processes.

Table 2-4 contains some of the research done on CO_2 methane reforming. The comparison among methane reforming research is not straightforward because the conversion rate of methane and CO_2 varies depending on the amount of catalyst and gas flow rate. The purpose of Table 2-4 is to provide the reader a survey of different methods researchers have used to improve the reaction rate and stability of CO_2 methane reforming.

Table 2-4 CO_2 methane reforming experiments

Catalyst	T°C	Method	X_{CH4}	X_{CO2}	Ref.
Iron Wool	776	Electric current assisted, CH_4 and CO_2 only	75%	50%	[78]
Iron Wool	760	Electric current assisted, with saturated water vapor	94%	88%	[78]
$NiMgAl_2O_4$ +8.8wt% Ni	800	Addition of 0.5wt% gold increase stability suppresses graphite formation	42%	100%	[100]
Ni/ZSM-5	800	Ni-nanoparticle supported on mesoporous ZSM-5	92%	96%	[71]
$Ni/MgAl_2O_4$	700	Fixed bed reactor Ni with Mg added minimize carbonation	96%	92%	[67]
Pt/20%CeZrO2 +Al_2O_4	450	Combined Pd-Ag membrane reactor with 90sccm Ar sweep gas	19%	25%	[101]
Ni/Al_2O_3	800	Argon glow discharge treatment	89%	92%	[58]
$Ni/La_2O_3/Al_2O_3$	700	8%Ni shows optimum performance	65%	70%	[57]
$Ce_2Zr_{1.51}Ni_{0.49}$	750	Ce -Zr oxide as support	72%	81%	[68]
Ni+Al_2O_3	750	Mesoporous Al with Ni	84%	86%	[102]
Ni+$MgOAl_2O_3$	750	Mesoporous Al+Mg with Ni	93%	86%	[102]

2.3.2 Steam methane reforming

Steam methane reforming (SMR) is the industrial process for making syngas and producing hydrogen. Tessie du Motay and Marechal first described the process of steam reforming with hydrocarbons using CaO in 1868 [81]. Later in 1889, Mond first used Ni as the catalyst. The first industrial steam reformer was installed in 1930 at Baton Rouge [81]. Eighty years has passed since the first industrial installation of the steam methane reformer, but the basic principle and catalyst behind the process has not changed. Ni/Al_2O_3 is used in MSR due to nickel's high reactivity and low cost as well as Al_2O_3's high surface area, stability and mechanical strength. The advantage of SMR over other hydrogen production methods is the high hydrogen yield, low cost and high reaction rate. Thus despite the development in hydrogen technology, SMR still remains as the dominant method for H_2 production in the near future.

The main reactions of MSR are:

$CH_4 + H_2O \leftrightarrow CO + 3H_2$ $\Delta H°=206kJ/mol$ (2-29)

$CO + H_2O \leftrightarrow CO_2 + H_2$ $\Delta H°=-41.2kJ/mol$ (2-30)

Total Reaction: $CH_4 + 2H_2O \leftrightarrow CO_2 + 4H_2$ $\Delta H°=164kJ/mol$ (2-31)

The first step of partially oxidation of methane is carried out at temperature 800-1000°C and pressure of 14-20atm [82]. Some CO will continue to react with steam, forming H_2 and CO_2 via water gas shift (WGS). The resultant gas from the SMR will be mostly H_2, with about 10% of CH_4, CO, CO_2 and H_2O each [82]. If the desired final product is hydrogen, the effluent gas will be fed into a WGS reactor with lower temperature (300°C-400°C) to further produce H_2 using the remaining CO and H_2O. At the downstream, pressure swing adsorption (PSA) technology or amine scrubbing is used to remove CO_2.

The catalyst used in SMR can also be used in CO_2 methane reforming, vice versa all the catalysts in CO_2 methane reforming mentioned above can be used for SMR. SMR also share the problem of carbon formation, which is the problem most researchers are trying to solve. The two reactions responsible for carbon formation are CO_2 dissociation (2-26) and methane dissociation (2-27). The primary carbon formation mechanism is methane dissociation

because it is more favorable at the reforming temperature. Unlike CO_2 methane reforming, in SMR the large amount of steam reacts with carbon and alleviates the problem. The steam to methane ratio in industrial plant is around 2.5-3 to prevent carbon deposits. However, it is not energy efficient to feed excessive amount of water into the reaction. Thus, the improvement of SMR coke resistance in steam reforming is still attracting much research attention. The methods to prevent coke formation that were mentioned in the dry reforming section also can be applied in steam reforming. Firstly, the addition of noble metals such Pt, Pd, Ag and Rh all contribute to the reactivity and coke resistance of the catalyst. Second, the addition of rare earth metals such as Ce, La and Ce-ZrO2 result in enhanced metal-support interaction and Ni dispersion. Third, the use of novel supports such as spinel structured and perovskite often has very good results. For example, Choi and Moon [83] used Ce-substituted $LaFe_{0.7}Ni_{0.3}O_3$ for steam reforming and found that the Ce improved CH_4 conversion, hydrogen selectivity as well as coke resistance. The spinel structured aluminum oxide Al_2O_4 was used in a report by Enger et al [84] for steam reforming. Lastly, the preparation methods that generate finer catalyst particles can lead to desirable coke resistant properties. One example is plasma treatment, which include plasma jet, glow discharge, thermal plasma chemical vapor deposition and dielectric-barrier discharge [85]. The treatment enhances particle distribution and leads to smaller nickel particle size.

The advantage of methane steam reforming over other hydrogen production methods is its low cost and high yield. The use of Ni catalyst over Al_2O_3 support is so cheap and efficient that even if other catalysts have better performance, it is hard to compete with Ni/Al_2O_3 in terms of hydrogen price.

While the improvement of catalyst performance is critical, many researches seek to improve the hundred-year-old steam reforming technology by combining other processes and reactions into the system. One particular chemical process that direct comparison to this thesis is combined reforming of $CH_4/CO_2/H_2O$, which is also the gases that will be used in the proposed membrane reactor. Thus the next section will be devoted to combined steam-CO_2 reforming.

2.3.3 Combined Steam Dry Reforming of Methane

The benefit of combing steam reforming and dry reforming of methane is two-fold. First, by adding CO_2 into steam reforming, CO_2 can be reused. Second, by combing the reactions, the product gas can have a H_2/CO ratio of about 2, which is desirable for Fischer-Tropsch and methanol synthesis [86].

Al-Nakuoa et al [86] tested the combined reaction in a narrow channel reactor. 49wt% Ni/51wt%Al_2O_3 and Ni(33%)-Cr(5.6%)-Ba(11%)/La_2O_3(19%)-Al_2O_3(31%) were tested. The catalyst was coated on the walls of micro-channels with width and heights of a few millimeters. Reaction was tested under temperature ranging from 600°C to 900°C, pressure from 1bar to 20bar and varying mixture ratios. They observed that if the Ni-Cr-Ba/ La_2O_3-Al_2O_3 were used as the catalyst, the addition of steam to dry reforming decreased CO_2 conversion but the coke resistance increased by five times during the 140hr test. By adjusting the $CO_2/H_2O/CH_4$ ratio, the desirable H_2/CO of 2.2 could be achieved at 700°C and 3bar. The steam/carbon ratio was maintained above 0.51 to prevent carbon deposition.

Soria et al [87] conducted both thermodynamics analysis and experiment test on combined steam dry reforming. The catalyst used in the experiment was Ru supported on ZrO_2-La_2O_3. The thermodynamics analysis and experiment were carried out on 10%CH_4/10%CO_2 balanced with He and H_2O varied from 1% to 5%. Both the numerical analysis and experimental results showed that before reaching 550°C, CH_4 conversion increased with increasing amount of water vapor, while the CO_2 conversion decreased. The RWGS reaction is favored to greatest extent at 550°C. At temperature above 550°C steam reforming is thermodynamically more favored than DRM and water was increasingly being consumed with increasing temperature. CO_2 conversion also increased with rising temperature regardless of water content, suggesting that DRM is increasingly more important compared to WGS. The study showed that the reaction is a complex combination of DRM, SRM, WGS and RWGS, and depending on temperature and feed composition, the products can be adjusted as desired.

In the recent report by Oyama et al. [88], they compared hydrogen production by SR and

DR. They criticized the DR process for being inefficient in producing hydrogen. The RWGS inevitably consumes hydrogen during the reaction. A packed bed reactor was used for testing dry reforming using 0.5%Rh/Al_2O_3 and steam reforming using 15%$Ni/MgAl_2O_4$. They also tested the reforming reaction with hydrogen selective membrane. The finding was that with increasing pressure in dry reforming, hydrogen yield increased in both packed bed reactor (PBR) and membrane reactor (MR). The hydrogen yield was below what was predicted by equilibrium during dry reforming in PBR and above equilibrium in MR. However, in both cases, the hydrogen yield leveled off at about 20atm. On the other hand, the steam reforming hydrogen yield kept increasing in both PBR and MR. According to the results they concluded that dry reforming was not appropriate for hydrogen production.

Maestri et al [103] analyzed the reaction mechanisms of both steam reforming and dry reforming according to numerical models and experimental data. Their model found that the most important steps are methane activation reactions, which is the pyrolysis and carbon oxidation of methane by OH*. The only exception is that when CO_2/CH_4 is smaller than unity, in which case the RWGS becomes rate limiting. The other steps involving CO_2 and H_2O including the WGS are at quasi-equilibrium state when CO_2/CH_4 is larger than one. And the steam reforming and dry reforming proceed at the same rate. This means that the products can be adjusted by changing the composition of the reactants, which is also suggested by the experiments.

Table 2-5 shows some results of the combined methane reforming from two researches, Al-Nakuoa et al[86] and Lee et al[103]. The data shows that much difference in conversion rates can be made by different catalysts, but huge difference can be made by using different reactants.

While it is true that dry reforming is in disadvantage in producing hydrogen, the product of dry reforming is useful in many applications such as methanation. In situations where the CH_4 contains significant amount of CO_2, dry reforming or combined steam and dry reforming could be used. The desired products can be made by adjusting the compositions, the reaction temperature and the reaction pressure. Further more, by adjusting the water content, coke formation can be further inhibited. The combined reaction is also an analogous process to the proposed LCF membrane reactor where the feed gases consist of CH_4, H_2O and CO_2,

although in our case, CH_4 is separated from H_2O/CO_2. However, the advantage of membrane reactor is the potential to reach complete reaction because methane is separated, while in the case of methane reforming, the conversion rate is limited by equilibrium.

Table 2-5 CO_2 steam reforming of methane experiments

Catalyst	T	CH_4:H_2O:CO_2	X_{CH4}	X_{CO}	H_2/CO	Ref.
$Ni+Al_2O_3$	850	1:2:1	99.37%	57.13%	2.19	[103]
Ni+MgO	850	1:2:1	99.40%	63.05%	1.86	[103]
Ru+TiO	850	1:2:1	98.78%	60.17%	1.88	[103]
$Ni/Cr/Ba+La_2O_3/Al_2O_3$	700	1:5:1.2	93%	7%	2.6	[86]
$Ni/Cr/Ba+La_2O_3/Al_2O_3$	700	2:4:1	90%	13%	2.5	[86]

2.4 Comparison of Hydrogen Production Technologies

2.4.1 Calculation of Membrane Reactor Efficiency

In order to evaluate the feasibility of using high temperature membrane reactor for hydrogen production, the efficiency of the reactor should be compared to existing technologies. The technologies reviewed in this report include: Mixed Ionic-Electronic Conducting Membrane (MIEC), alkaline water electrolysis, solid oxide electrolysis (SOE), proton exchange membrane electrolysis (PEME), photoelectrolysis, dry reforming of methane (DRM), steam reforming of methane (SRM) and steam-dry reforming of methane (SDRM). In this section, we will compare these technologies in terms of energy efficiency.

First let's define the energy efficiency of the membrane reactor. To calculate the energy input and the energy output of the system, several things need to be considered. First, the compressors for the feed and sweep gas streams need to be included. Then to increase the effectiveness of the reactor, heat exchangers also need to be included. Figure 2-9 shows the

membrane reactor system. It can be a sub-system that is integrated into a larger energy production cycle, such as an IGCC power plant.

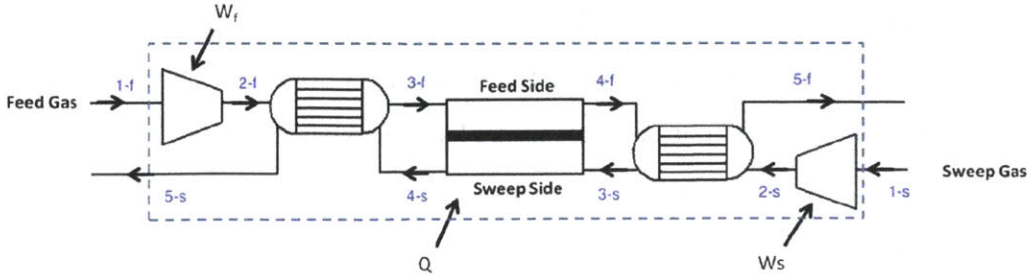

Figure 2-9, membrane reactor system

In Figure 2-9, the membrane reactor system has two compressors and two heat exchangers. The feed gas is consisted of CO_2, H_2O, and N_2. The sweep gas is consisted of CH_4 and CO_2. The feed gas enters at gas state 1-f, then is pressurized by the compressor into a higher-pressure state 2-f. After the compressor, the feed gas is fed into the heat exchanger to be heated by the outlet of the sweep gas and enters gas state 3-f before moving into the membrane reactor. The outlet of feed gas 4-f will go through another heat exchanger to cool down by exchanging heat with the sweep gas inlet and enters gas state 5-f to exit the membrane reactor system. The sweep gas goes through a similar process through gas states 1-s, 2-s, 3-s, 4-s, and 5-s. W_f and W_s are the work done by the compressors and Q is the heat input from the furnace to the reactor. Assume no other heat exchange exits between the environment and the system inside the dashed box.

To analyze the efficiency of the process, let's first defined the efficiency as:

$$\eta = \frac{LHV_{H2}\dot{m}_{H2}+LHV_{CO}\dot{m}_{CO}}{(\dot{m}_{5\_s}h_{5s}+\dot{m}_{5f}h_{5f})-(\dot{m}_{2s}h_{2s}+\dot{m}_{2f}h_{2f})+\frac{W_f+W_s}{\eta_e}} \tag{2-32}$$

$$h_i = h_{i\_f} + \int_{T_o}^{T} c_p dT \tag{2-32a}$$

This definition of efficiency calculates how much energy is produced in terms of the heating values of the syngas products over how much energy is "spent" to produce the syngas. LHV is used in the numerator because steam is used in the reactor rather than liquid water. In the denominator, the first two terms correspond to the heat input to the system, which includes the heat from oxidation of CH_4 and heat from heating of the reactor Q. The first two terms in the denominator calculates the heat input to the system during step 2 through step 5.

The third term in the denominator calculates the energy input to the system from step 1 to step 2, which is the work done by the compressors. The compressor work is converted from electricity to heat by a factor of $\eta_e = 50\%$. This definition of hydrogen production energy efficiency is consistent with the efficiency definition used in PEME and SOE as shown in Eq. (2-17). Some of the values used in calculations are listed below in Table 2-6.

Table 2-6, Table of variables

Variables	Description	Value
$T_{1\text{-}f}$	Feed gas entry temperature	300~500°C
$T_{1\text{-}s}$	Sweep gas entry temperature	25°C
$T_{4\text{-}f}$	Feed reactor exit temperature	800~1000°C
$T_{4\text{-}s}$	Sweep reactor exit temperature	800~1000°C
$P_{2\text{-}f}$	Feed gas compressor pressure	2~6atm
$P_{2\text{-}s}$	Sweep gas compressor pressure	2~6atm
β_p	Pressure drop coefficient	20%
η_h	Heat exchanger efficiency	80%
η_i	Compressor isentropic Efficiency	75%
η_e	Heat to electricity efficiency	50%
X_{CO2}	CO_2 conversion rate to CO and O_2	0.9
X_{H2O}	H_2O conversion rate to H_2 and O_2	0.9
X_{CH4}	CH_4 consumption rate	0.9
S_{H2}	Selectivity of H_2	1

In Table 2-6, the feed gas enters the system at a relative high temperature because it is assumed that the gas is the flue gas of a combustion process. The feed gas is consisted mainly of CO_2, H_2O and N_2. The feed and sweep gases exit the reactor at the same temperature as the reactor temperature. The pressure drop coefficient is the pressure drop across the heat exchangers and the membrane reactor in terms of percentage pressure loss.

The heat exchanger efficiency is defined as:

$$\eta_h = \frac{mc_p(T_{out}-T_{in})}{(mc_p)_{min}(T_{hot}-T_{cold})} \quad (2\text{-}33)$$

Where the T_{out} and T_{in} are outlet and inlet temperatures; T_{cold} and T_{hot} are cold gas inlet and hot gas inlet temperatures; $(mc_p)_{min}$ is the smaller of the products of mass and specific heat between the two gas streams.

The compressor isentropic efficiency is defined as:

$$\eta_i = \frac{h_{o\_s}-h_i}{h_o-h_i} \quad (2\text{-}34)$$

Where h_{o_s} is the outlet enthalpy under ideal isentropic condition, and h_o and h_i are the outlet and inlet gas enthalpy.

To calculate the efficiency of the membrane reactor system, the gas compositions of the feed gas inlet, outlet and the sweep gas inlet, outlet must be known. The inlet gas is composed of $n_{CO2}:n_{H2O}:n_{N2}$ in 1:2:6 in order to mimic the exhaust gas composition of a stoichiometric combustion of natural gas in air. The composition of the sweep gas is $n_{CH4}:n_{CO2}$ in 2:7 ratio. Both the sweep gas and the feed gas flow rates are the same so that the CH_4 is converted to CO and H_2 when the CO_2 and H_2O in the fee gas are fully dissociated. To determine the gas composition of the outlet, the water conversion ratio X_{H2O}, the CO_2 conversion ratio X_{CO2}, methane conversion ratio X_{CH4}, and hydrogen selectivity in the sweep gas S_{H2} must be known. The S_{H2} is defined as:

$$S_{H2} = \frac{n_{sweep\_out\_H2}}{2(n_{sweep\_CH4\_in}-n_{sweep\_CH4\_out})} \quad (2\text{-}35)$$

In the calculations of efficiency here, S_{H2} is assumed to be unity. That is, the only oxidation products of CH_4 are CO and H_2. It is also assumed that the conversion ratio of CH_4, H_2O, and CO_2 are all 90%. That means, 90% of H_2O is converted to H_2 and O_2 and 90% of CO_2 is converted into CO and O_2. As can be seen in Figure 2-10, the equilibriums of CO_2 dissociation and H_2O dissociation are almost identical in the region of 750°C to 1000°C, which is the temperature range of the membrane reactor. So the assumption that CO_2 conversion ratio is the same as that of H_2O is reasonable.

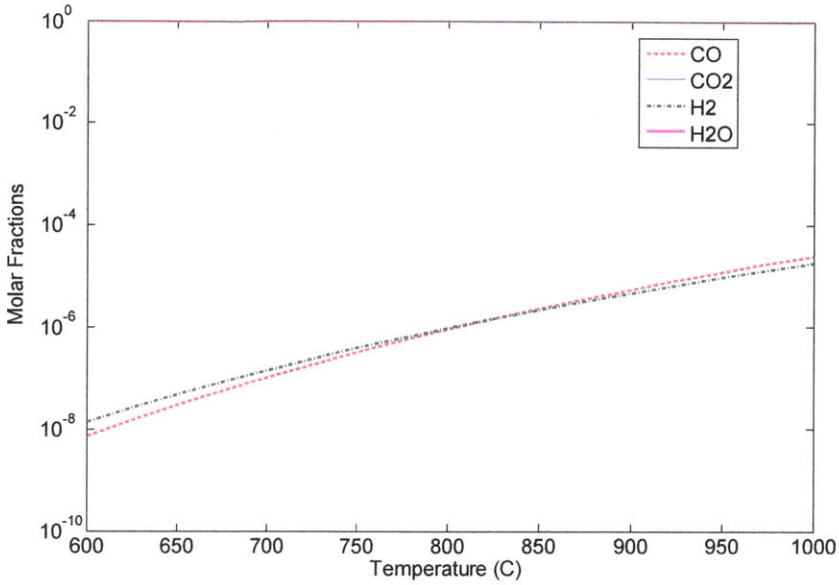

Figure 2-10, the equilibrium of H_2O and CO_2 dissociation at different temperatures, 1atm.

Figure 2-11 shows the results of the calculation on the membrane reactor system efficiency as a function of reactor temperature at different pressures. The conversion of H_2O to H_2 and the conversion of CO_2 to CO are both assumed to be 90% and the feed inlet temperature is 300°C. The pressure P2 in the figure refers to $P_{2\text{-}f}$ and $P_{2\text{-}s}$, which are the pressures that the compressors compress the gases to. Although the heat exchanger reduces the heat required for heating up the gases, the efficiency of the heat exchangers is not 100%. So the efficiency of the system decreases with increasing reactor temperature because more energy is needed for heating the gases to higher reactor temperature at given H_2O and CO_2 conversion ratio. Also, higher pressure requires more compressor work so that the efficiency decreases with increasing pressure.

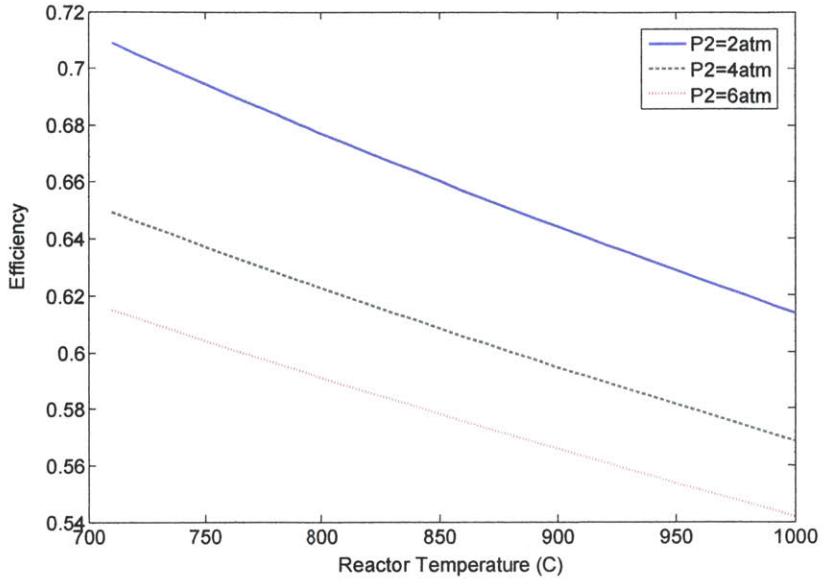

Figure 2-11, Reactor temperature v.s. efficiency. Feed inlet temperature 300°C. Conversion ratios 90%.

Similarly, in Figure 2-12, the efficiency increases as the inlet temperature of the gases increase. The inlet temperature refers to the temperature of the feed gas before it enters the system. The conversion ratios of H_2O and CO_2 are assumed to be 90% and membrane reactor temperature 900°C. With higher inlet temperature, less energy is required to heat the gases to the operating temperature of the reactor. Although the increase in inlet temperature requires more compressor power for the same reactor pressure, the increase in compressor work is offset by decrease in heat requirements. Thus it is beneficial to have an inlet feed gas of higher temperature. However, the inlet temperature should be limited by the power of the compressor and the temperature limit of the piping material. And under the same conversion rate, it is the best to choose the minimal pressure needed to improve the efficiency.

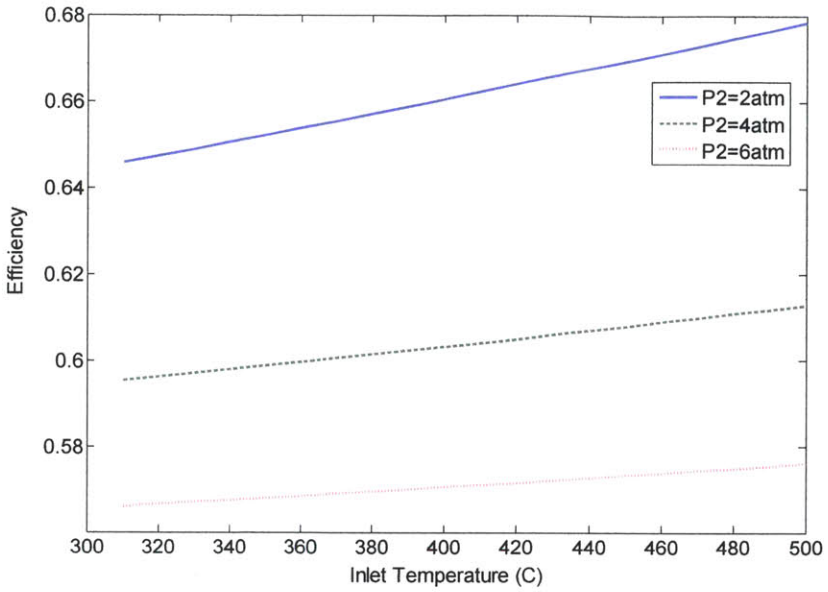

Figure 2-12, Inlet temperature v.s. efficiency. Reactor temperature 900°C. Conversion ratios 90%.

Figure 2-13 shows the efficiency of the system as a function of water conversion ratio. The CO_2 conversion is assumed to be always the same as the water conversion ratio. The feed gas inlet temperature is 300°C and the membrane reactor temperature is 900°C. The efficiency increases as the conversion ratio increases, and the increase is significant in the beginning but slows down at high conversion ratio. This implies that at high conversion ratios such as 90%, it may be less economic to try further increasing the conversion compared to improving other parameters, such as decreasing the membrane operating temperature and improving insulations.

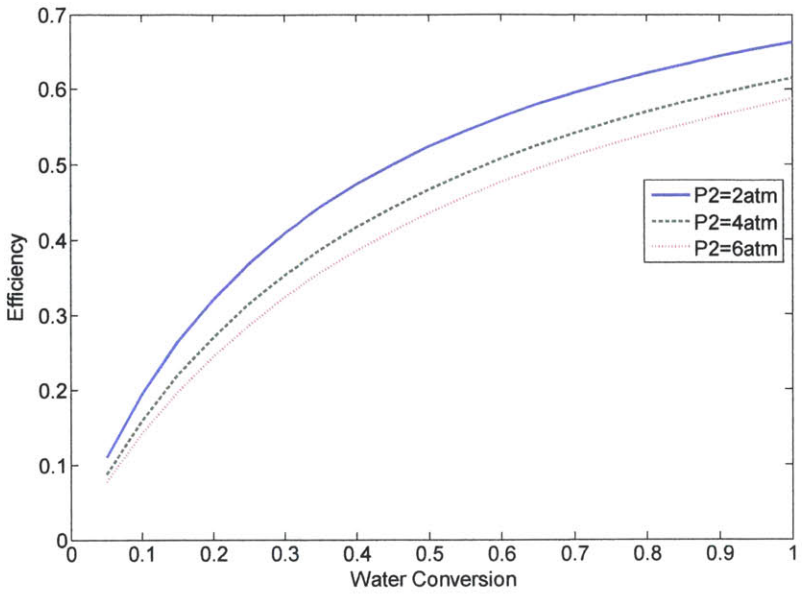

Figure 2-13. Efficiency v.s. water conversion. Membrane reactor temperature 900°C, feed inlet temperature 300°C.

Figure 2-14 plots the energy use in terms of percentage of total energy. The item "HF" refers to energy used by partially oxidizing CH_4 calculated from the change in heat of formation. The "Q" corresponds to the heat from the furnace used for heating up the sweep and feed gas calculated from the change in sensible heat. The "W" refers to the energy used by the compressors, which is converted from electricity to heat by a 50% factor. The feed gas inlet temperature is 300°C and the conversion ratios of H_2O and CO_2 to H_2 and CO are 90%. As can be seen from Figure 2-14, most of the energy used during the process is the energy stored in CH_4, as signified by 'HF'. When the reactor temperature or operating pressure is increased, more energy "Q" is used to heat the gas and more "W" is needed to compress the gas so that the "HF" occupies less percentage of the total energy use. It can be seen from the plots that the compressor work can occupy a large percentage of energy use. It is therefore preferred to operate the reactor at lower temperature and pressure to decrease the energy spent in heating and compressing the gases.

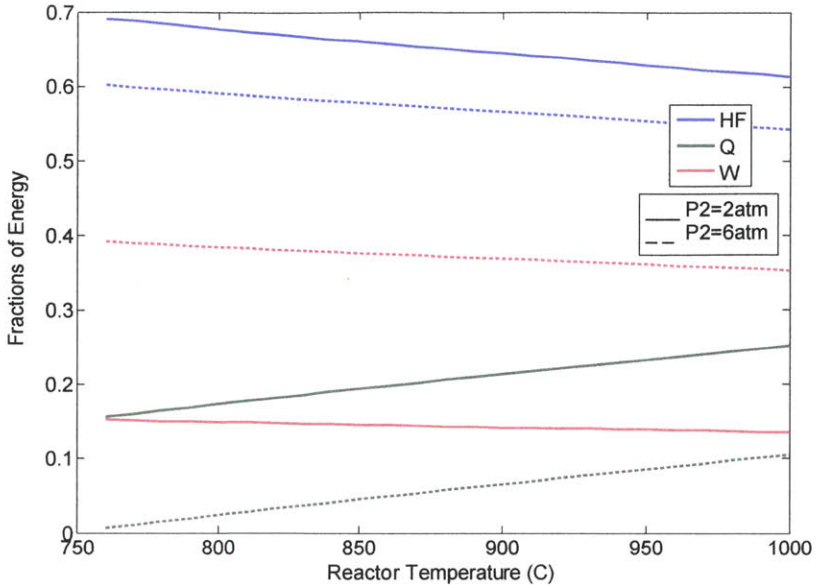

Figure 2-14, Energy fractions v.s. reactor temperature. Water conversion 90%, feed inlet temperature 300°C.

The relatively low efficiency calculated in this analysis is due to the realistic assumptions of pressure loss, heat exchanger efficiency and compressor efficiency. On the other hand, it is not difficult to achieve H_2O and CO_2 conversion ratios larger than 70% because membrane reactors are not limited by equilibrium. Assuming that the compressor pressure is 4atm and the membrane operating temperature is 900°C, the reactor system can achieve an efficiency of 60% according to the calculations. However, there is a trade-off between the membrane efficiency and the cost. The reactor can be designed so that the conversion ratio is larger than 90%, which gives efficiency higher than 60%. To achieve high efficiency, however, larger membrane area is needed, which will increases the cost. Thus to improve the membrane technology and to make it more competitive compared to other hydrogen production methods, membranes with high oxygen permeation rate per unit area is needed. It is also important to improve the efficiency of the compressors and the heat exchangers and reduce the pressure loss of the gases through the reactor.

2.4.2 Comparison with Methane Reforming Methods

The production of hydrogen is conventionally done by steam-methane reforming. The process usually includes a catalytic reformer and a combustor that provides heat by burning CH_4. After the reformer, the syngas is let into one or two shift reactors to perform water gas shift reaction so that CO and reaming H_2O became CO_2 and H_2. At the end of the process, a PSA reactor is used to separate hydrogen from CO_2. It is reported that the efficiency of steam-methane reforming based on lower heating value is 74% to 83% [89]. A study done by X.D. Peng [89] set the efficiency limit of the process to 90%~93% based on thermodynamic simulations. The simulation included the reformer, the combustor, a global heat exchanger and a PSA reactor. However, Peng's study did not consider the efficiency of compressors and efficiency of heat exchangers. Thus the study only gave a theoretical limit of the process. Another study done by M.A. Rosen [90] reported the efficiency of H_2 production by methane steam reforming to be 86%. This report calculated the entire process of hydrogen production including heat exchanging, reforming, water-gas shift and CO_2 removal. The efficiency was 92% if only looking at reforming and heat exchanging. That is, if the final product were syngas like in the case of membrane water splitting reactor analyzed above, the efficiency would be 92%. In this study, the reforming temperature was 370°C and reforming pressure was 34atm. In a study by Lutz et al[91], both computational and experimental results were compared. The study considered a system with a vaporizer, heat exchangers, a reformer and a membrane separator for extracting hydrogen. Since the study compared the computational results with experiments where the reformer was not pressurized, the simulation did not include pressure change. The study investigated the effect of steam to carbon ratio, exhaust temperature and reformer temperature and included chemical equilibrium calculation. The result showed that the efficiency of the system was 75% to 85% depending on different conditions, which is in agreement with industrial reports.

Based on the previous calculations of efficiency in a possible membrane reactor, the efficiency of methane reformer is close to that of a membrane reactor. Although the membrane reactor needs higher reaction temperature, heat exchangers can largely alleviate

the energy cost of high temperature. With higher heat exchanger efficiency and compressor efficiency, the membrane reactor can achieve similar over efficiency as the methane reformers.

The other question is that how much should the membrane reactor's capital cost be to make it comparable to methane-steam reformers. To achieve a reasonable water conversion ratio, proper membrane reactors need to be designed. The cost of it depends both on the material cost of membranes and the hydrogen production per unit area of these membranes. To estimate the operation cost and capital investment, simulations of hydrogen production in a membrane reactor need to be made and the total area of membrane need to be found based on the simulations. A good reference of a similar simulation on oxygen transporting membrane can be found in a paper written by Mancini et al[92][93]. The investigation on the hydrogen production cost analysis compared to steam-methane reforming is beyond the scope of this thesis but will need to be considered in future work.

2.4.3 Comparison with Water-Splitting Methods

Water dissociation methods include mixed ionic-electronic conducting membrane (MIEC), alkaline water electrolysis (AWE), solid oxide electrolysis (SOE), proton exchange membrane electrolysis (PEME) and photo-electrolysis. The hydrogen production reactions in this group of methods all share the same process: ion transportation. Since only ions are transported, the selectivity of the ion, either it is H^+ or O^{2-}, is always 100%. This means that only a thin layer of the material, either it is PEM or OTM, is sufficient to separate the products from the reactants. In fact, in order to facilitate the process, thinner layers are needed to improve the transporting rate. Because of this thin layer configuration, the hydrogen production rates are often reported on per unit area base. In table 2-7, a comparison of the H_2 production rates reported in $\mu mol/s/cm^2$ are listed.

Table 2-7. Comparison between water splitting methods.

Method	Material (catalysts, dopant)		Sweep	Feed	T [°C]	H2 rate [μmol cm^{-2} s^{-1}]	Ref.
MIEC	Gd-CeO2 (CGO)	Ni	H_2 + He	H_2O + N_2	900	4.464	[4,5,6]
		NiO	H_2 + He	H_2O + N_2	900	7.44	
	SrFeCo0.5Ox		H_2 + He	H_2O + N_2	900	3.72	[5]
	GdCeO-GdSrTiAlO		H_2 + Ar	H_2O+Ar+H_2	900	7.5	[7]
SOE	Cathode: La0.75Sr0.25Cr0.5Mn0.5O3-δ-YSZ Electrolyte: YSZ Anode: La0.8Sr0.2MnO3-δ-YSZ		air	H_2O+H_2+N_2	850	6.36	[30]
	Cathode: NiO-YSZ Electrolyte: YSZ Anode: La0.8Sr0.2MnO3		air	H_2O+H_2+Ar	750	1.58	[29]
	Cathode: La0.6Sr0.4Co0.2Fe0.8O3 Electrolyte: YSZ Anode: Ni/CGO		air	H_2O+H_2	820	1.88	[27]
PEME	Cathode: 10%Pt Vulcan Electrolyte: Nafion Anode: IrO2		N/A	N/A	80	5.12	[36]
	Cathode: 20%Pt/Carbon Electrolyte: Nafion 115 Anode: Ir0.6Ru0.4O2		N/A	N/A	90	5.12	[37]
	Cathode: 50%Pt/C Electrolyte: Nafion 212 Anode: 20% RuO2/ATO (SnO2)		N/A	N/A	80	5.12	[39]
Photo-electrolysis	Cathode: NiMoZn Electrolyte: Potassium Borate Anode: Co/ITO coated Silicon PV: 3jn-a-Si		N/A	N/A	Ambient	0.004	[50]
AWE	Electrodes: Ni Electrolyte: KOH Diaphram: Arylene		N/A	N/A	Ambient	5.12	[16]

In this table, the hydrogen production rate of PEME and AWE are reported as the equivalent value to current density of $1 A/cm^2$. Because in the case of electricity driven water dissociation, hydrogen production rate is controlled by the electrical current across the electrodes. The focus of researches in PEME and AWE is to increase the electricity efficiency, which depends on the over potential that comes from water splitting reactions and resistance in connections. The efficiency of PEME and AWE is defined according to Equation (2-17), which takes the power of hydrogen production over power of electricity. However, heat is a much cheaper energy source than electricity and in many cases free. Thus a direct comparison between thermal efficiency of MIEC and electrical efficiency of PEME and AWE is not appropriate, considering the high cost of electricity. In order to make the comparison, the efficiencies of PEME and AWE are multiplied by 50%.

In the case of SOE, efficiency is calculated by combining the electrical efficiency and thermal efficiency. The electrical energy is divided by 50% to make the comparison consistent. The formula used for this calculation is:

$$\eta = \frac{\dot{m}_{H2} LHV_{H2}}{\frac{Qe}{50\%} + (\Sigma \dot{m}_{i,o} h_{i,o} - \Sigma \dot{m}_{i,i} h_{i,i})} \quad (2\text{-}36)$$

Here Qe is the electrical energy consumption. The second term in the denominator corresponds to the change in enthalpy calculated by the difference between enthalpy of outlet species $\Sigma \dot{m}_{i,o} h_{i,o}$ and that of the inlet species $\Sigma \dot{m}_{i,i} h_{i,i}$. The numerator term is the energy stored in the produced H_2 calculated as the lower heating value of hydrogen. Based on this definition, the efficiency of a particular SOE can be calculated based on the data provided in the literature. The efficiency of MIEC is provided based on the calculations in the simulation. Table 2-8 summarizes the efficiencies of water splitting methods.

Table 2-8 Energy efficiency of water splitting methods

Method	Efficiency	Reference
MIEC	40-68%	This
SOE	35%-55%	[24]-[30]
PEME	32%-40%	[36]-[45]
AWE	22%-35%	[108]
Photo-electrolysis	2%-12%	[16]

Although the efficiency of AWE is reported to be much greater than those shown in Table 2-8, they don't look as great when multiplied by 50% to convert electrical efficiency into thermal efficiency. The efficiency of PEME is also low when the electoral efficiency is converted into efficiency based on heat. The efficiency of SOE is higher than that of PEME because it uses electricity as well as high temperature heat to operate. The data used for SOE and PEME is the experimental data reviewed in this thesis. Lastly, while the photo-electrolysis is a promising technology that uses solar energy, the technology still has a long way to go before being comparable to other hydrogen production methods.

The efficiencies of any of the technologies in Table 2-6 have opportunities to increase. However, the table proves that based on thermal efficiency, the MIEC membrane reactor has a larger advantage by using heat directly.

2.5 Reactor Design

In order to build a mixed conducting membrane (MCM) reactor that produces syngas through membrane assisted H_2O/CO_2 splitting and methane reforming, a proper reactor design must be considered. Even though no membrane reactor has been built for the proposed application, reactors for oxy-combustion or catalytic steam methane reforming have been either build or proposed. The designs of these membrane reactors follow the same principle: to maximize the total flux of oxygen/hydrogen from the feed side to the sweep side of the

membrane. Given a certain membrane, the reactor performance is improved by: 1. minimizing the thickness of the membrane. 2. maximizing the total effective surface area of the membrane reactor. 3. maximizing the oxygen partial pressure difference across the membrane.

The first goal of minimizing the membrane thickness is usually achieved by using thin dense membrane on porous support or rigged support. The second goal of maximizing total membrane area is met by using various methods. The most important configurations can be summarized into tubular, monolith, and planar configurations. All three configurations achieve high membrane area by using thin gas flow channels and compact design. The last goal of maximizing the oxygen partial pressure difference is more complicated. Apparently, one can increase the total pressure on the feed side of the membrane, or decrease the pressure on the sweep side of the membrane. On the other hand, the overall effect of partial pressure difference must also be considered. Thus selecting a co-current flow configuration, a counter-current flow configuration or any configurations in-between must also be considered and simulated when designing the reactor. The study by Mancini et al [93] simulated an oxygen air separation reactor with monolith configuration. In the simulation, air was used as the feed gas with inlet temperature at 973K. The sweep gas was either 1173K CO_2/H_2O at 1:1 ratio or 1173K $CO_2/H_2O/CH_4$ at 10:10:1 ratio. Both counter-current configuration and co-current configuration were simulated for the separation only and reactive cases. The results showed that counter-current configuration was superior to the co-current case with lower pressure drop and higher average oxygen flux. The counter-current reactive case was deemed inappropriate for high heat concentration and high potential for cracking. More interestingly, the study found that the co-current reactive configuration was not better than separation only configuration in turns of oxygen flux or any other considerations under the give assumptions. However, they only modeled the reactive case with simple configurations but did not consider a staged introduction of the fuel. Thus it is not conclusive from this study that reactive configuration is useless. A study like this provides more insight into selection of configurations for the membrane reactor.

As mentioned above, a monolith is a common reactor configuration. Sundkvist et al [94] built a monolith reactor as depicted in Figures 2-15a,b for oxygen separation from air using

inert gas. The main component of the reactor consisted of 2.2mm width square channels. Porous walls of ~0.5mm were coated with ~50μm dense membrane. The total effective area was $540m^2/m^3$ monolith volume. All parts of the module except the sealant were made from the same material. As seem in Figure 2-15a, the channels needed two complicated distributor units to distribute the sweep gas and feed gas to different channels. The test using counter-current flow showed a highest oxygen flux at $2.8ml/cm^2/s$ and an oxygen concentration of 28% in the sweep gas at 850°C operating temperature. The monolith configuration has a high area to volume ratio and is easy to scale up. But the issue with the design is the difficulties in flow distribution and sealing. The other similar reactor configuration was explored by Pan and Wang [95]. The reactor built was call "plate-fin" reformer by the authors, which was basically the same concept as monolith reactor with cross flows as shown in Figure 2-16. The reactor was designed so that the heat needed for methane steam reforming can be supplied by methane partial oxidation form adjacent channels. The design considered the heat exchanging aspect of the process but did not consider the mass transfer which is important for ion transporting membranes.

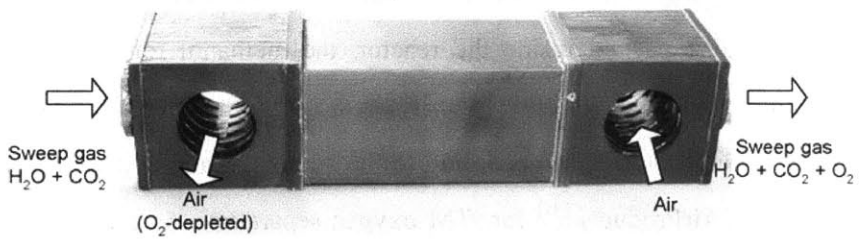

Figure 2-15a. Monolith reactor with counter-current flow (Picture from Sundkvist et al [94])

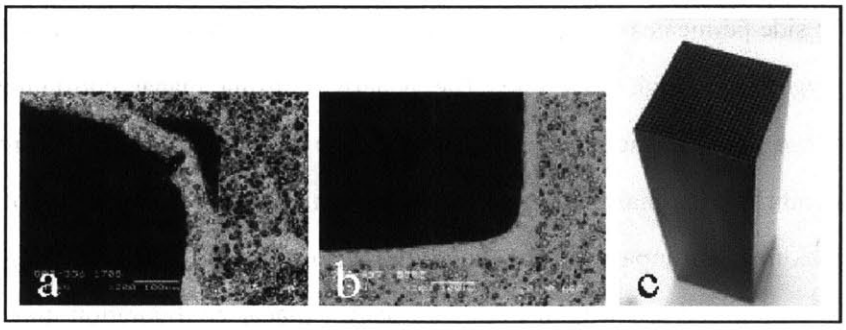

Figure 2-15b. Monolith reactor with counter-current flow. (Picture from Sundkvist et al [94])

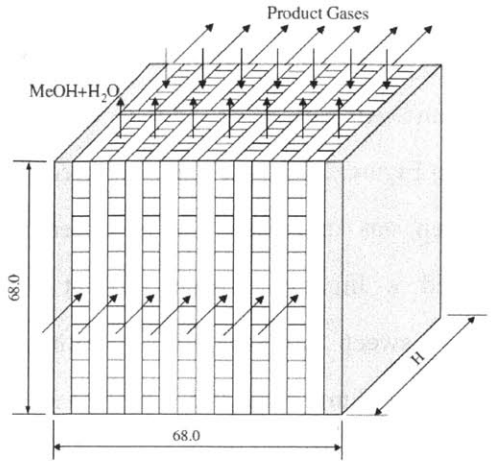

Figure 2-16, cross flow reactor for methane steam reforming (Picture from Pan and Wang [95])

Besides monolith type of reactor, the other type is planar. Figure 2-17 shows a planar reactor that resembles a pan-cake stack, which was used by Han et al [96] for hydrogen production from methanol steam reforming. The module was designed for vehicle on-board fuel cell with the capacity of $10Nm^3/h$ hydrogen. The reactor used Pd-Cu alloy foil and diffusion bonding the foil onto the unspecified metal frame. The operating pressure of the module was 10atm and the operating temperature was 350°C. With the use of $CuO/ZnO/Al_2O_3$ catalyst packed inside the reactor, the methanol reforming at the above mentioned conditions yielded 99.9995% purity hydrogen. The thermal efficiency of the reforming process was 81% to 82% according to the authors. Another planar reactor design was implemented by AirProducts [97] for ITM oxygen separation. As can be seen in Figure 2-18, the dense ceramic membranes were attached to porous support with metal rigs. The gas outside the cells is air at high pressure. At 900°C, the oxygen from the air in the high-pressure side permeates to the inside of the cells. This method produced higher than 99% purity of oxygen at a high flow rate. The benefit of using planar configuration is the robustness of the structure and the ability to easily scale up. With the high pressure difference across the membrane, the planar reactors can create a high flux. However, the total effective area is not maximized compared to the monolith reactors. Also if a sweep gas is used, as in the case of the proposed application in this thesis, the planar configuration may need more design adjustment before being used as the CO_2 reusing reactor.

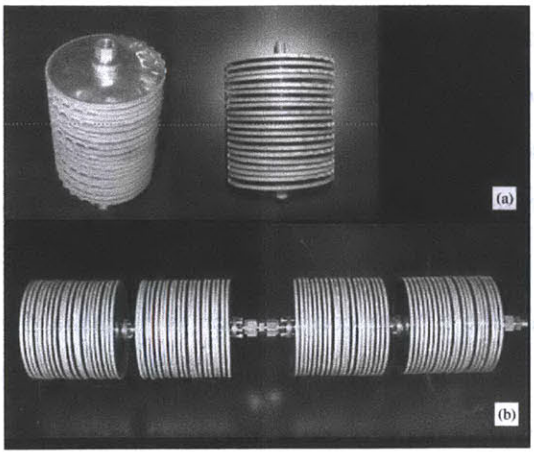

Figure 2-17, Planar configuration (Picture from Han et al [96])

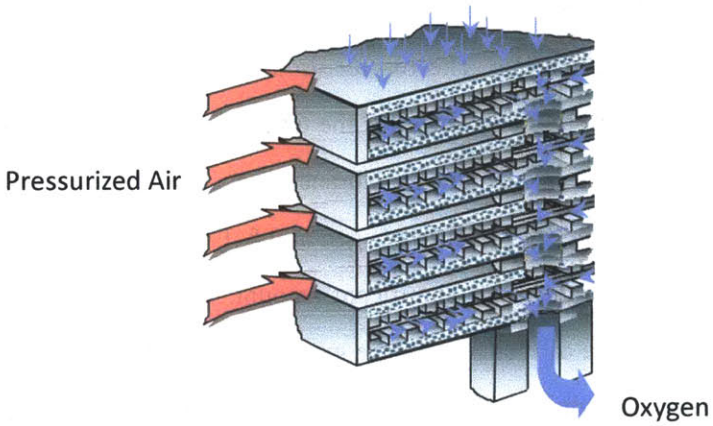

Figure 2-18, The planar membrane reactor design (Picture from AirProducts [97])

The third type of reactor configuration is tubular reactor. Silvano et al [98] investigated the use of a "finger-like" tubular Pd reactor used for ethanol steam reforming to produce hydrogen (Figure 2-19). The catalyst used for the reaction was Rh and the tubes were fabricated using cold rolling and diffusion welding of metal foils. The wall thickness of the Pd-Ag membrane was 50-60μm, the diameter of the tubes was 10mm and the length was 150mm. The authors proposed two set-ups for the methanol steam reforming, one with the catalyst outside the membrane tubes and one with the catalyst inside the membrane tubes. The authors chose to put the catalysts inside the tubes and operated at 650°C and 2atm pressure inside the tubes. Hydrogen was collected with N_2 sweep gas outside the tubes. Though two set-ups are possible for this configuration, from the mechanical point of view, it

is better to choose feed gas inside the tubes in the case of metal membrane. Because the metal tubes are stronger under extension so that they can sustain higher internal tension than compression. In the case of dense ceramic membranes, it is known that ceramic is stronger under compression than tension. Thus a higher pressure feed gas outside the tubes and sweep gas inside the tube will be more appropriate for the proposed CO_2 method. Compared to the other two configurations, the tubular configuration is mechanically stronger. However, the low surface area to volume ratio is the disadvantage of the design. To increase the area/volume ratio, hollow fiber reactors can be used.

Tan et al [99] built a hollow $La_{0.6}Sr_{0.4}Co_{0.2}Fe_{0.8}O_{3-\alpha}$ fiber reactor for oxygen separation. The reactor was consisted of 889 hollow fibers membranes that were 28-32cm in length, 1.8mm OD and 0.6mm wall thickness. The reactor used the same configuration as seen in Fgiure 2-19 but used hollow fiber membranes for the tubes. Vacuum was used to extract the oxygen permeated from the air inside the membrane tubes. Tan et al reported 1167h of operation at 960°C that produced 99.4% pure oxygen at 0.84L/min. The hollow fiber reactor increased the area to volume ratio by a significant amount. However, the scaling of fiber reactors is not effective because of the temperature gradient in the furnace. The sealing of the fibers also created impurity in the oxygen because the sealing between the membrane tubes and fiber produce more leakage as more and more fiber membranes are used. Thus, even though the hollow fiber membranes are able to produce high flux, there are many problems that need to be addressed.

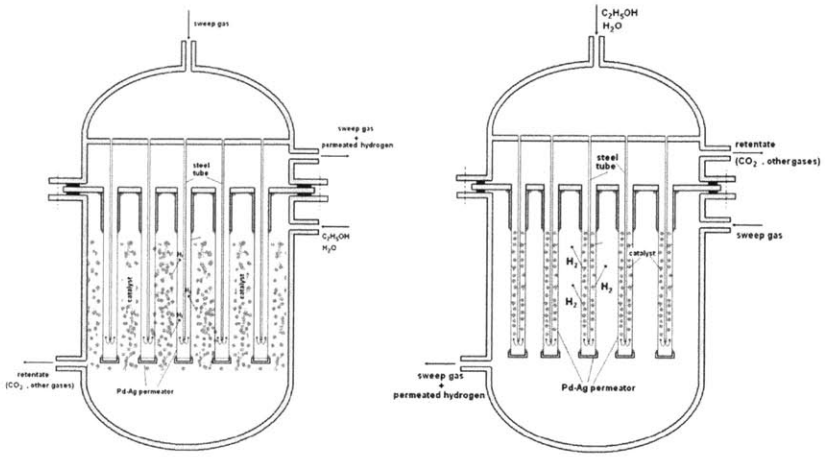

Figure 2-19, The "figure-like" tubular reactor configuration. Left: catalyst outside the tubes. Right: Catalyst inside the tubes. (Picture form Silvano et al [98])

To summarize, possible reactor configurations for CO_2 reuse membrane reactor has been reviewed here. The three categories of reactors, monolith reactors, planar reactors and tubular reactors all have their advantages and disadvantages. The comparison of three categories is summarized in the table. Hollow fiber membrane reactor is also included as a type of tubular membrane reactor. The five aspects to be considered are: area/volume ratio, mechanical strength, scalability, sealing and complexity. The importance of scalability and sealing performance is self-explanatory. It is also critical to have high area/volume ratio and good mechanical strength so that the system can provide large reactive area and support thin membranes. On the other hand, the reactors should be simple so that it will save the construction cost and maintenance cost. In the end, no matter what kind of reactor is chosen, reactor simulations and cost analysis must be performed during the R&D stage of the reactor to evaluate the possible membrane reactor design.

Table 2-6 Comparison of reactor configurations

	Area/Volume Ratio	**Mechanical Strength**	**Scalability**	**Sealing**	**Simplicity**
Monolith	High	Medium	Medium	Medium	Medium
Planar	Medium	High	High	High	High
Tubular	Low	High	Medium	High	High
Hollow Fiber	High	Low	Medium	Low	Low

Chapter 3. Experiment

The membrane used in this research is a $La_{0.9}Ca_{0.1}FeO_{3-\delta}$ (LCF) membrane provided by CeramTec® with 0.89mm thickness and 16mm diameter. The goal of testing this membrane is to:

1. Obtain data describing the membrane performance under inert sweep gas conditions and compare it with numerical simulations. This helps us understand the behavior of the membrane and to obtain the membrane's basic parameters. Furthermore, the comparison between numerical data and experimental data verifies the fluid behavior in the numerical simulation.

2. Obtain data for the membrane performance under fuel assisted oxygen permeation and compare with numerical simulations. This helps to identify the reactions that happen during fuel assisted oxygen permeation by verifying the numerical simulation model.

3. Conduct water-splitting experiments under inert sweep gas conditions and fuel-assisted conditions. These experiments are important to prove the concept of the proposed CO_2 reuse because the essential step in reusing the CO_2 is to produce H_2O through water splitting. The comparison between data from the previous two types of experiments will give us insight into the mechanism behind water splitting.

To perform the above-mentioned experiments, a button-cell type reactor was built in the Reacting Gas Dynamics Laboratory. This chapter describes the design of the reactor system, the experimental set-up, the experimental procedures and the methodology used to analyze the results.

3.1 Experiment Set-up

3.1.1 Reactor Design

Two alumina tubes 8.5" long, 0.75" OD and 0.5" ID act as the feed gas and sweep gas reactor chambers with the membrane between them (Figure 3-1). In Figure 3-1 only the central parts of the reactor assembly is shown. This includes the 0.75" OD alumina tube, the 0.25" OD alumina inlet tubes, the membrane, the outlet gas tubes and the thermocouple ports. The main body of the reactor is symmetric with the membrane plane. A compression fitting cross adapter is used on each side of the reactor to connect to the exhaust. Also connected to the cross adapter is the entrance port for high temperature thermocouples. The thermocouples, sampling valves and exhaust tubes are not shown in the figure. Alumina tubes used as the reactor chamber and the gas inlet tubes because of their high melting point and stability in high temperature. The upper alumina tube has its outer diameter reduced to 0.64" throughout a 0.2" long section from the top (Figure 3-2a). The lower alumina tube has its inner diameter bored to 0.64" from the top to 0.2" depth (Figure 3-2b). The two modified ends of the alumina tubes create an inter-locking joint as it is illustrated in Figure 3-3. Two alumina tubes are inter-locked to each other so that the membrane sits between them. During the experiment, the membrane and gold ring seals are placed in the bore of the tube in Figure 3-2b. This feature insures the convenience of alignment and a better sealing performance.

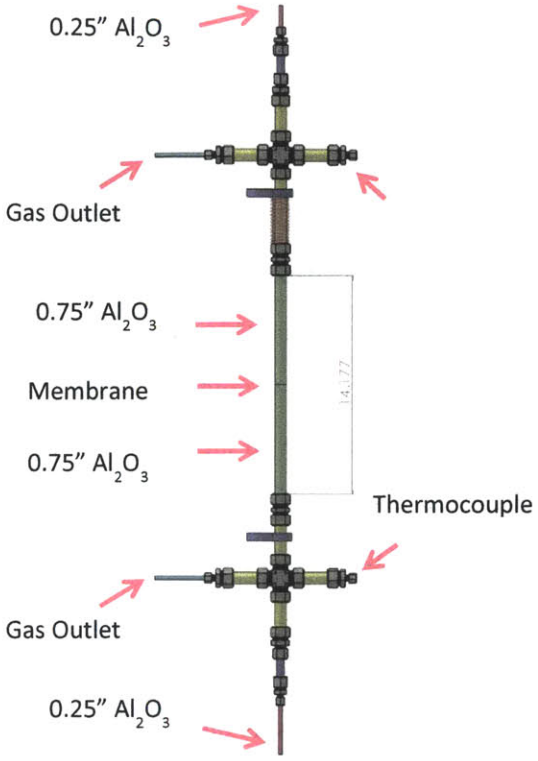

Figure 3-1 Reactor assembly the central parts

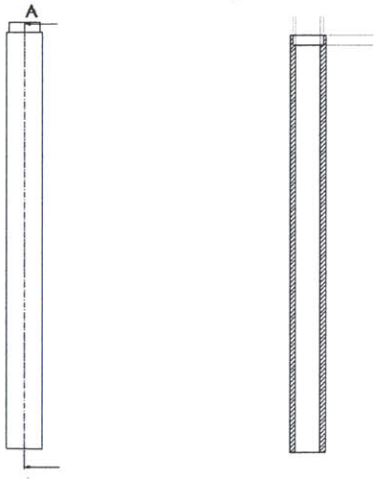

Figure 3-2a Figure 3-2b

Figure 3-2 Alumina tubes

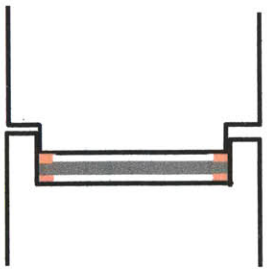

Figure 3-3. Inter-lock mechanism. The membrane sits between the alumina tubes.

To ensure positive contact between the sealant, the membrane and the alumina tubes, the upper alumina tube is pressed down by a spring from the upper cross bar while the lower alumina tube is fixed. A schematic of the chamber configuration is shown in Figure 3-4. The gases are fed into the alumina chamber by two 24" long alumina tubes with 0.25" outer diameter and 0.187" inner diameter. In this way, only the alumina parts, the membrane and the sealant are heated in the furnace. The alumina tubes are connected to stainless steel tubes outside the furnace using Swagelok® ultra-torr vaccum fittings as shown in Figure 3-5a and Figure 3-5b. The two alumina tubes that act as membrane chambers are connected with 0.75" ultra-torr fittings and the two 0.25" gas inlet tubes are connected to 0.25" ultro-torr fittings. These fittings have rubber o-rings inside so that when they are tightened, the o-rings will compress and establish gas tight seals.

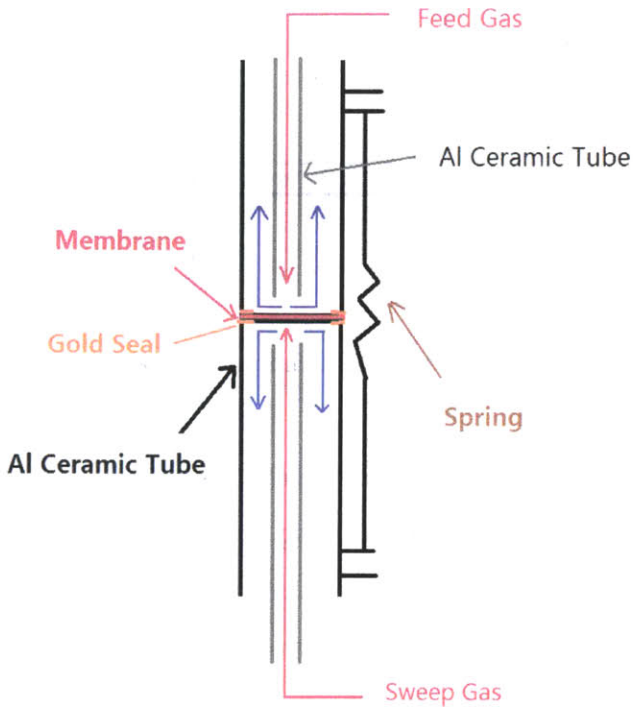

Figure 3-4. Reactor chamber illustration

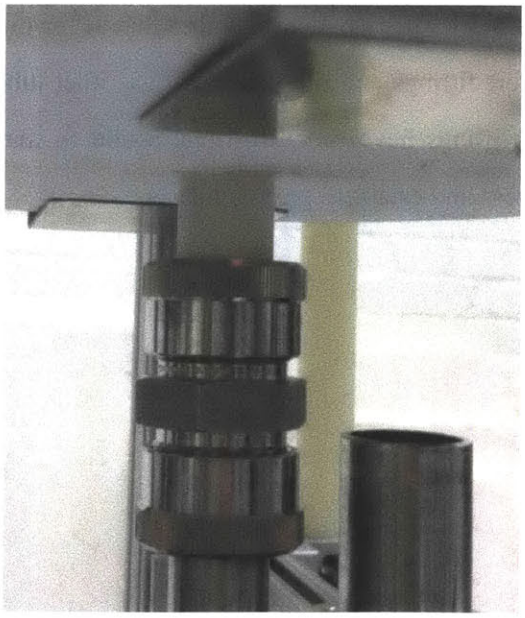

Figure 3-5a Figure 3-5b

Figure 3-5a. Vacuum fittings on alumina feed tube connecting with stainless steel part.
Figure 3-5b. Vacuum fitting connecting alumina tube chamber to the stainless steel tube.

The upper body and the lower body of the reactor are each held by an 80/20® aluminum bar mounted horizontally (Figure 3-6). Both of the two horizontal cross bars are mounted on one vertical 80/20 aluminum bar. Each of the cross bar is connected to the vertical bar by a UniBearing® provided by 80/20®. In this way, the two cross bars are connected to one reference plane, so that they can be easily aligned. Each half of the reactor tubes is held vertically by another UniBearing® connector and a pair of clamps.

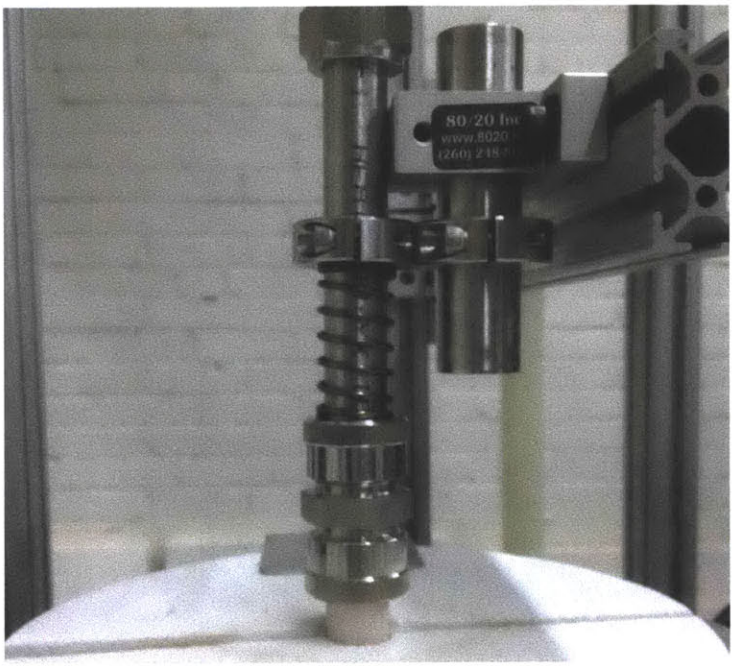

Figure 3-6. The figure shows the cross bar and base that holds the upper part of the reactor. Spring loading presses the upper alumina tube down.

The furnace used in the experiment is an ATS® 3210 tubular furnace, which operates at temperatures up to 1200°C. The control unit of the furnace offers simple ramp functions and it gives temperature readings from a K-type thermo couple. It has one heating zone in the middle of the furnace. The furnace has a tubular opening of 12" long and 1" OD to allow the alumina parts of the reactor to be heated in it. The furnace is mounted on the reactor bench with 80/20 aluminum supports (Figure 3-7).

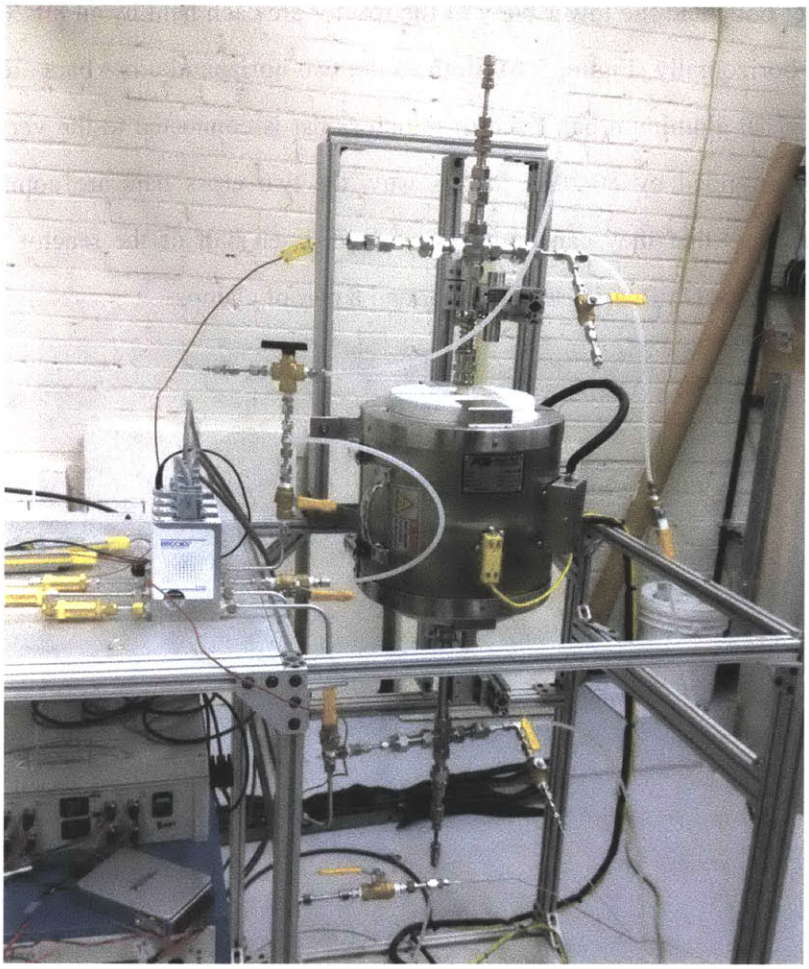

Figure 3-7. Reactor assembly and furnace

3.1.2 Connections

Figure 3-8 describes the flow chart of the system in this experiment. There are in total four Brooks® GF40 mass flow controllers used to control the gas flows. The MFC can be configured to flow different gases. The feed gases are controlled by two MFCs, and one of the MFC from the feed gas is connected to a Saturator with a by-pass valve. If the experiment needs water vapor in the feed gas, as in the case of the water splitting experiments, the by-pass valve can be connected to the saturator. A Fideris® bubble humidifier is used as the saturator. The humidifier can achieve a relative humidity up to 100% and bulk temperature up

to 95°C. Heat tapes are wrapped around the tubes that come out from the humidifier to prevent condensation. As can be seen in Figure 3-9, ceramic fiber insulators and aluminum foils protect the heat tapes for insulation and safety considerations. Before the sweep gas and feed gas go into the reactor, a three-way valve is installed to switch the inlet gases between the GC (gas chromatography) sampling and reactor feed gas. The outlets from the sweep side and feed side of the reactor are connected with the three-way valves also to switch between GC sampling and venting.

The gas sampling tubes from the reactor are connected to a 0.125" VICI® multiposition valve, which can select the sampling inlet from different sources and has only one outlet going to the GC. Before the sample gases go to the GC, they must be deprived of any water vapor to prevent the GC columns from water damage. Two dryers are installed in line to complete this task. The first drier is a Perma Pure® MD series counter flow membrane drier. To enable drying, the MD drier needs a dry airflow in the direction opposing the sample gas. The dry airflow is created by a compression air driven vacuum pump that draws room air through a desiccant air dryer. By going through the MD counter flow drier, the water vapor from the sample gas is driven to the dry air side of the membrane drier. The second dryer installed in line immediately upstream to the GC is Genie® 170 Lab series membrane separator. This dryer allows only dry sample gas to permeate through its membrane, some sample gas and remaining water vapor is discharged to air through a bypass port. By passing the sample gas through these two driers, it is guaranteed that water vapor is depleted before the sample gas enters the GC.

During the water splitting experiments, the water concentration in the gas is so high for the two above-mentioned dryers so that an alternative dryer set-up is used. In this set-up, indicating silicone gel desiccants are packed into a 24" long, 3/8" OD plastic tube. The plastic tube is connected with the outlet of the sampling valve and the inlet of the GC. The silicone gel desiccants change color when they are saturated so that they can be replaced in time. This simple setup of desiccants makes sure that the sample gas to the GC is dried after passing through the desiccants.

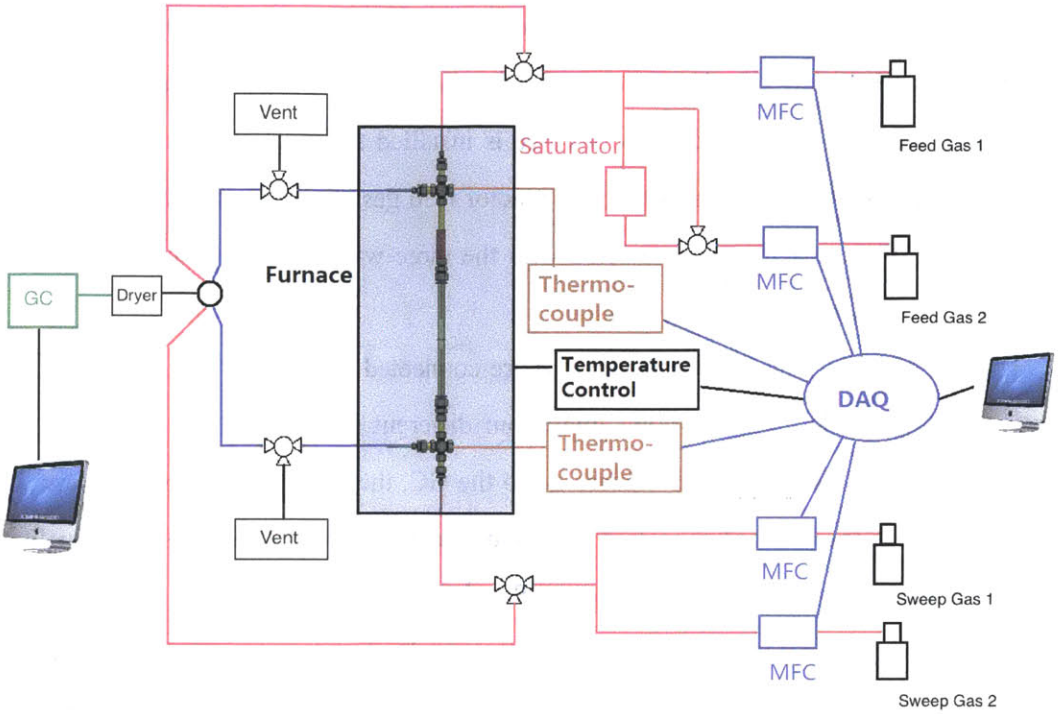

Figure 3-8. Flow diagram of the system

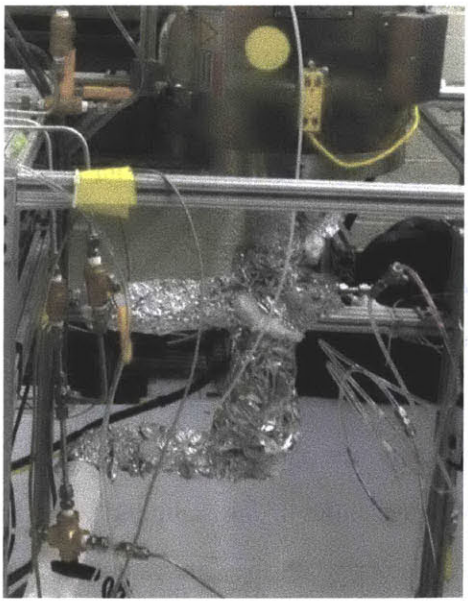

Figure 3-9. Heated line and insulation.

3.1.3 Instrumentation and Data Acquisition

The parameters to be controlled in this experiment are the flow rate Q_{in} of the sweep gas and the feed gas, the temperature T inside the furnace, and vapor pressure P_{H2O}. The variables to be measured are the temperature at four points near the membrane surface, the mass flow rate readings from MFC's and the composition of inlet and outlet gases measured by the GC.

To read the temperature and mass flow rate signals, USB-6009 National Instrument® data acquisition card is used. Another data acquisition card National Instrument® cDAQ-9171 sends 0-5V voltage signals to the four MFC's to control the mass flow rates.

The gas flow rates are controlled by the Brooks® GF40 mass flow controllers, as mentioned previously. Gas types and flow rate ranges can be configured through a diagnostic pin on the MFC's. The 0-5V mass flow rate reading signal and 0-5V setpoint control signal are received and sent through RS485 cables connected to the DAQs. A home-made control box (Figure 3-10) supplies DC power to the MFC's and sends control and reading signals to and from the MFC to DAQ cards.

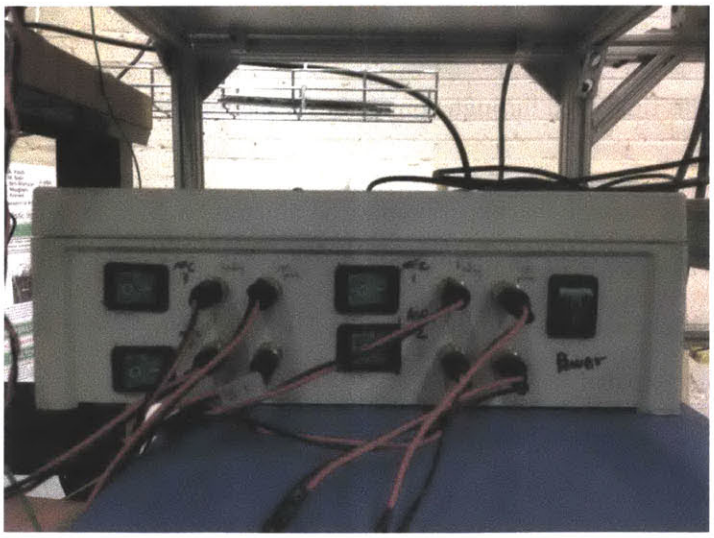

Figure 3-10. Control box. Each MFC has a power switch, a set-point input and a flow rate reading output.

Four Omega® Super OMEGACLAD® thermocouple probes are installed in the reactor. Theses thermocouples can measure temperatures up to 1300°C. The thermocouples are 24 inches long and so that the measuring tips can reach near the membrane surface from outside

the furnace through compression fittings. The tips of the thermocouples are placed at four different places in the reactor tube along the axis. On each side of the membrane there are two thermocouples. It this way, the temperature profile created by non-uniform temperature distribution in the furnace can be captured and the true temperature of the membrane can be interpolated. As shown in Figure 3-11, the thermocouples are inserted into the gas chambers through two gas tight Omega® feed-through connector on each side of the reactor. The signals are converted from analog to digital data using Omega Super MCJ® converter.

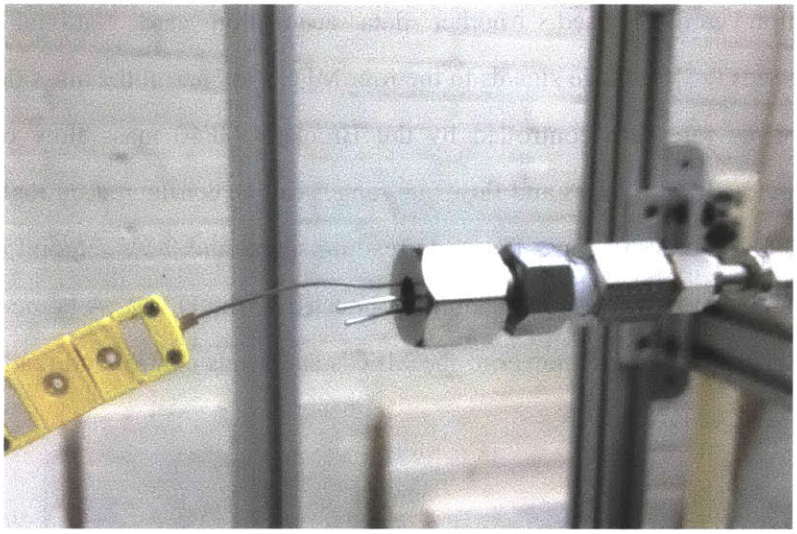

Figure 3-11. Gas tight feed through connector for the high-temperature thermo couple.

To monitor and control the experimental parameters, a Matlab graphic user interface (GUI) was built as shown in Figure 3-12. The data from the MFC's and thermocouples plotted over time in the windows on the left. The MFC flow rates and readings can be control on the right-hand-size panel.

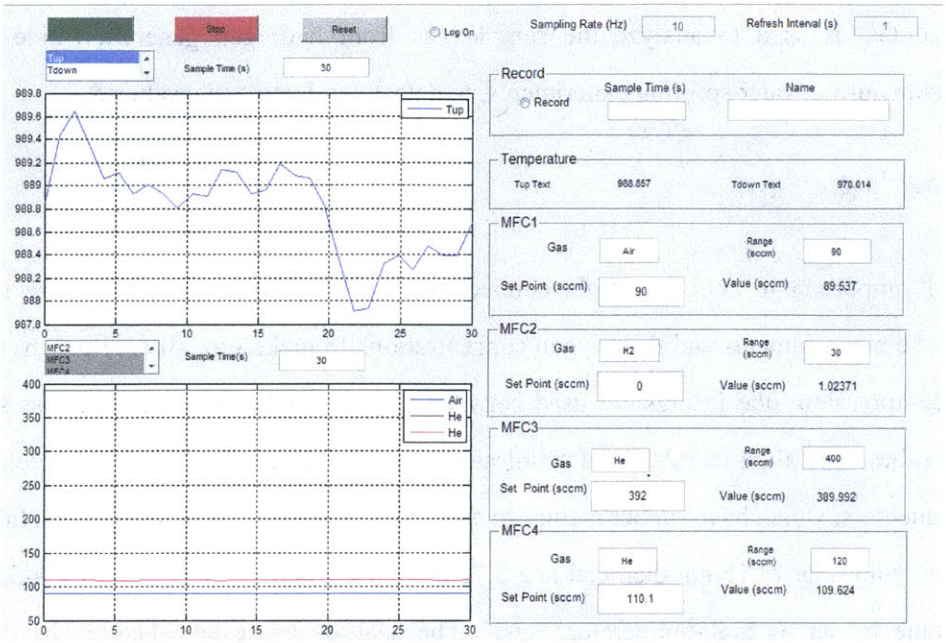

Figure 3-12. Matlab GUI for control of gas flow rates

During the water splitting experiments, steam is introduced into the inlet gases by flowing the inlet gases through a Fideris® bubble humidifier. The humidifier can achieve a relative humidity up to 100% and operate at temperature up to 95°C. Heat tapes are wrapped around the tubes that come out from the humidifier to prevent condensation.

Finally the sample gases are analyzed by the gas chromatograph. Two GC's are used in this experiment. To analyze gas samples from experiments that do not involve water splitting, Agilent 490 micro GC was used. The micro GC can analyze gas samples in a relatively short time (3-4 minutes) with high accuracy in O_2, N_2, and CO measurements. The sensitivity of measurements was 50-100PPM and the accuracy, according to our test, was about 0.8% of the reading. While the Agilent GC gives relatively high accuracy and quick readings, it does not have good hydrogen measurement accuracy. Thus the second GC, Shimazu 4950 was used for detection of hydrogen. While this GC requires longer processing time for every measurement (16-17 minutes), it has a high sensitivity and accuracy when measuring gases that contain low hydrogen level thanks to its PDHID detector. The detector can measure hydrogen concentration lower than 50PPM, however, hydrogen concentration higher than 500PPM will saturate the column. The highest hydrogen concentration seen in the water splitting experiment is 10~100PPM, which is within the limit of the Shimazu GC. The

Shimazu GC is used to analyze the sample gas from hydrogen generation side of the membrane during water splitting experiments, to detect any hydrogen produced.

3.1.4 Sealing

It is important to apply gas-tight connections throughout the reactor because leakage affects the measurements and the oxygen concentration. To make sure all connections are gas tight, compression tube fittings are used between stainless steel tubes and stainless steel to plastic tubes. The alumina tubes and stainless steel tubes are connected by Swagelok® ultra torr connectors, which have rubber o-rings to ensure gas-tight fittings to the alumina tubes.

Two gold rings of 15mm diameter and 0.75mm thickness were placed on each side of the membrane to act as high-temperature seals. The sealing was established by heating the reactor at a 180°C/hr ramp rate until 1020°C and remain the temperature for 30min-60min. During the sealing, 100sccm He runs through the sweep side of the membrane and 90sccm air was fed to the feed side of the membrane. Gas samples are taken at the outlet of the sweep side to monitor the O_2 and N_2 concentration. The gold seal is successfully established when less than 0.5% N_2 is detected in the outlet gas from the sweep side at 990°C. At this point, further improvement of the sealing is difficult, since the leak detectors cannot detect the trace amount of gases diffusing out of the reactor.

3.2 Experimental Methodology and Procedures

It is critical to have consistent and repeatable results from the experiments, thus one must be careful to apply the same procedure during each experiment. The following sections describe the procedures used in different tests.

3.2.1 Sealing

The sealing between the membrane and the reactor chamber, i.e. the alumina tubes, must be established before any tests are done. The following procedures are followed in this process:

1. Place the O-rings and membrane in the reactor. One O-ring is underneath the membrane and the other is above the membrane. The membrane and O-rings are placed between two 0.75" alumina tubes as illustrated by Figure 3-2. The spring on the upper half of the reactor is compressed to pressurize the connection between O-rings and the membrane.

2. Heat the furnace to 1030°C. The heating rate is 3°C/min. During heating, there is no gas flow into the reactor thus the only gas in the reactor is air.

3. At 1030°C, the gold is softened for 30-60mins. 90sccm air is fed to the feed side of the membrane and 100sccm He to the sweep side. The purpose of feeding air and He is to remove the remaining air in the sweep side of the reactor and prepare for measurements. Also, the nitrogen level in the sweep side can indicate if the sealing is established.

4. Cool the reactor down at 3°C/min until the membrane temperature is 990°C. 990°C is the temperature at which we always check if the flow rate matches with previous experiments. When the membrane temperature reaches 990°C, the sweep gas outlet composition is sampled to check any air leakage. The seal is considered successful when N_2 concentration is less than 0.5%. If the seal is not successful, steps 2-4 will be repeated.

The sealing process is required only when a new membrane is inserted into the reactor. Once the gold O-rings seals are established, the only way to destroy them is to heat the reactor to softening temperature of gold.

3.2.2 Inert Gas Permeation Experiments

The inert gas test uses air as the feed gas and inert gas as the sweep gas to test the oxygen permeability of the LCF membrane. The data from inert gas permeation tests will be used in simulations to characterize the membrane. The inert gases used are He and CO_2. In this case CO_2 is considered inert because it will not react with the permeated O_2 thus acts as an inert gas. The procedure in these tests:

1. Heat the membrane to 990°C under 100sccm inert gas and 90sccm air. Take samples of outlet gas on the sweep side of the reactor to compare with previous experiments and check the consistency of the results. If the results do not match previously determined results within experimental errors, the experiment will not continue until the reason of inconsistency is found out and resolved.

2. Change the temperature and gas flow rates to the targeted sampling set points. The sweep gas flow rates always starts from the highest to the lowest while the air flow rate is maintained the same. The temperature always starts from the highest value to the lowest. After reaching the lowest flow rate, or lowest temperature, the flow rate or temperature is raised again to one or two of the previous set points to check the consistency. The reason of this procedure is that the membrane takes time to reach steady state at each set point condition. This procedure makes sure that the data are taken when the oxygen permeation flux is settled to stead value.

3. At the end of the experiment, the membrane is cooled down to room temperature at 3°C/min cooling rate with the gases shutdown.

3.2.3 Fuel Assisted Permeation Experiments

The fuel assisted permeation tests are performed to compare the membrane behavior under fuel assisted air permeation and fuel assisted water splitting. This comparison will provide insights into the mechanism behind membrane water splitting. The sweep gas that

has been used so far in the test is H_2/Ar and the feed gas was still 90sccm air.

1. The first step in this test is to check the consistency with previous experiments. This is done by taking the samples at the same set point of 100sccm Ar/5vol%H_2 sweep gas and 90sccm air feed gas.

2. Similar to the inert gas permeation test, the set points always start from conditions of high oxygen flux to those of low oxygen flux. In this case, the set point conditions start from the highest hydrogen content to lowest and from the highest temperature to the lowest. After reaching conditions with the lowest oxygen flow rates, some tested conditions with higher oxygen flux are examined again to ensure data are taken at steady states.

3. At the end of the experiment, the sweep side is purged with Ar for 30min. Then the membrane is cooled down to room temperature at 3°C/min cooling rate with the gases shutdown.

3.2.3 Water Splitting Experiments

Three types of water splitting experiments are performed: 1. 200sccm of 50%Ar and 50%H_2 is used as the feed gas. 200sccm Ar and 400 sccm Ar are used as the sweep gas. 2. 200sccm of 50%Ar and 50%H_2 is used as the feed gas. 200sccm of 97.5%Ar and 2.5% CH_4 is used as the sweep gas. 3. 90sccm of 95% He and 5% H_2O is used as the feed gas. 100sccm of 5%H_2 and 95% He was used as the sweep gas.

1. Similar to the previous experiments, the first step is to check the consistency with previous experiments. The furnace is first heated to 990°C. Then 200sccm 50%H_2O/Ar is introduced to the feed side of the membrane while the sweep side is 200sccm Ar. The hydrogen production rate is compared to previous experiments.

2. During all three types of the water splitting experiments, the membrane was tested at 990°C, 950°C and 900°C. Each condition is tested with at least 5 samples before changing to the next condition. The reactor is tested for at least 3hr at each condition to reach equilibrium. Some set points are tested twice to verify the stability of the data.

3. At the end of the experiment, the reactor is cooled down at 3°C/min cooling rate. However, rather than cooling with gases shutdown, for water splitting experiments, dry air continues to flow on both sides of the reactor to purge remaining water vapors out of the reactor.

3.3 Methodology of Analysis

During the experiment, the GC measures the compositions of the outlet gases C_{i_out} and inlet gases C_{i_in} while the four thermocouples measure the temperature T_i near the membrane. The mass flow rate controllers control the total flow rate of sweep gas Q_{sweep} and feed gas Q_{feed}. To find the temperature of the membrane, distance-temperature plot is made and the temperature of the membrane is found, as shown in Figure 3-13. The positions correspond to the distance from the membrane surface and the negative value represent the positions below the membrane. In this particular example, the temperature at the intersection with vertical axis is 987°C, which is the temperature of the membrane. In later experiments conducted on water splitting reactions, the temperature was made more uniform by improving the insulation of the reactor at each end of the opening. In this later case the temperature profile looks like the plot shown in Figure 3-14, and the temperature of the membrane is more defined, with uncertainties within 1°C.

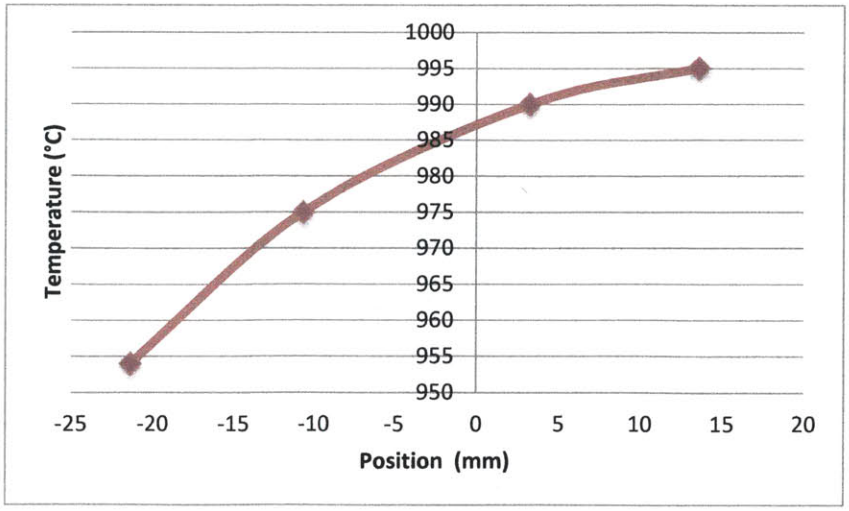

Figure 3-13. Temperature v.s. position in inert gas experiments. The y-axis intersection is the membrane temperature.

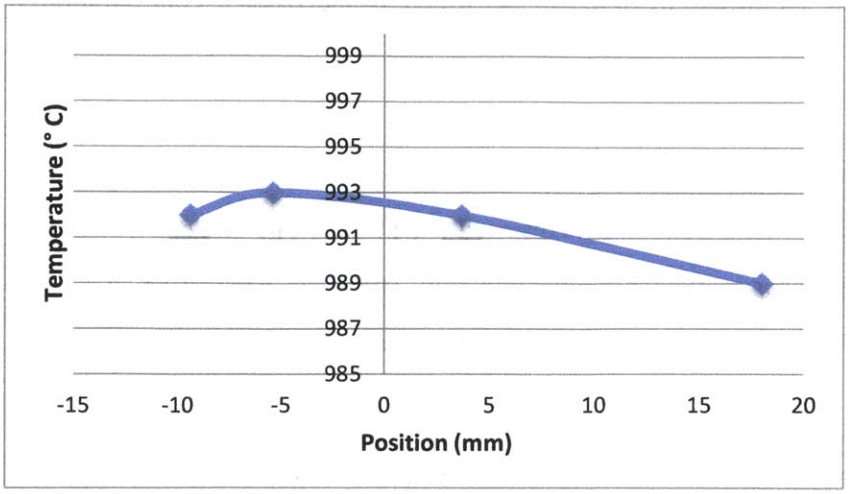

Figure 3-14. Temperature vs position in water splitting experiments.

Inert Gas Permeation Test

In the case of inert sweep gas oxygen permeation, the oxygen flux can be found from measurements of total sweep gas flow rate Q_{sweep}, outlet O_2 concentration in sweep gas $C_{O2_{o\_sweep}}$, and outlet N_2 concentration in sweep gas $C_{N2_{o\_sweep}}$. The measurement of $C_{N2_{o\_sweep}}$ is used to correct any extra oxygen detected because of air leakage.

$$J_{O2} = \frac{\left(C_{O2_{o\_sweep}} - 0.27 C_{N2_{o\_sweep}}\right) Q_{sweep}}{V_{molar} \pi r^2} \tag{3-1}$$

The V_{molar} is molar volume of ideal gas at 1atm, for which 24.5ml/mol is used. And r is the effective radius of the membrane, which is 0.635cm. The J_{O2} calculated from this expression has the unit of mol/cm^2/s.

Hydrogen Assisted Permeation Test

During hydrogen assisted permeation tests, both inlet concentrations of H_2 ($C_{H2_{i\_sweep}}$), and outlet concentrations of H_2 ($C_{H2_{o\_sweep}}$), and N_2 ($C_{N2_{o\_sweep}}$) are measured:

$$J_{O2} = \frac{\left(0.5 C_{H2_{i\_sweep}} - 0.5 C_{H2_{o\_sweep}} - 0.27 C_{N2_{o\_sweep}}\right) Q_{sweep}}{V_{molar} \pi r^2} \tag{3-2}$$

The oxygen flux is deduced from the change of concentration in hydrogen. Any oxygen leakage from air is combusted in the reactor. So the amount of oxygen found by hydrogen

reduction is subtracted by $0.27C_{N2\_out}$, which is the oxygen concentration from the air leakage.

Water Splitting Test

In water splitting tests, two fluxes need to be found. The first one is hydrogen production flux and the other is oxygen permeation flux. Hydrogen permeation flux can be found by detection of hydrogen concentration in the feed gas outlet:

$$J_{H2} = \frac{C_{H2Q\_sweep} Q_{sweep}}{V_{molar} \pi r^2} \tag{3-3}$$

The oxygen flux is thus $0.5J_{H2}$ by mass balance. On the other hand, J_{O2} can also be found by using the same methods used in inert gas permeation test (3-1) and hydrogen assisted permeation test (3-2). The results of J_{O2} using different methods will be used to cross check the consistency of measurements. However, due to the low oxygen permeation flux during the experiment, (3-3) is the most efficiency and accurate rate to check the hydrogen production rate with the Shimazu GC 4950.

3.4 Error Analysis

Error analysis must be done in the investigations of the experimental results because no matter how much effort is made to increase the accuracy of the measurements, there are always errors. These errors are not systematic errors that result from mistakes during the experiment, but rather, are uncertainties from the measurements.

The sources of errors in this experiment are:

E_Q: the error in total mass flow rate reading

E_{read}: the error in GC reading due to uncertainties of the GC

E_T: the error in temperature, because thermocouples are not directly measuring the membrane surface temperature.

E_{cal}: the error due to calibration of GC. As illustrated in Figure 3-15, this error comes from the uncertainty in measuring the calibration gas.

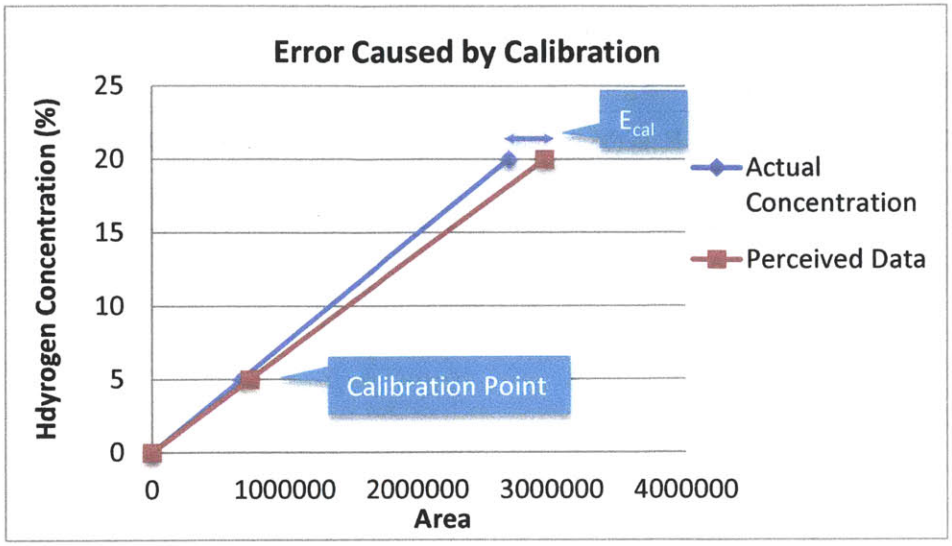

Figure 3-15. Error from calibration of GC

For example, to calculate the total error of the oxygen flux J_{O2} from the measurements, the error from different sources cumulate to one error in J_{O2}:

$$Error = \frac{\partial J_{O2}}{\partial Q} E_Q + \frac{\partial J_{O2}}{\partial C_{O2}} E_{read} + \frac{\partial J_{O2}}{\partial C_{O2}} E_{cal} + \frac{\partial J_{O2}}{\partial T} E_T \quad (3\text{-}4)$$

Here the partial differentials of J_{O2} can be found following the expressions in Equation 3-1 and 3-2. The error in temperature E_T is not included in this calculation because it does not appear directly in the calculations of J_{O2} from measurements. The error in temperature appears in the temperature-flux plot in the formal of x value errors. The effect of temperature error is on the calculation of pre-exponential factors of membrane parameters.

The error in mass flow rate E_Q is 0.5sccm. The error from GC calibration E_{cal} is 1% of the detected concentration while the error in GC reading E_{read} is 1% of the detected concentration. The error from temperature measurement $\frac{\partial J_{O2}}{\partial T} E_T$ is more difficult to determine since the temperature dependence of the oxygen flux is not explicit. The best way to determine is to first find the temperature dependence of the oxygen flux, then $\frac{\partial J_{O2}}{\partial T} E_T$ can be determined from the estimated $\frac{\partial J_{O2}}{\partial T}$. The error E_T in temperature is assumed to 5°C. As a result of these error calculations, error bars can be applied to each measurement. The values of the errors will be discussed in the next section.

The Table 3-1 summarizes the error sources and the values of these errors.

Table 3-1 Errors and their values

Error Source	E_Q	E_{read} (% of reading)	E_{cal} (% of reading)	E_T
Value	0.5sccm	1%	1%	5°C

Chapter 4. Results and Discussion

4.1 Sealing

The test on the effectiveness of the sealing was done by feeding 100sccm He on the sweep side and 90sccm air on the feed side. Figure 4-1 shows the detected oxygen leak from air and oxygen flux permeating through the membrane. The leak from air was calculated based on the N_2 detected from the outlet sweep stream. The oxygen flux was calculated by subtracting the detected leak from the total oxygen flow on the sweep side. The flow rate of the air oxygen leak is converted to flow rate per membrane area with the unit μmol/s/cm^2 so that the oxygen leak is comparable to the permeation oxygen flux.

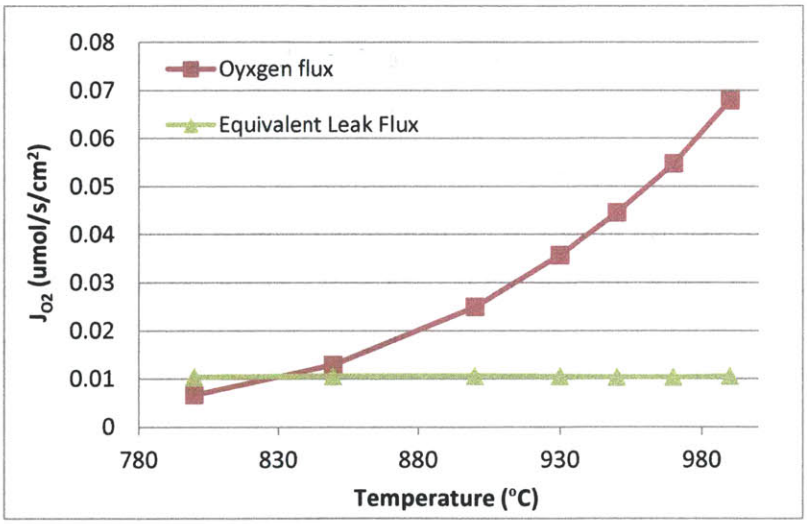

Figure 4-1. The oxygen flux excluding leak under varying temperature. The feed gas is 90sccm air. The sweep gas is 100sccm He.

As can be seen in the plot, the oxygen flux through the membrane was much higher than the flux of leak per unit area especially at high temperatures. In fact, the leak was 15% of the oxygen flux at 990°C. However, at lower temperature, the oxygen flux across the membrane became much lower. At about 830°C, the oxygen from permeation became less than the oxygen from leak, thus the data for temperatures below 850°C is not used for analysis. The leak was not influenced by the varying temperature and remained at a constant rate as long as

the sweep gas flow rate did not change. In Figure 4-2, the flow of oxygen leak in terms of the percentage of the total sweep gas flow rate is shown.

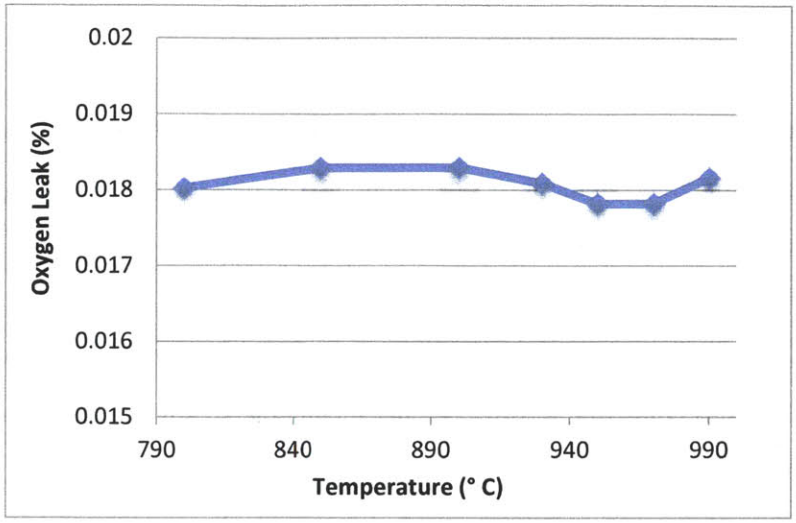

Figure 4-2 Percentage of leak to total sweep gas flow. The feed gas is 90sccm air. The sweep gas is 100sccm He.

Although the leak of oxygen from air is on a similar order of magnitude to the oxygen permeation, the percentage of leak to the total flow of sweep gas is quite small. As can be seen in Figure 4-2, when 100sccm He is used as the sweep gas only 0.018% of the total sweep gas flow is oxygen from air. Thus to further decrease the leak is a challenging task.

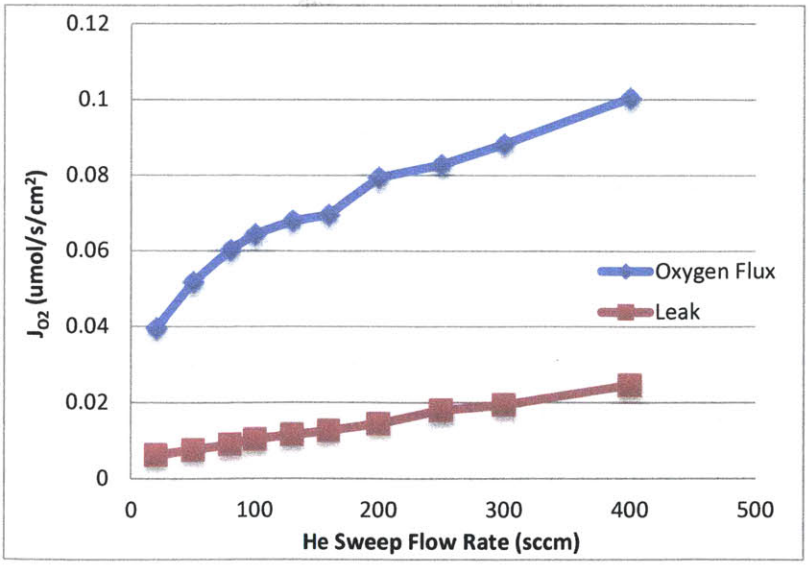

Figure 4-3 Sweep flow rate dependence of leak and the oxygen flux excluding leak. The feed gas is 90sccm air. The sweep gas is 20-400sccm He. T=990°C.

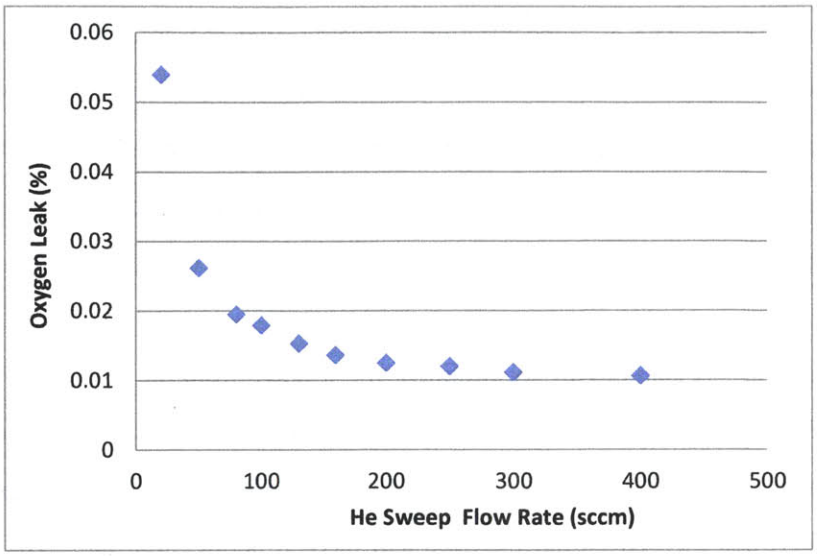

Figure 4-4 Percentage of oxygen leak to total flow of sweep gas. T=990°C The feed gas is 90sccm air.

Another fact about the leak is its flow rate dependence. The plot in Figure 4-3 shows the oxygen leak flux per membrane area as a function of the He sweep gas flow rate. The absolute value of leakage increases with increasing sweep gas flow. Figure 4-4 shows that the proportion of leakage in the sweep gas decreases with increasing sweep gas flow. At 20sccm He flow, the leakage of oxygen is 0.053% of total sweep gas flow and at 400sccm the leakage is only 0.01% of the sweep gas flow. On the other hand, the flux of leak increased from 0.0062 μmol/s/cm^2 to 0.024 μmol/s/cm^2 from 20sccm sweep flow to 400sccm sweep flow, which correspond to 15.8% and 24.5% of the oxygen permeation flux. Thus, while the greater amount of sweep gas dilutes the air leakage, the increased speed of sweep gas in the piping increases the mass transfer from air to the sweep gas.

The leak of air into the reactor does not come from a single source. Rather, it comes from multiple sources in the piping. This is evident when looking at the leak of air in hydrogen assisted permeation test. During the hydrogen assisted permeation test, gas samples are taken from two sampling points on the sweep side. The sampling points are shown in Figure 4-5. The inlet gases are sampled through a three way valve after the MFC and before feeding into the alumina inlet tube. The outlet gases are sampled after the gases exit the heated zone of the reactor which is inside the furnace. During the H_2 sweep gas experiments, the sweep gas was

Ar/H_2 at 100sccm and feed gas was 90sccm air at 950°C. Figure 4-6 shows the leak detected at the inlet and outlet. The N_2 concentration increased after the gases went into the heated zone and flew through the membrane surface. This indicates that some air entered the reactor through the connections after the inlet. Some air may have also entered through the gold ring seal between the membrane and the alumina tube. The exact place of leakage cannot be determined because the amount of leakage is so small that no leak detectors can detect the exact source.

Nevertheless, it is challenging to minimize the leakage from air in such an experiment. The detected N_2 can be used to correct the oxygen from air if one needs to determine the oxygen permeation rate. However, the oxygen from air must be considered when examining the relation between oxygen partial pressure and oxygen permeation rate. When evaluating the mass transfer from the membrane surface to the bulk gas, the measured oxygen partial pressure including leak is used as the bulk oxygen pressure.

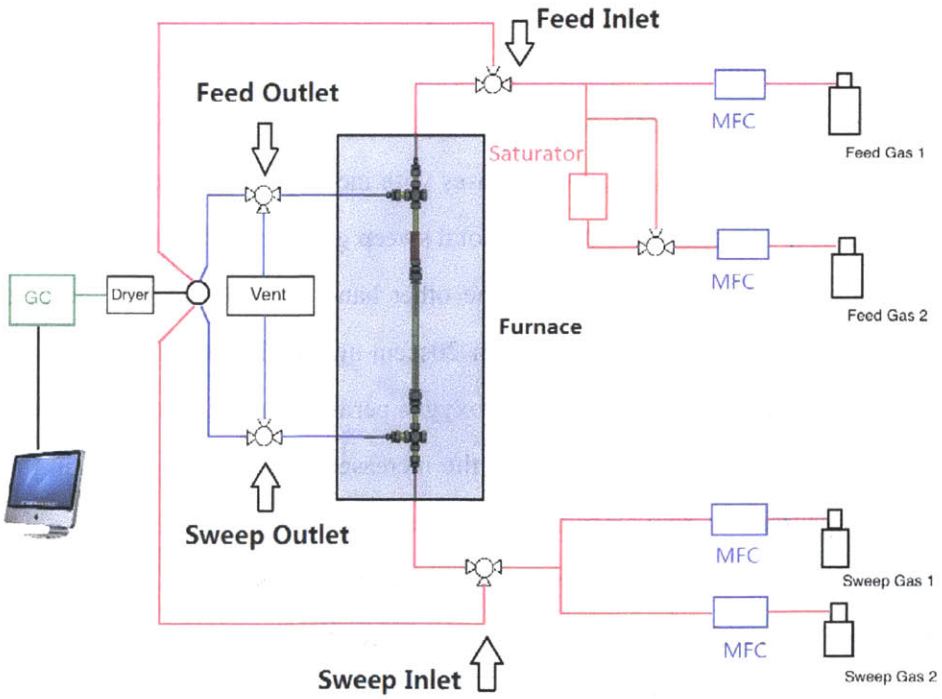

Figure 4-5 Diagram of the reactor and sampling points

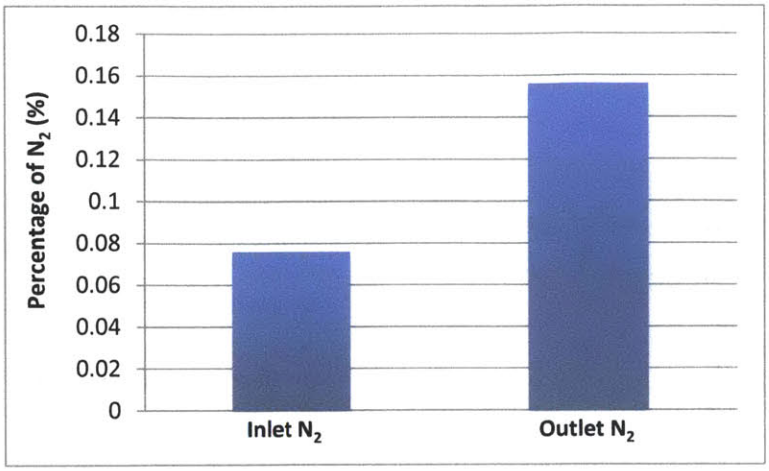

Figure 4-6 Leak detected during the hydrogen assisted permeation test in terms of percentage of total flow rate. The feed gas is 90sccm air. The sweep gas is 100sccm Ar/5vol%H_2. T=950°C

4.2 Inert Gas Permeation Experiments

The inert gas permeation experiments were conducted to determine the oxygen permeation characteristics of the membrane. Some tests were repeated several times to confirm the stability and repeatability of the results. Figure 4-7 shows the stability test during an experiment. The sweep gas was 100sccm He and the feed gas was 90sccm air. The test started at 990°C and samples were taken as the temperature decreased. At 932°C the decrease of the temperature was stopped and the furnace was heated up again. At each temperature set point, at least three samples with stable measurements were taken and the results were averaged. The plots show that the samples from increasing and decreasing the temperature had the same oxygen permeation rate. This proves that the oxygen flux was stabilized to equilibrium at the sampling points. The time taken for the membrane to reach equilibrium was less than 15min. If the equilibrium was not established when the samples were taken, the two plots would vary, with the fluxes of samples from decreasing temperature higher than those from the increasing temperature.

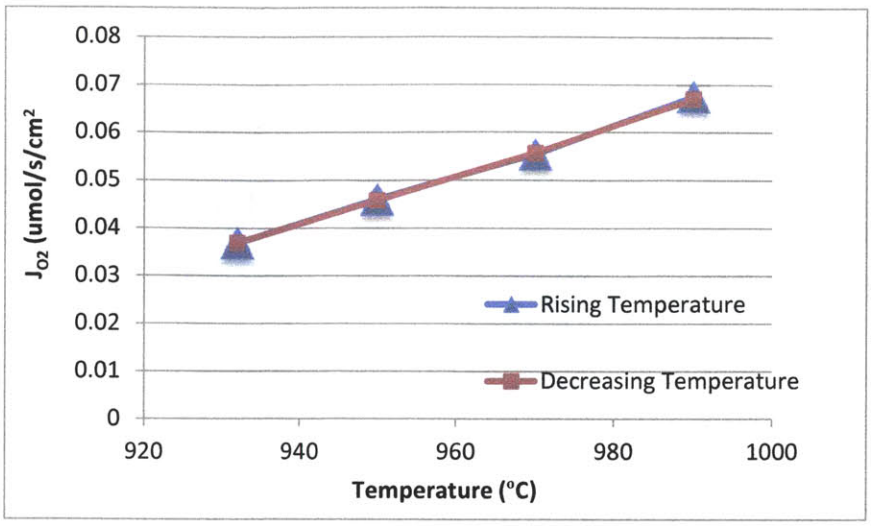

Figure 4-7 Air-He permeation stability tests. The feed gas is 90sccm air. The sweep gas is 100sccm He.

To verify the repeatability of the experiments, the tests were repeated during different heating cycles. During each heating cycle, the furnace is heated up from ambient temperature and is cooled down to room temperature after the tests are finished. Figure 4-8 shows the 90sccm air permeation test with He as the sweep gas at 990°C. The tests were done with the same set-up and the same LCF membrane and were repeated for four different heating cycles. As can be seen in the plot, there are variations in the measurement. However, the change of oxygen flux did not show any trend over time. The XRD analysis (section 4.5) of the membrane after experiments showed that the membrane material did not change during the experiments. Thus, rather than membrane property changes, the differences come from random variations in the experiment. Such variations include changes in calibrations of the GC, variations in the mass flow rate controls because of the changes in humidity and ambient temperatures, and membrane temperature differences. Table 4-1 shows the standard deviation and the errors from each source. One can see that the errors are close to the standard deviations of the measurements. Although there are variations on the oxygen flux from tests, the values converge to a single value, which signifies the repeatability of the experiments. Table 4-1 shows the measured values of the oxygen permeation flux from the tests. The standard deviations of the results were within 5% to 7% of the mean, which verifies the repeatability of the results.

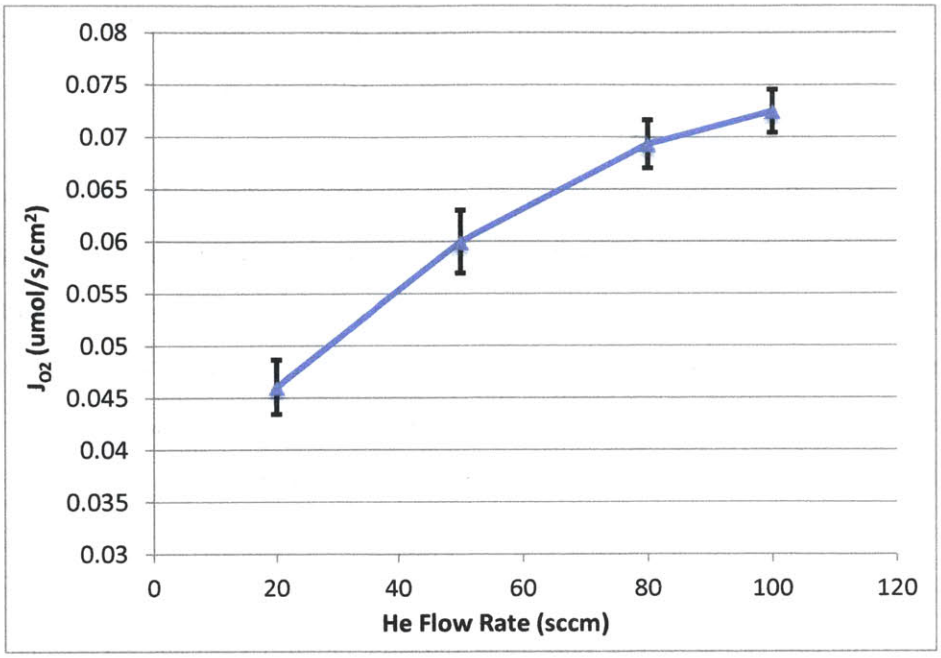

Figure 4-8 Air-He permeation repeatability tests. The feed gas is 90sccm air. The sweep gas is He. T=990°C

Table 4-1. Measurement table of flux at 90sccm air flow rate, 990°C. Units are μmol/s/cm^2

	100scm	**80sccm**	**50sccm**	**20sccm**
Mean	0.0679	0.0640	0.0557	0.0425
Stdev	0.0034	0.0038	0.0035	0.0028
Stdev/Mean	4.99%	5.97%	6.24%	6.66%
$\frac{\partial J_{O2}}{\partial Q} E_Q$	0.0003	0.002	0.0001	0.0001
$\frac{\partial J_{O2}}{\partial C_{O2}} E_{cal}$	0.0005	0.0002	00.0001	0.0000
$\frac{\partial J_{O2}}{\partial T} E_T$	0.0029	0.0029	0.0024	0.0020
$\frac{\partial J_{O2}}{\partial C_{O2}} E_{reading}$	0.0005	0.0002	0.0001	0.0000
Total Error	0.0042	0.0035	0.0028	0.0021

To test the temperature dependency of the LCF membrane, the temperature was changed while keeping the flow rates of the sweep gas and the feed gas constant. The flux of oxygen increased with increasing temperature. The logarithm of the oxygen flux and the inverse of

the temperature follow a linear relationship shown in Figure 4-9, which is the typical case for a chemical reaction. The line can be represented by an Arrhenius Dependence:

$$J_{o2} = Ae^{-E_a/RT} \tag{4-1}$$

Where J_{o2} is the reaction rate, A is a pre-exponential factor in μmol/s/cm^2, R is the ideal gas constant, and E_a is the apparent activation energy. Eq(4-1) is an empirical relation that can be used to describe the temperature dependence of the chemical reactions and the diffusivity of oxygen through the membrane. The plot in Figure 4-9 shows a nicely fitted correlation of Arrhenius form. The R^2 shown in the plot is the coefficient of determination, which is used to evaluate how good a fitting is. R^2=1 means a perfect, and R^2=0 means a totally irrelevant fitting. According to the fitting in Figure 4-9, the apparent activation energy E_a is 112kJ/mol under the given 90sccm air and 100sccm He flow rates. More interestingly, as shown in Figure 4-10, the slop of the curves increase as the flow rate of sweep gas He decreases. The apparent activation energy thus increases with decreasing sweep gas flow. The activation energy was 98kJ/mol, 113kJ/mol, 117kJ/mol and 125kJ/mol for 200sccm, 100sccm, 50sccm and 20sccm He flow rates respectively. Two values are found for the apparent activation energy under 100sccm He flow because the results were from measurements during different heating cycles and the experimental errors varied. The average of the apparent activation energy is 115kJ/mol under 100sccm He flow rate.

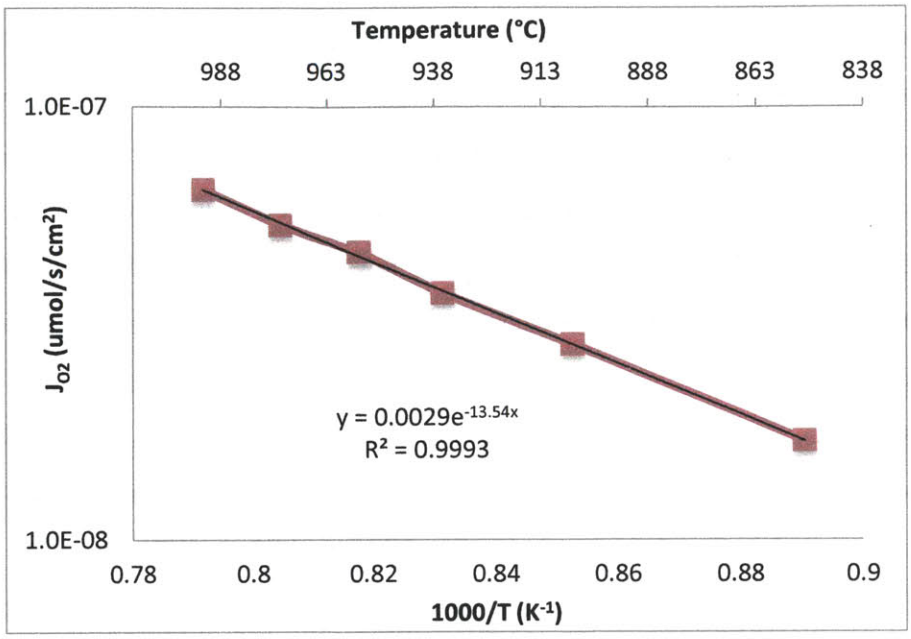

Figure 4-9. Temperature dependence of oxygen flux. The feed gas is 90sccm air. The sweep gas is 100sccm He. E_a=138kJ/mol

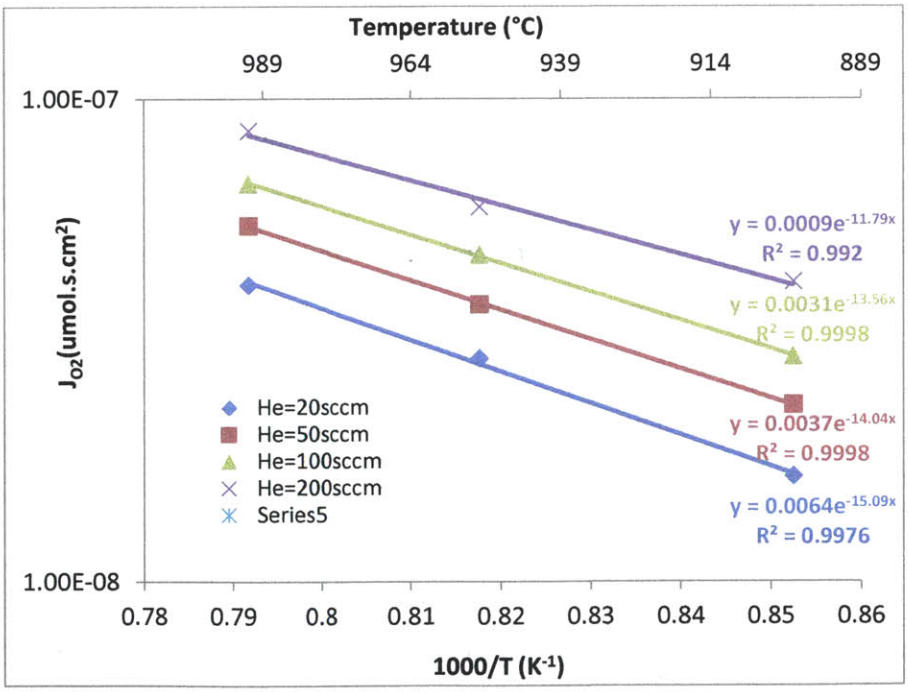

Figure 4-10.Temperature vs oxygen flux. The feed gas is 90sccm air.

Similar membrane oxygen permeation experiments were done by researchers on other perovskite membranes. For example, Xu and Thomson [104] tested a 1.65mm thick LSCF

membrane ($La_{0.6}Sr_{0.4}Co_{0.2}Fe_{0.8}O_{3-\delta}$) in a button cell reactor. The apparent activation energy with air as feed gas and pure N_2 as sweep gas was 119kJ/mol to 191kJ/mol, and the membrane experienced a change in apparent activation energy at about 860°C. The Sr in the LSCF membrane made it more oxygen permeable so that a change from surface exchange limited to bulk diffusion limited happened at low temperature. In the case of this LCF membrane, the change in apparent energy was not observed, which indicated that the rate limiting mechanism didn't change over the temperature range tested. Tsipis et al[105] tested a 1mm thick $La_{0.3}Sr_{0.7}FeO_{3-\delta}$ membrane and found that the activation energy was around 75kJ/mol. Another disk membrane was tested by Tsai et al in a similar button cell reactor. The membrane was $La_{0.4}Ca_{0.6}Fe_{0.8}Co_{0.2}O_{3-\delta}$, with 0.55mm thickness. The apparent activation energy under air oxygen permeation was about 95kJ/mol. Thus the 98-139kJ/mol apparent activation energy found for the 0.89mm $La_{0.9}Ca_{0.1}FeO_{3-\delta}$ (LCF) membrane in this thesis is consistent with similar membranes. The Ca substitute of La and the lack of Sr and Co make the LCF membrane less active.

The apparent activation energy is a useful parameter for understanding the general permeation property of the perovskite membranes. However, to fully apprehend the characteristics of the membrane, one has to understand the mechanism of oxygen permeation. The transport of oxygen through the membrane can be divided into five steps:

1. Mass transport to the membrane surface.

2. Oxygen surface exchange on the feed side.

3. Oxygen ion diffusion through the membrane via oxygen lattice vacancies in the membrane.

4. Oxygen surface exchange on the sweep side.

5. Mass transport away from the membrane.

Depending on the membrane thickness, operating temperature, gas flow rates and membrane reactivity, every step above can be the rate limiting step. In many researches, the flow rates of gases are set up so that the step 1 and step 5 are not the rate limiting steps. In that case, the surface exchange rates and the oxygen diffusivity become the critical properties. The critical thickness L_c is the thickness where the change from diffusion limited to surface exchange limited happens as the membrane thickness decreases. In the case of diffusion

limited oxygen permeation, the traditional way of describing the mechanism is through Wagner's Equations:

$$J_{O2} = \frac{RT}{4^2F^2L}\left(\frac{\sigma_i\sigma_e}{\sigma_i+\sigma_e}\right) In(\frac{P'_{O2}}{P''_{O2}}) \quad (4\text{-}2)$$

Where F is Faraday constant, L is the membrane thickness, σ_i and σ_e are ionic and electronic conductivity respectively, and P'_{O2} and P''_{O2} represent feed side and sweep side oxygen partial pressures respectively. In Eq. (4-2), the electronic and ionic conductivities are both temperature dependent, following the empirical formula in Eq. (4-1). This equation simply assumes that the oxygen permeation through the membrane is diffusion limited, and does not take into account the surface exchange limits. To account for surface exchange limitations, a modified Wagner's equation can be used:

$$J_{O2} = \frac{1}{1+(\frac{2L_c}{L})}\frac{RT}{4^2F^2L}\left(\frac{\sigma_i\sigma_e}{\sigma_i+\sigma_e}\right) In(\frac{P'_{O2}}{P''_{O2}}) \quad (4\text{-}3)$$

Here L_c, the critical thickness, can be calculated from the following equation:

$$L_c = \frac{D_v}{K_s} \quad (4\text{-}4)$$

The D_v and K_s in Eq. (4-4) are bulk diffusion coefficient and equilibrium constant of surface exchange respectively. Both D_v and K_s are temperature dependent, following the same form in Eq. (4-1). That is why the oxygen permeation rate can be expressed by Equation (4-1) through apparent activation energy E_a and pre-exponential factor.

However, Eq. (4-3) is an over-simplified use of Wagner equation, which does not take into account the different surface exchange rates on either side of the membrane, and considers surface exchange rates only by modifying the overall resistance from bulk diffusion. A more detailed mechanism is needed to predict the membrane characteristics. Xu and Thomson [104] developed a more detailed model to predict the oxygen flux:

$$J_{O2} = \frac{D_v k_r (P'^{0.5}_{O2} - P''^{0.5}_{O2})}{2Lk_f(P'_{O2}P''_{O2})^{0.5} + D_v(P'^{0.5}_{O2} + P''^{0.5}_{O2})} \quad (4\text{-}5)$$

Where D_v, k_f, k_r are diffusion coefficient, reverse surface reaction rate and forward surface reaction rate respectively. All three of the parameters D_v, k_f and k_r are temperature dependent and follow the Arrhenius equation in Eq(4-1). The partial pressures in the equation, P'_{O2} and P''_{O2}, are local oxygen partial pressures at the feed and sweep side membrane surfaces respectively. The equation can also be written in the following form:

$$J_{o2} = \frac{(\frac{k_r}{k_f})(P_{O2}''^{-0.5} - P_{O2}'^{-0.5})}{\left(\frac{1}{K_{ex}^{sweep}}\right)+\left(\frac{2L}{D_v}\right)+\left(\frac{1}{K_{ex}^{feed}}\right)} = \frac{K(P_{O2}''^{-0.5} - P_{O2}'^{-0.5})}{R_{ex}''+R_d+R_{ex}'} \quad (4\text{-}6)$$

$$K_{ex}^{swep} = k_f\sqrt{P_{O2}''} \quad (4\text{-}6b)$$

$$K_{ex}^{feed} = k_f\sqrt{P_{O2}'} \quad (4\text{-}6b)$$

Notice that in Eq.(4-6), the three terms in the denominator $\frac{1}{K_{ex}^{sweep}}$, $\frac{2L}{D_v}$ and $\frac{1}{K_{ex}^{feed}}$ correspond to surface exchange resistance on the sweep side R_{ex}'', bulk diffusion resistance R_d and surface exchange resistance on the feed side R_{ex}' respectively. This expression does not ignore the mass transport resistances in step 1 and step 5 by using only P_{O2}' and P_{O2}'', the local oxygen partial pressures at the membrane surfaces. Thus in order to find the values of k_f, k_r and D_v, one needs to find the local partial pressures P_{O2}' and P_{O2}'' from the measurements of the bulk partial pressures P_{O2_b}' and P_{O2_b}''.

In the oxygen permeating experiments, 90sccm air is used as the feed gas which is equivalent to 19sccm oxygen flow rate if 0.21atm oxygen partial pressure is assumed. This is equivalent to 12μmol/s/cm^2 oxygen flux flowing to the feed side, about 1000 times of the oxygen permeation flux. Thus the mass transport of oxygen from the feed side bulk to the feed side surface can be assumed fast enough so that $P_{O2\_b}' \approx P_{O2}'$.

The oxygen partial pressure on the sweep side cannot be found directly since the GC only measures the oxygen partial pressure in the bulk gas. One way to find the P_{O2}'' value is to find the correlation between the P_{O2_b}'' and P_{O2}'' by simulating the flow field. One can also approximate the P_{O2}'' value by finding the mass transfer coefficient g_m so that the following equation can be solved:

$$J_{O2\_m} = g_m(m_{O2}'' - m_{O2\_b}'') \quad (4\text{-}7)$$

Where J_{O2_m} is the oxygen flux in kg/s/m^2, g_m is the mass transfer coefficient in kg/s/m^2, m_{O2}'' and m_{O2_b}'' are mass fractions of oxygen at the membrane sweep side surface and in the outlet sweep gas bulk respectively. The mass transfer under the stagnation flow is analogous to the heat transfer under the same conditions if the following equation is satisfied according to Lienhard and Lienhard [109]:

$$B_m = \frac{m_{O2}'' - m_{O2\_b}''}{1 - m_{O2}''} \leq 0.2 \quad (4\text{-}8)$$

Where B_m is the dimensionless factor describing the driving force of mass transfer.

Following the analogy, the correlations for heat transfer under stagnation flow can be used for mass transfer to obtain the g_m value. According to the analogy, the Nusselt number Nu can be replaced by Nu_m:

$$Nu_m = \frac{g_m d}{\rho D_{12}} \tag{4-9}$$

ρ is the average density of the mixture at the operating temperature, which is approximately the density of He because the mass fraction of O_2 is only about 0.0001~0.001. The characteristic length $d = \frac{D_t + D_c}{2}$ is the average of the feed tube diameter and the alumina chamber diameter as depicted in Figure 4-11. D_{12} is the diffusivity of O_2 in He at the operation temperature.

The heat transfer under an axisymmetric jet at the stagnation point can be estimated by the following empirical relation:

$$Nu = 0.753 Re_d^{1/2} Pr^{1/3} \tag{4-10}$$

The Prandtl number Pr can be replaced by Schmidt number Sc using the mass transfer analogy:

$$\mathrm{Sc} = \frac{\nu}{D_{12}} \tag{4-11}$$

Here ν is the kinematic viscosity of helium at the operating temperature.

Eq. (4-10) is used to find the following relation for mass transfer:

$$Nu_m = 0.753 Re_d^{1/2} Sc^{1/3} \tag{4-12}$$

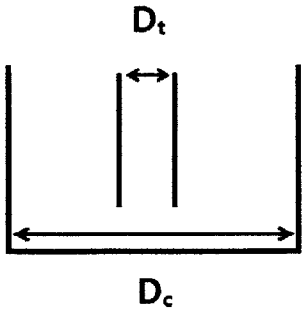

Figure 4-11. Inner diameters of the inlet tube and the chamber

Using Eq.(4-7) and Eq.(4-12) the oxygen partial pressures at the membrane can be estimated from the bulk pressures measured from the sweep gas outlet. Table 4-2 shows the results of the calculation. The membrane was tested at 900°C and 990°C with 90sccm air on the feed side and varying He flow rate on the sweep side. In the table, P''_{O2} decreases as the sweep gas flow rate increases because of increased mass transfer. On the other hand, the oxygen flux J_{o2} increases with increasing sweep gas flow rate (Fig. 4-13). This is also shown in the simulations done by Hong et al [110]. In Hong's work, a numerical model was used to simulate the mass transfer of oxygen near a 1mm thick disk OTM in a stagnation flow reactor. The J_{o2} was calculated based on Eq. (4-5). The simulation created a profile of the oxygen partial pressures on each side of the membrane. Figure 4-12 shows the results of the simulation varying the sweep gas flow rate while maintaining the feed gas flow rate and membrane temperature. In the Figure, P_{O2} corresponds gas phase oxygen partial pressure, H is the distance between the membrane surface and the gas inlet tube and y corresponds to the distances to the membrane surface. The subscripts "feed" and "sweep" correspond to the feed side and the sweep side respectively. The sweep side oxygen partial pressure profile shows that as the sweep gas flow rate increases, the oxygen partial pressure at the surface decreases. Meanwhile, the oxygen partial pressure gradient $\frac{\partial P_{O2\_sweep}}{\partial y}$ at the surface increases as the sweep gas flow rate increases, as shown by the slops of the plots near y_{sweep}=0. Thus in Figure 4-13, although the difference between the local and bulk oxygen partial pressures $P''_{O2} - P''_{O2\_b}$ decreases as the sweep flow rate increases, the oxygen flux J_{o2} still increases, because the oxygen partial pressure gradient $\frac{\partial P_{O2\_sweep}}{\partial y}$ can still be increasing at the sweep side surface, as shown in by the numerical model. The increase in mass transfer overcomes the increase in oxygen flux and makes $P''_{O2} - P''_{O2\_b}$ smaller at higher sweep gas flow rates.

From the results in table 4-2, one can see that the mass transfer does play a role in the oxygen transport so that there is an oxygen partial pressure gradient between the bulk sweep gas and the membrane surface. However, this partial pressure difference is small compared to the partial pressure difference across the membrane. Thus, although the sweep side gas phase mass transfer does play a role in the total oxygen transport resistance, it is not the highest resistance.

Table 4-2. Bulk oxygen partial pressures P''_{O2_b} from measurements and calculated oxygen local pressures P''_{O2}. 90sccm air is used as the feed gas.

	T=990°C			T=900°C		
Q_{He} (sccm)	J_{o2} (μmol/s/cm^2)	P''_{O2_b} (Pa)	P''_{O2} (Pa)	J_{o2} (μmol/s/cm^2)	P''_{O2_b} (Pa)	P''_{O2} (Pa)
400	0.1003	54.46	194.78	0.0518	33.44	107.99
300	0.0882	62.57	205.16	0.0432	36.48	108.29
250	0.0828	69.91	216.55	0.0398	39.92	112.35
200	0.0793	81.82	239.08	0.0359	44.18	117.38
160	0.0696	89.67	243.99	0.0337	50.66	127.44
130	0.0679	106.64	273.96	0.0301	55.93	132.13
100	0.0644	130.45	311.68	0.0283	66.26	147.77
80	0.0602	150.97	340.57	0.0252	72.75	153.94
50	0.0517	206.69	413.30	0.0217	102.13	190.99
20	0.0395	399.20	652.29	0.0159	192.31	295.58

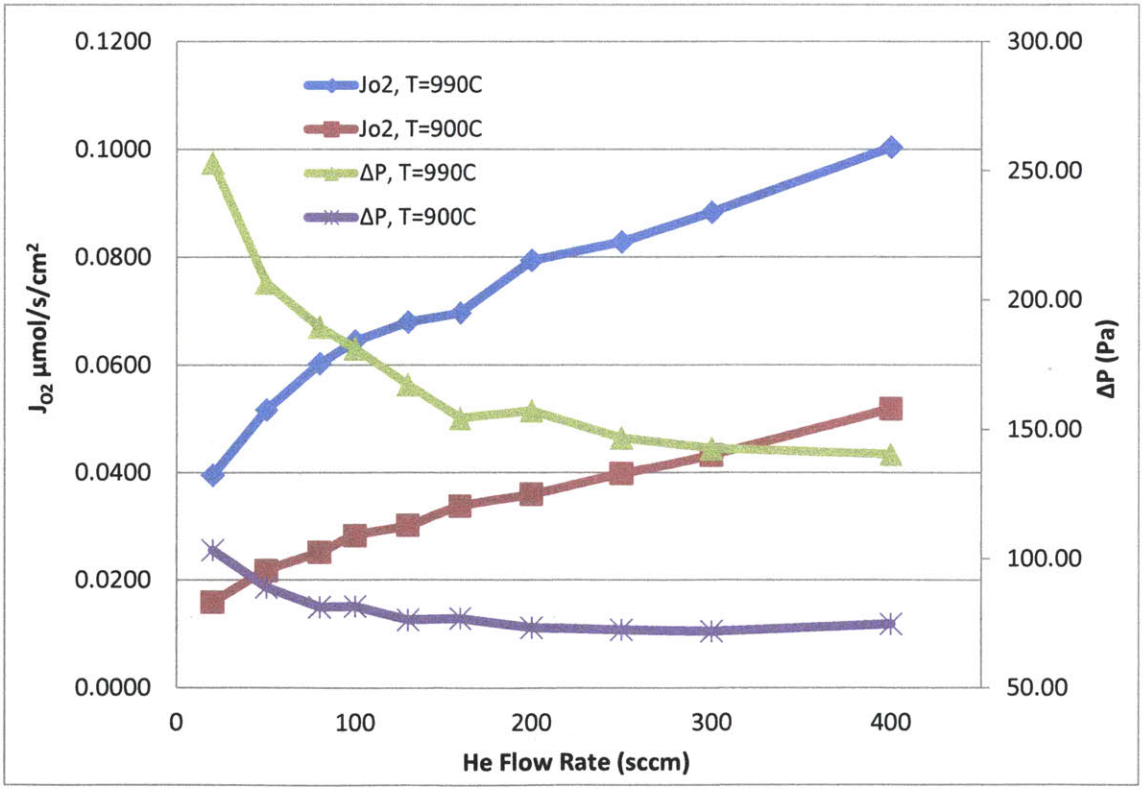

Figure 4-13. Oxygen flux and ΔP under varying He sweep gas flow rate. The feed gas is 90sccm air. ΔP is the difference between local and bulk oxygen partial pressures $P''_{O2} - P''_{O2\_b}$.

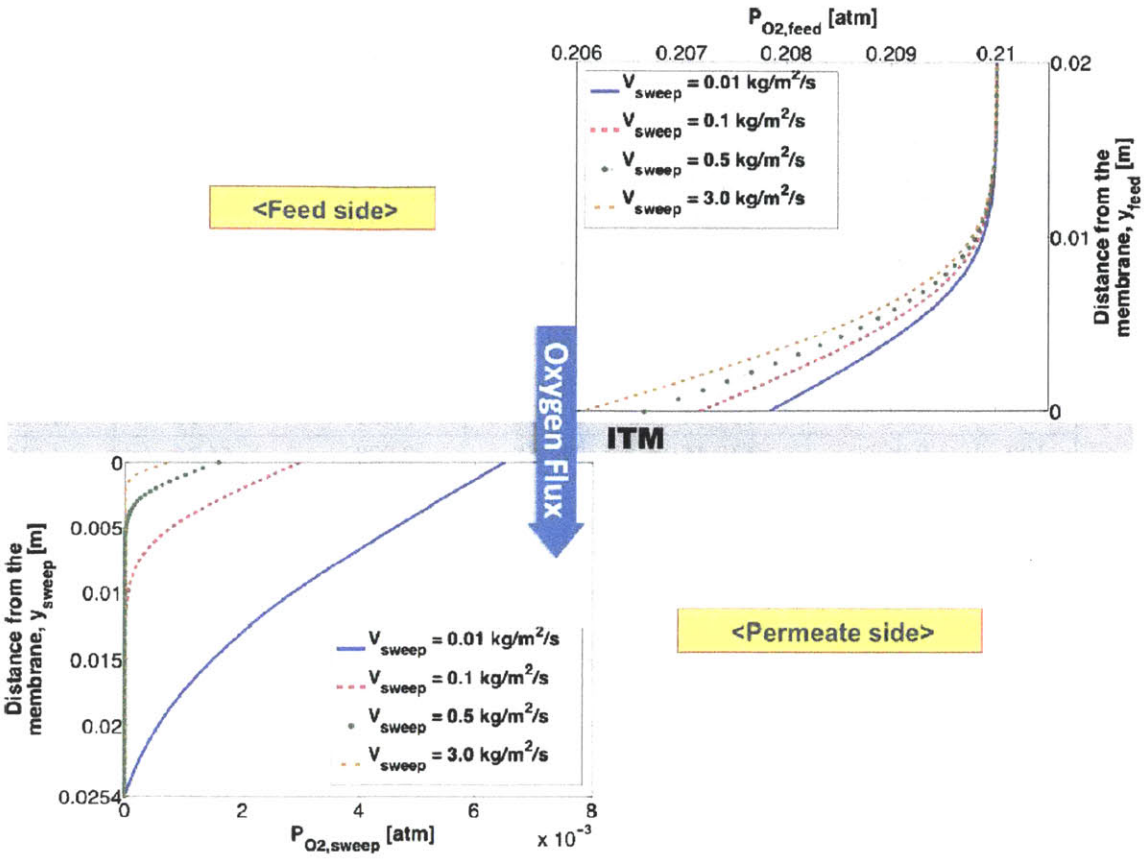

Figure 4-12. Spatially resolved oxygen partial pressure profile as a function of sweep gas flow rate (Hong et al[110]). V_{feed}=0.1kg/m^2/s, T=1100K, L=1mm H_{feed}=50.8mm, H_{sweep}=25.4mm.

The remaining three most important rate limiting steps are the surface oxygen surface exchange on the feed side, the bulk diffusion and the oxygen surface exchange on the sweep side. The surface exchange resistance on the feed side is unlikely to be the rate limiting step as $R'_{ex} = \frac{1}{k_f\sqrt{P'_{O2}}}$ is at least 7 times smaller than the surface exchange resistance on the sweep side $R''_{ex} = \frac{1}{k_f\sqrt{P''_{O2}}}$ because $P'_{O2} \approx 21200$ Pa and $P''_{O2} \approx 50\sim467$Pa. Thus, the remaining rate limiting steps to be considered are bulk diffusion and sweep side oxygen surface exchange. In the bulk diffusion limited case, Eq.(4.6) can be expressed as:

$$J_{O2} = \frac{D_V k_r (P''^{-0.5}_{O2} - P'^{-0.5}_{O2})}{2Lk_f} \quad (4\text{-}13)$$

And in the sweep side surface exchange limited case, the oxygen flux becomes

$$J_{O2} = k_r[1 - \left(\frac{P''_{O2}}{P'_{O2}}\right)^{0.5}] \quad (4\text{-}14)$$

Figure 4-13 shows the oxygen flux of the data listed in Table 4-2 over He flow rate. As the He flow rate increases, the oxygen flux also increases. The increasing sweep gas flow rate decreases the oxygen partial pressure on the sweep side, as shown in Table 4-2, thus increases the oxygen partial pressure gradient across the membrane. To examine the rate limiting step of the oxygen permeation, the estimated P''_{O2} listed in Table 4-2 and the feed side partial pressure P'_{O2}≈0.21atm are used to fit the Eq. (4-13) and Eq.(4-14). Figure 4-14 shows the oxygen flux plotted against the partial pressure difference $P''^{-0.5}_{O2} - P'^{-0.5}_{O2}$. J_{O2} and $P''^{-0.5}_{O2} - P'^{-0.5}_{O2}$ show a linear relation with coefficient of determinations R^2 equals 0.89 and 0.75 at 990°C and 900°C respectively. On the other hand, Figure 4-15 shows that the attempt to fit J_{O2} with $[1 - \left(\frac{P''_{O2}}{P'_{O2}}\right)^{0.5}]$ according to the surface exchange limited equation gives meaningless fittings. The results of Figure 4-14 and 4-15 show that the oxygen permeation through the membrane is mainly controlled by the bulk diffusion resistance when He is used as the sweep gas. The fact that R^2 is higher when temperature is at 990°C indicates that the oxygen permeation follows Eq.(4-13) more closely at higher temperatures. Thus at higher temperature, the bulk diffusion is more important.

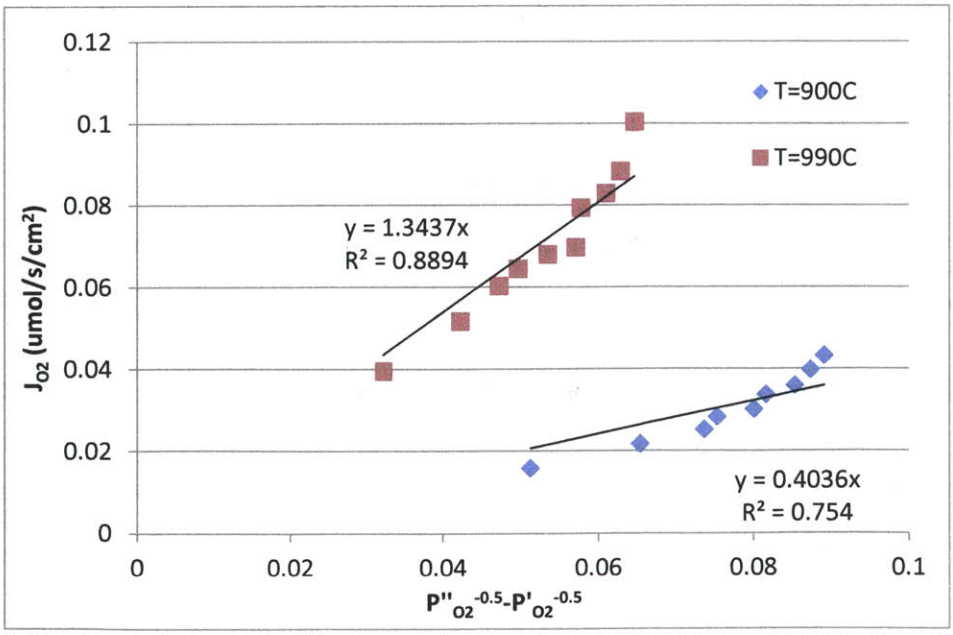

Figure 4-14. Oxygen flux v.s. $P''^{-0.5}_{O2} - P'^{0.5}_{O2}$. The feed gas is 90sccm air.

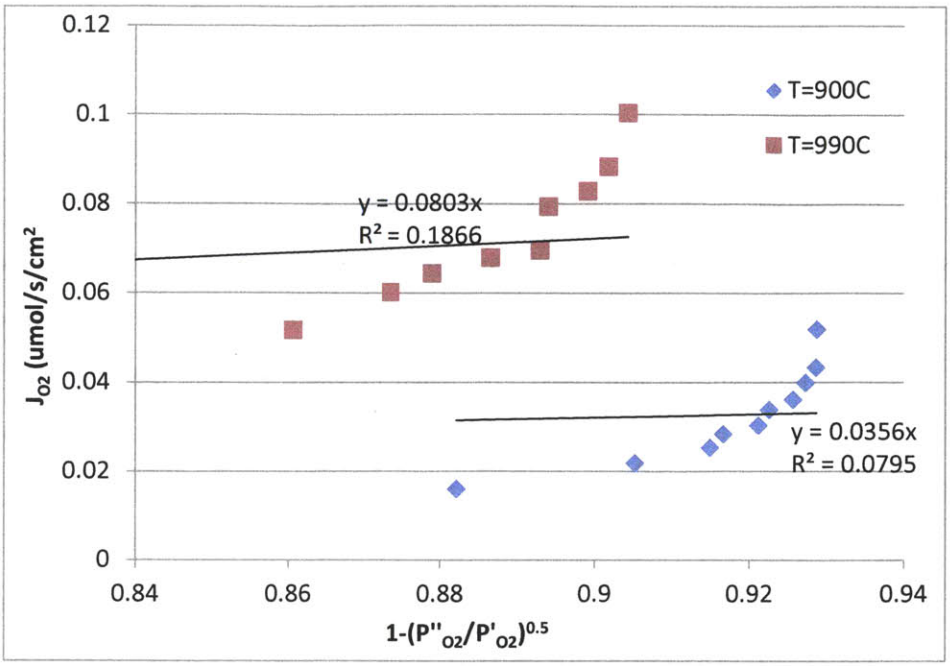

Figure 4-15. Oxygen flux v.s. $[1-\left(\frac{P''_{O2}}{P'_{O2}}\right)^{0.5}]$. The feed gas is 90sccm air.

The temperature dependence of D_v of the LCF membrane is given by Air Products®, thus the D_v values at each temperature can be calculated as shown in Table 4-3. To estimate k_r and k_f at a constant temperature, one can start from an initial guess of the two values. Then the estimated values of J_{O2} can be found using Eq.(4-5) by plugging in the values of L, D_v, P''_{O2} and P'_{O2}. The initial guess of k_r and k_f can then be adjusted continuously until finding values of the estimated J_{O2} that's closest to the measured values of J_{O2}. Shown in Table 4-3 are the k_r and k_f values estimated with the above-mentioned method using Matlab. By using Eq (4-6), one can calculate the resistances of the membrane oxygen transport. The diffusion resistance $R_d = \frac{2L}{D_v}$ is in the range of $10400\sim16000 s/cm$ while the sweep side surface exchange resistance $R''_{ex} = \frac{1}{k_f\sqrt{P''_{O2}}}$ is in the range of $500\sim1000 s/cm$.

Thus the data shows that the diffusion resistance is indeed the dominant resistance when He is used as the sweep gas.

Table 4-3 D_v, k_r, k_f values under different temperatures of the experiment. Feed gas is 90sccm air, sweep gas is 20-400sccm He.

	T=990°C	T=900°C
D_v (cm^2/s)	1.71E-5	1.10E-5
k_r ($mol/s/cm^2$)	1.61E-6	5.94E-7
k_f (cm/s)	0.034	0.027

CO_2 has also been used as the sweep gas. Figure 4-16 shows the oxygen flux when CO_2 was used as the sweep gas and the corresponding flux under He sweep flow at different temperatures. The feed gas was as 90sccm air, the flow rates of CO_2 and He varied from 20sccm to 200sccm. One can see that the oxygen flux is much higher when He is used as the sweep gas. Under increasing flow rate, the difference in J_{O2} between the He sweep gas case and CO_2 sweep gas case increases, which means that at higher flow rate, the suppressing effect of CO_2 on the oxygen flux increases. This indicates that change in diffusivity of O_2 in CO_2 is not the main cause of the lowered oxygen flux under CO_2 as sweep gas. Because the resistance in gas phase mass transfer should decrease as the sweep gas flow rate increases. So the difference between the J_{O2} under the two sweep gas cases should decrease with increasing sweep gas flow rate if the change was mainly caused by the gas phase mass transfer. Thus the plots in Figure 4-16 indicate that the increase in gas phase oxygen transport resistance is not the major cause of the decreased flux. Table 4-3 shows the surface partial pressure P''_{O2} estimated using Eq.(4-10). One can see that the difference between the local oxygen partial pressure P''_{O2} and the bulk oxygen partial pressure P''_{O2_b} is larger than that in the He sweep gas case. The larger sweep side gas phase mass transfer resistance is because of the lower diffusivity of O_2 in CO_2. However, as discussed, the gas phase mass transfer resistance is not the most important resistance in the oxygen transportation, and is not the major cause of the reduced oxygen flux, so the resistance of surface exchanges and bulk diffusion also need to be investigated.

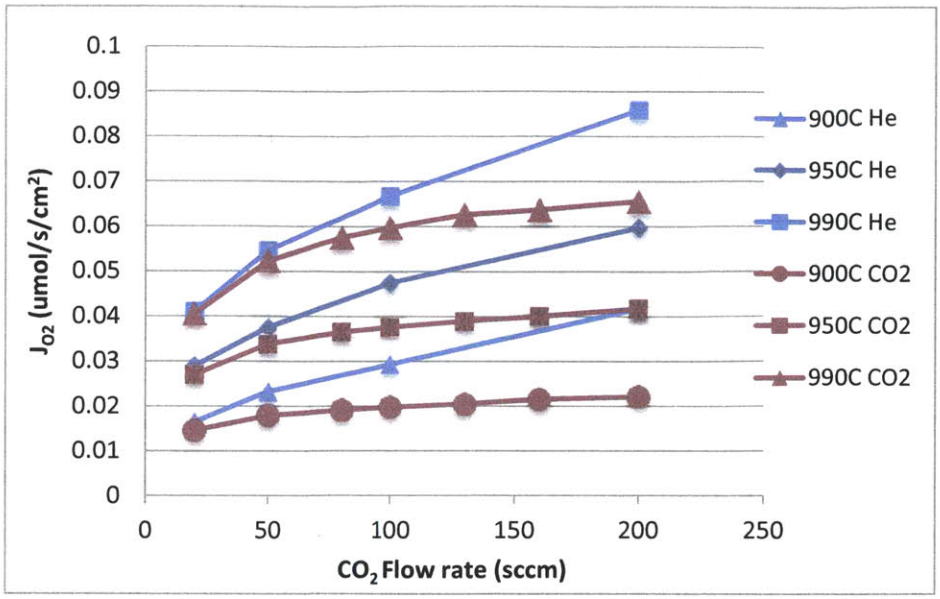

Figure 4-16 Oxygen flux under He and CO_2 sweep flows. The feed gas is 90sccm air.

Table 4-4. The comparison between bulk partial pressure P''_{O2_b} and estimated local partial pressureP''_{O2} . Feed gas Q_{air}=90sccm.

	T=990°C		T=950°C		T=900°C	
Q_{CO2} (sccm)	P''_{O2_b} (Pa)	P''_{O2} (Pa)	P''_{O2_b} (Pa)	P''_{O2} (Pa)	P''_{O2_b} (Pa)	P''_{O2} (Pa)
200	57.20	277.00	56.13	197.89	38.10	114.24
160	69.43	308.06	63.07	215.13	42.55	125.64
130	102.94	363.38	73.15	237.01	47.22	134.68
100	124.42	407.20	86.32	266.81	55.32	151.61
80	147.32	452.00	101.52	297.59	63.83	168.06
50	207.71	557.47	143.67	372.79	88.15	211.72
20	392.87	820.82	275.34	564.03	166.98	326.03

As discussed earlier, the feed side surface exchange resistance is much lower than the sweep side surface exchange resistance because $P'_{O2} \gg P''_{O2}$, thus the feed side surface exchange is not likely the dominating resistance. And because $P'_{O2\_b} \approx P'_{O2}$, the feed side gas phase mass transfer is also not likely to be the dominating resistance. Thus the sweep side surface exchange resistance and the bulk diffusion resistance are the two highest resistances to oxygen permeation. Using the data from Table 4-4, one can plot the J_{O2} v.s. $P''^{-0.5}_{O2} - P'^{-0.5}_{O2}$ curve to determine if the bulk diffusion resistance dominates the oxygen permeation

as expressed in Eq. (4-13). One can also plot the J_{O2} v.s. $[1-\left(\frac{P''_{O2}}{P'_{O2}}\right)^{0.5}]$ curve to determine if the oxygen permeation is sweep side surface exchange resistance dominated as expressed by Eq. (4-14). Figure 4-17 and Figure 4-18 show the above mentioned two plots. As can be seen from the Figures, the attempt to fit the data using Eq.(4-13) and Eq.(4-14) does not give successful fitting. Thus none of the Eq. (4-13) and Eq. (4-14) can be used to describe the oxygen permeation flux using CO_2 as the sweep gas. This indicates that the bulk diffusion resistance and surface exchange resistance have similar magnitudes so that the oxygen permeation is controlled by the joint effect of the two resistances.

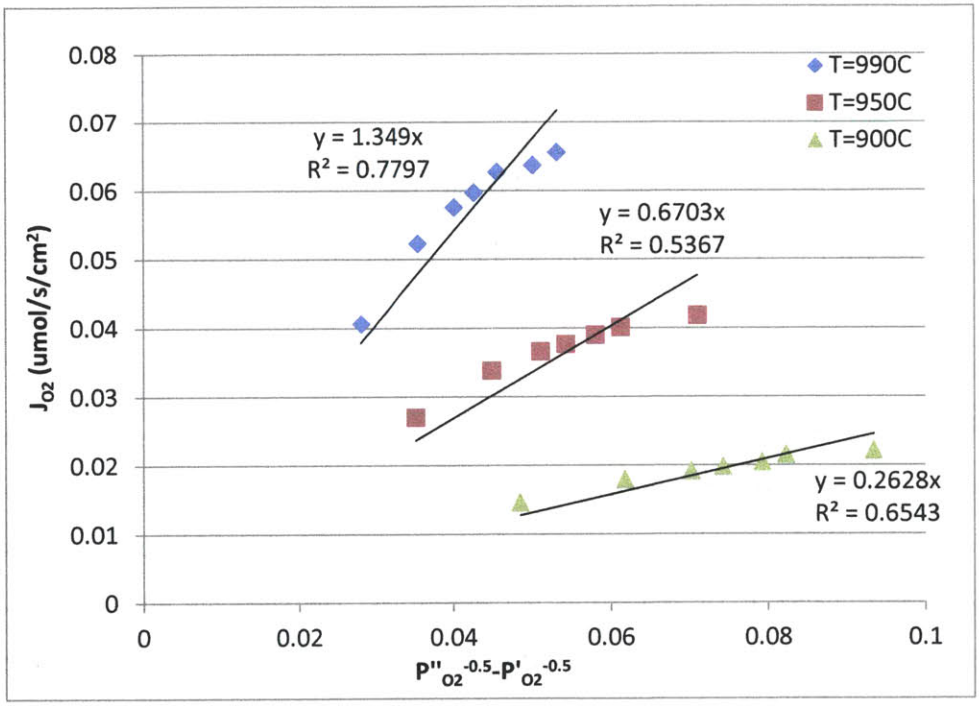

Figure 4-17. The J_{O2} v.s. $P''^{-0.5}_{O2} - P'^{-0.5}_{O2}$. The feed gas is 90sccm air. The sweep gas is CO_2 with varying flow rates.

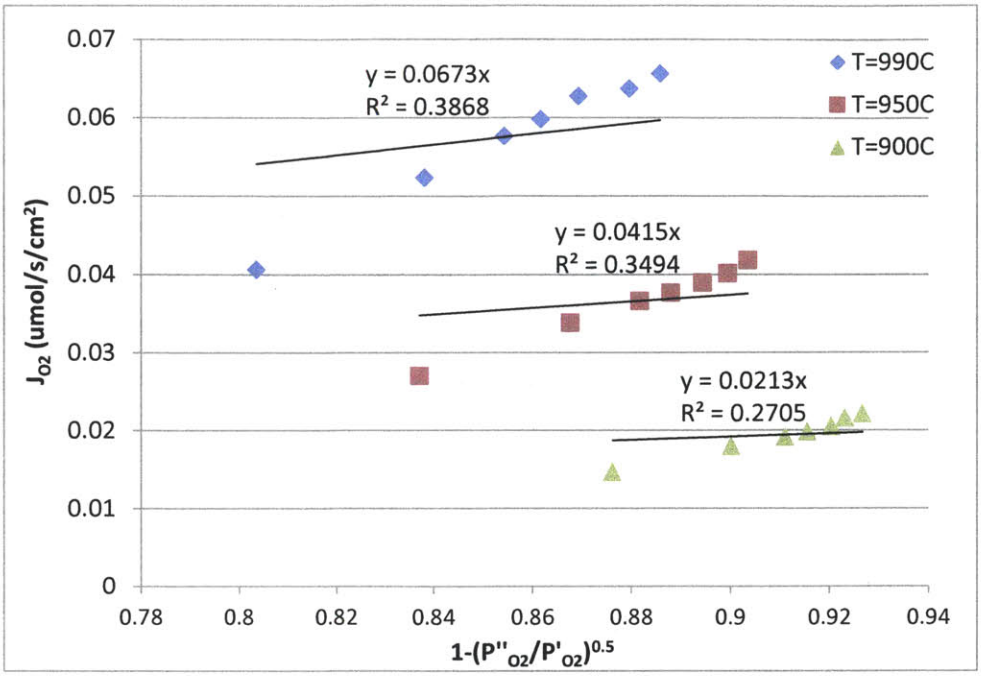

Figure 4-18. J_{O2} v.s. $\left[1-\left(\frac{P''_{O2}}{P'_{O2}}\right)^{0.5}\right]$. The feed gas is 90sccm air. The sweep gas is CO_2 with varying flow rats.

Figure 4-19 shows the oxygen permeation flux in a logarithm scale. One can see that the apparent activation energy changes as the temperature decrease when 100sccm CO_2 is used as the sweep gas and 90sccm air is used as the feed gas. In comparison, the apparent activation energy doesn't change if He is used as the sweep gas. The changing apparent activation energy over the temperature range indicates that the oxygen permeation is dominated by not only one mechanism. This confirms the analysis that the oxygen permeation is controlled by bulk diffusion as well as sweep side surface exchange. At lower temperature, the reaction is increasingly controlled by the sweep side surface exchange reaction so that the difference between the He sweep case and the CO_2 sweep case increases, as shown in Figure 4-16 and Figure 4-19. Compared with He sweep gas case, where bulk diffusion is the major rate limiting step, the sweep side surface exchange resistance increased when CO_2 is used as the sweep gas. The cause of this decreased sweep side surface exchange rate is unknown. One possible explanation is that the oxygen ions from CO_2 occupy the oxygen vacancies and block the permeated oxygen ions.

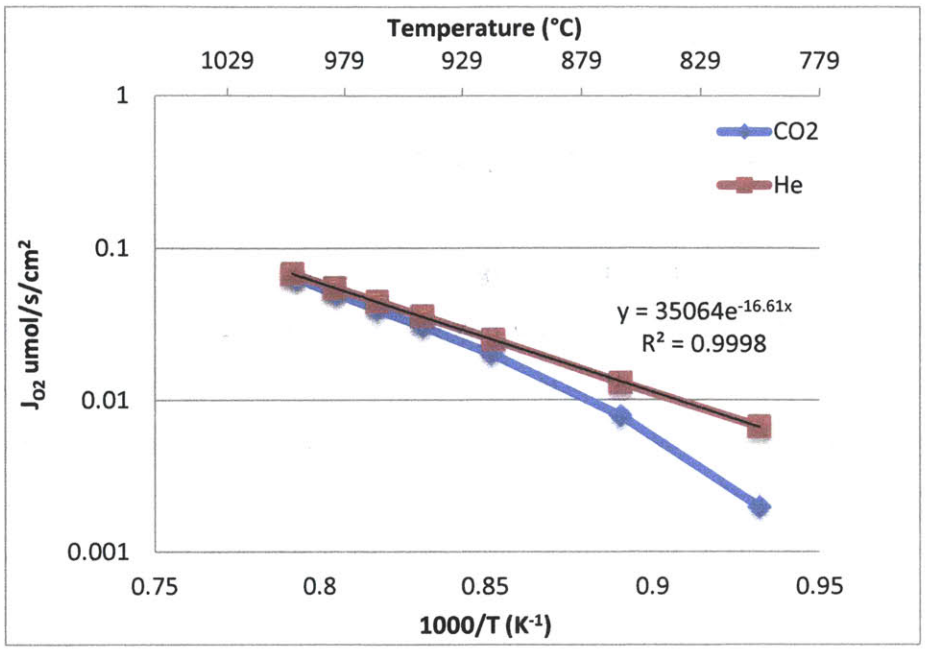

Figure 4-19. Oxygen flux under varying temperature. The feed gas is 90sccm air. The sweep gas is 100sccm CO_2 or He.

Table 4-5. D_v, k_r, k_f values under different temperatures of the experiment. Feed gas is 90sccm air, sweep gas is 20-200sccm CO_2.

	T=990°C	T=950°C	T=900°C
D_v (cm^2/s)	1.71E-5	1.42E-5	1.10E-5
k_r ($mol/s/cm^2$)	3.98E-7	1.34E-7	4.88E-8
k_f (cm/s)	0.0070	0.0031	0.0019

The data in Table 4-5 shows the estimated k_r and k_f values using the data obtained in Figure 4-15. As one can see, the k_r and k_f values obtained from the CO_2 sweep gas case are much lower than those from the He sweep gas case. The values obtained from the fittings of the data are sensitive to errors. More accurate calculations of k_r and k_f can be made if there are more data and more accurate estimations of the local partial pressures. The value of the diffusion resistance $R_d = \frac{2L}{D_v}$ is in the range of $8000\sim10400s/cm$ while the sweep side surface exchange resistance $R''_{ex} = \frac{1}{k_f\sqrt{P''_{O2}}}$ is $2000\sim16000s/cm$. From the comparison between the two resistances, one can see that in the CO_2 sweep gas case, the surface

exchange resistance not only increases but also becomes comparable to the diffusion resistance.

The plot in Figure 4-20 shows the effect of decreased oxygen flux in CO_2 sweep gas is reversible. The experiment was done at 990°C using 90sccm air as the feed gas. 100sccm He was first used as the sweep gas and the oxygen flux was measured. Then the sweep gas was changed to 100sccm CO_2 and the oxygen flux was measured at steady state. After that, the sweep gas was switched back to 100sccm He and the steady state oxygen flux was measured. One can see that the CO_2 sweep gas decreases the oxygen permeation flux, but does not have a permanent effect on the membrane. By switching back to the He sweep gas, the oxygen permeation flux recovered. Note that the large error bar comes from the measurement of J_{O2} using He as the sweep gas after CO_2 was used. The large variation indicates that there is a recovering process of J_{O2} before the oxygen permeation returns to the previous value. Nevertheless, the experiment presented by Figure 4-20 shows that the effect on CO_2 sweep gas is reversible.

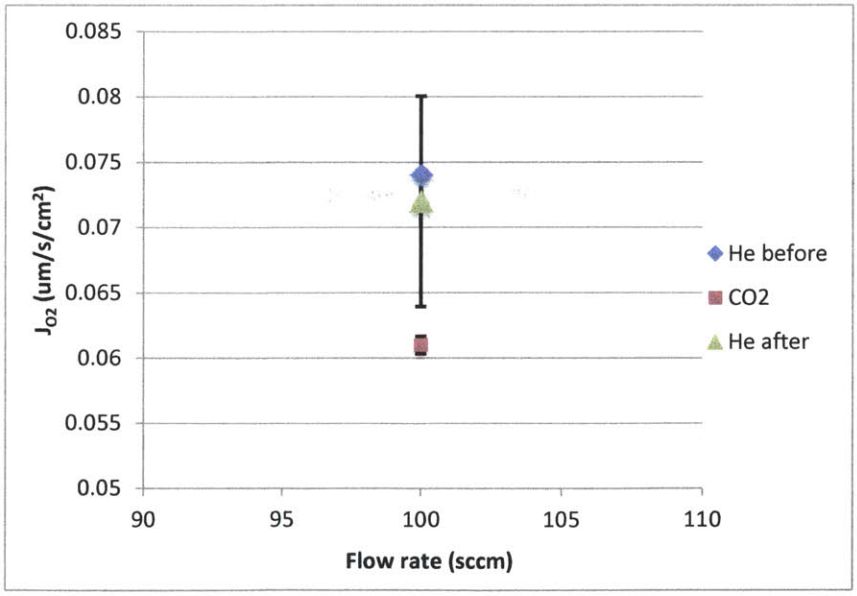

Figure 4-20 Oxygen flux of He and CO_2 sweep. The feed gas is 90sccm air. The sweep gas is100sccm with CO_2 or He. T=990°

4.3 Hydrogen Sweep Experiments

Hydrogen was added to the sweep gas to test the effect of fuel assisted permeation, the reactive case. Figure 4-21 shows the flux of oxygen when hydrogen was used in the sweep gas at 990°C. The feed gas was again 90sccm air. The sweep gas was composed of H_2/Ar at 100sccm with varying hydrogen concentration. The data show an increase in the oxygen flux as the hydrogen concentration increases. As more and more hydrogen is added into the sweep gas, the sweep side oxygen is consumed more and more quickly and the oxygen partial pressure gradient increases. The oxygen flux compared to that in the case of He sweep gas increased by 7-8 times. The highest oxygen flux in He sweep case was 0.072μmo/s/cm^2 at 990°C and 100sccm sweep flow rate while in the case of 100sccm Ar/20vol%H_2 at 990°C the flux increased to 0.54μmo/s/cm^2.

The plot in Figure 4-21 shows the average of two different sets of data taken during different heating cycles. The errors in the data show variations in the reactive experiments. The error increases as the hydrogen concentration increases. This can be explained by the error analysis in section 3.4. The errors are predicted according to section 3.4 and are shown in the Table 4-4. Since for the reactive case, the temperature was not varied during the experiments, the errors mostly come from the GC readings and the calibration of hydrogen. The GC always has a 1% reading error for the hydrogen measurements according to our test, this error contributes to variations in the oxygen flux measurements. The oxygen flux is calculated from the difference of H_2 concentration between the inlet sweep gas and the outlet sweep gas, thus variations in the hydrogen concentration measurements result in variations of the oxygen flux. Nevertheless, as can be seen from Table 4-6, the differences in the oxygen flux obtained from the two heating cycles are within the errors predicted by the analysis.

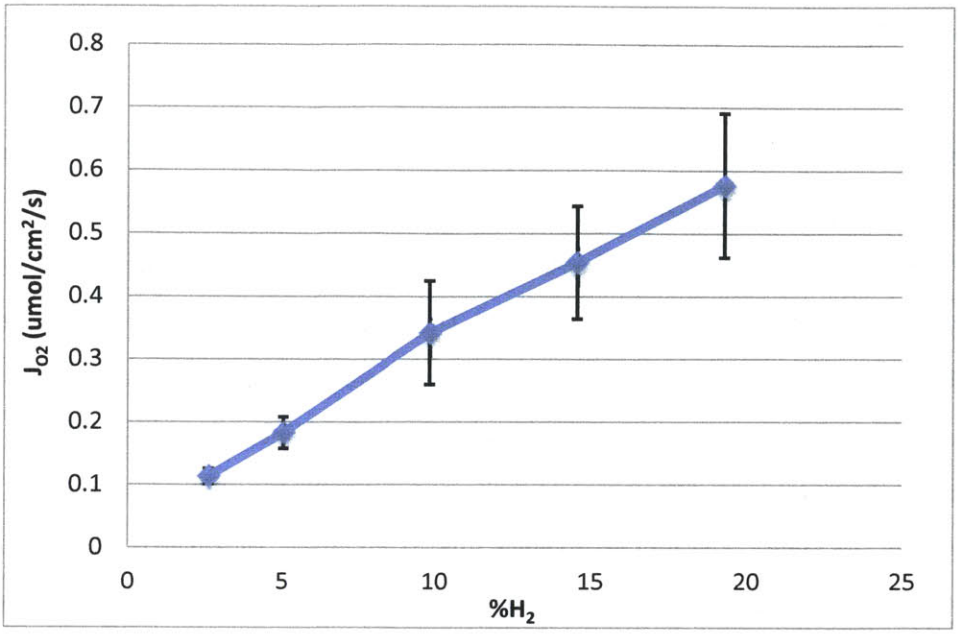

Figure 4-21 Oxygen permeation with varying H_2 concentration. The feed gas is 90sccm air, The sweep gas is 100sccm Ar/H_2 with varying H_2 concentrations. T=990°C.

Table 4-6 Error calculations of the measurements. Feed gas Q_{air}=90sccm, Sweep gas Ar/H_2 Q_{sweep}=100sccm. T=990°C. Data in μmol/s/cm^2

	2.5% H_2	**5% H_2**	**10% H_2**	**15% H_2**	**20% H_2**
$\frac{\partial J_{O2}}{\partial Q} E_Q$	0.0018	0.0036	0.0073	0.0109	0.0145
$\frac{\partial J_{O2}}{\partial C_{O2}} E_{cal}$	0.0073	0.0145	0.0290	0.0436	0.0581
$\frac{\partial J_{O2}}{\partial T} E_T$	Unknown	Unknown	Unknown	Unknown	Unknown
$\frac{\partial J_{O2}}{\partial C_{O2}} E_{reading}$	0.0073	0.0145	0.0290	0.0436	0.0581
Predicted Error	0.0163	0.0327	0.0653	0.0980	0.1307
Error in data	0.0113	0.0249	0.0829	0.0896	0.1145

Figure 4-22 shows the hydrogen conversion ratio at increasing hydrogen concentration. The consumption of hydrogen was calculated according to the difference in hydrogen concentrations at the outlet and inlet sampling points of sweep gas using Eq.(4-15).

$$J_{O2} = \frac{(0.5C_{H2_{i\_sweep}} - 0.5C_{H2_{o\_sweep}} - 0.27C_{N2_{o\_sweep}})Q_{sweep}}{V_{molar}A} \quad (4\text{-}15)$$

Where $C_{H2_{i\_sweep}}$ is the inlet hydrogen concentration, $C_{H2_{o\_sweep}}$ is the outlet hydrogen concentration and $C_{N2_{o\_sweep}}$ is the nitrogen concentration in the sweep gas outlet. It can be seen from the plots that the hydrogen is only partially consumed by the permeated oxygen even at low concentrations. With increasing hydrogen concentration in the sweep side, less percentage of hydrogen is consumed. On the other hand, Figure 4-21 indicates that the absolute amount of hydrogen that reacts with the oxygen increases as the hydrogen concentration increases, according to Eq. (4-15). Thus Figure 4-21 indicates that increasing the hydrogen concentration in the sweep gas increases the oxygen consumption on the membrane sweep side surface. Figure 4-22 indicates that even though the oxygen flux from the membrane increases, the growth in oxygen flux cannot keep up with the increase in hydrogen. The reason is probably low oxygen flux and not enough mixing of the gases on the membrane sweep side.

Nevertheless, the data from hydrogen permeation test show a significant effect of flux increase. The combustion of hydrogen and oxygen on the sweep side increased the oxygen gradient and enhanced the oxygen permeation.

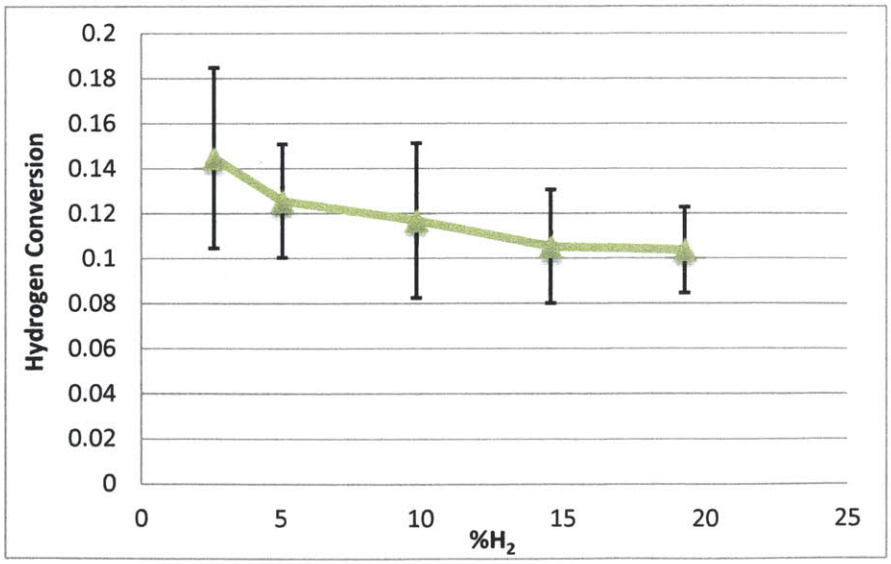

Figure 4-22 Hydrogen conversion with varying concentration. The feed gas is 90sccm air, The sweep gas is 100sccm Ar/H_2 with varying H_2 concentrations. T=990°C.

4.4 Water Splitting Experiments

4.4.1 Ar and Ar/CH_4 sweep gas

Table 4-7 shows the history the membrane used during the water splitting experiments with inert sweep gas and CH_4 reactive sweep gas. The first 20hr was heating up the reactor and establishing the gold ring seal. Then the Ar sweep gas water splitting experiment was conducted, followed by the reactive sweep gas water splitting. Notice that some conditions were tested for more than ten hours because large variation was observed.

Table 4-7. Membrane history

T (°C)	Heating (K/min)	Sweep Side	Feed Side	Duration (hr.)
20-990	3	air-0sccm	air-0sccm	13
990-1030	3	air-0sccm	air-0sccm	1
1030-990	3	Ar-90sccm	He-90sccm	2
990	-	He-100sccm	air-90sscm	5
950	3	He-100sccm	air-90sccm	5
950	-	Ar-400sccm	Ar/50%H_2O-200sccm	4
990	3	Ar-200sccm,400sccm	Ar/50%H_2O-200sccm	21
950	3	Ar-200sccm,400sccm	Ar/50%H_2O-200sccm	4
990	3	Ar-200sscm,400sccm	Ar/50%H_2O-200sccm	24
900	3	Ar-200sccm,400sccm	Ar/50%H_2O-200sccm	18
950	3	Ar-400sccm	Ar/50%H_2O-200sccm	6
990	3	Ar-200sccm,400sccm	Ar/50%H_2O-200sccm	31
950	3	Ar-200sccm	Ar/50%H_2O-200sccm	4
900	3	Ar-200sccm	Ar/50%H_2O-200sccm	16
900		Ar/2.5%CH_4-200sccm	Ar/50%H_2O-200sccm	9
950	3	Ar/2.5%CH_4-200sccm	Ar/50%H_2O-200sccm	3
990	3	Ar-200sccm	Ar-200sccm	9
990	-	Ar/2.5%CH_4-200sccm	Ar/50%H_2O-200sccm	12
			Total	187

Figure 4-23 shows the hydrogen concentration in the feed gas outlet when Ar was used as the sweep gas. The feed gas was 50vol%H_2O and 50vol%Ar at 200sccm total flow rate and the sweep gas was 200sccm or 400sccm Ar. Also shown in the plots are the equilibrium hydrogen concentrations in the feed gas at their corresponding temperatures if no membrane were present. As can be seen from the figure, the hydrogen concentrations during membrane water splitting are 3-4 times higher than those predicted by equilibrium of thermal water dissociation. With higher temperature, the rate of hydrogen production became higher. The fluctuation in the measurements also increased with the temperature. The reason why the fluctuation was higher at higher temperature is not known. Nevertheless, the measurements indicate that oxygen ions from the water splitting reaction moved into the membrane oxygen vacancies, shifting the equilibrium of the water splitting reaction:

$$H_2O(g) + V_o^{oo} + 2e^- \rightarrow O^{2-} + H_2(g) \qquad \Delta H° = 241.82kJ/mol \qquad (4\text{-}16)$$

Where V_o^{oo} represents oxygen vacancy and e^- represents electron. Reaction (4-16) is the overall reaction describing how the water splitting reaction is enhanced by membrane. The details of Reaction (4-16) are still unknown. However, from Figure 4-23, one can rationalize that the water splitting is limiting the reactions on the feed side, since changing the sweep gas flow rate did not have an effect on the hydrogen production rate. Thus the rate limiting step should be the water splitting reaction on the feed side. One possible water splitting mechanism is described by the following two steps:

$$H_2O(g) \rightarrow \frac{1}{2}O_2 + H_2(g) \qquad (4\text{-}17a)$$

$$\frac{1}{2}O_2 + V_o^{oo} + 2e^- \rightarrow O^{2-} \qquad (4\text{-}17b)$$

Alternatively, the direct dissociation of H_2O molecules on the membrane surface could also be the rate limiting step. To determine whether membrane water splitting reaction can be described by equations in Eq. (4-17), one can check the overall reaction rate of the homogeneous reaction in Eq. (4-17a). The reaction rate of O_2 is 4.547E-7μmol/s/cm^3 at 990°C when 50%H_2O/50%Ar is used as the starting gas according to calculations in Cantera. To convert the reaction rate to oxygen flux, the following formula can be used:

$$J_{O2} = \frac{Q_{feed} r_{O2} t_r}{A} \qquad (4\text{-}18)$$

Where J_{O2} is the oxygen flux when (4-17a) is the rate limiting step, Q_{feed} is the flow rate of the feed gas at ambient temperature and atmospheric pressure, r_{O2} is the overall rate of O_2 production, t_r is the residence time of the gases in the reaction zone, A is the effective membrane area. If one assumes that the reaction in Eq. (4-17a) is the rate limiting step, the oxygen flux would be t_r ×0.00000528μmol/s/cm^2 based on the 4.547E-7μmol/s/cm^3 reaction rate. The measured data show that the oxygen flux is about 0.0005μmol/s/cm^2, which means that the residence time needs to be at least 100 seconds if Eq. (4-17a) is the rate-limiting step. At the 200sccm feed gas flow rate, it takes only 3.4s for the gases to flow through the alumina tube reactor chamber. Thus the homogeneous reaction in Eq.(4-17) cannot be the water splitting mechanism during membrane assisted water splitting reactions. The water splitting is assisted by heterogeneous reactions.

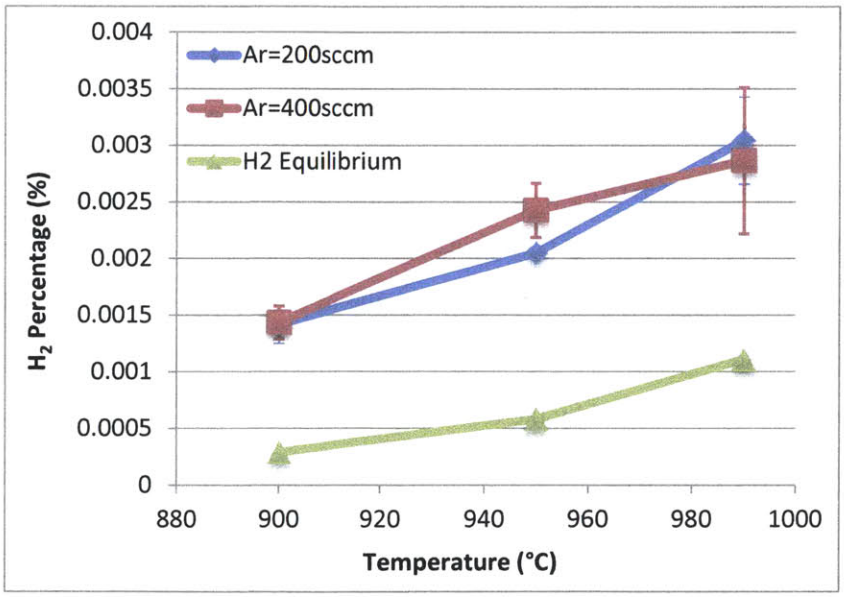

Figure 4-23. Hydrogen concentration during inert sweep water splitting. The feed gas is 50%H_2O/50% Ar at 200sccm. The sweep gas is Ar.

Figure 4-24 shows the comparison between the oxygen flux of water splitting reaction under 200sccm Ar sweep gas, and the oxygen flux during O_2 permeation experiments. During the O_2 permeation experiment, 90sccm air was used as the feed gas and 200sccm He was used as the sweep gas. The apparent activation energy of the water splitting experiment was 103.3kJ/mol while that of the oxygen permeation was 107.6kJ/mol. Although the activation

energies are similar, the pre-exponential factor of water splitting reaction was 142 times smaller than that of the oxygen permeation. During the oxygen permeation reaction, the oxygen molecules from air occupy the surface vacancies of the membrane as described by Eq. (4-17b). But during the water splitting reaction, the oxygen ions must come from water molecules, thus more reaction steps are involved. As discussed above, the water splitting reaction is not limited by the homogenous reaction described in Eq. (4-17a), thus the heterogeneous reactions resulting in water splitting on the membrane surface are the rate limiting steps. The low oxygen flux in the water splitting case is because of the reaction on the feed side surface of the membrane. Unfortunately, one cannot determine from the data of the current experiments the details of the heterogeneous reaction at the membrane surface.

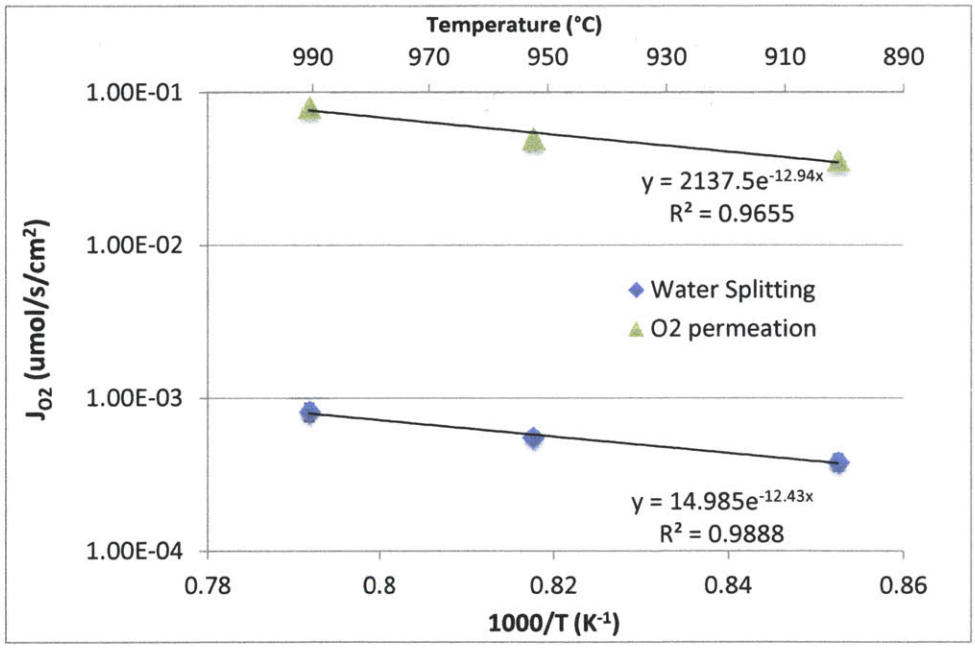

Figure 4-24. A comparison of oxygen flux during water splitting reaction and oxygen permeating reaction. Water splitting: Feed gas= 100sccm Ar/50vol%H_2O. Sweep gas=200sccm Ar; O_2 permeation: Feed gas= 90sccm air, Sweep gas=200sccm He.

The water splitting experiment with reactive sweep gas was conducted with methane in the sweep gas. The feed gas was 200sscm Ar/50vol%H_2O. The sweep gas was 195sccm Ar and 5sccm CH_4. The purpose of adding CH_4 to the sweep side is to let CH_4 react with the permeated oxygen to increase the oxygen gradient across the. A larger oxygen gradient across

the membrane enhances the oxygen transportation and should increase the hydrogen production rate. However, as seen in Figure 4-25, the addition of methane into the sweep gas did not increase the oxygen flux across the membrane. The reaction of methane on the sweep side should decrease the oxygen concentration on the sweep side, which should increase the sweep side surface reaction and the bulk diffusion across the membrane. The fact that the methane in the sweep gas did not increase the hydrogen production rate indicates that the water splitting reaction at the feed side surface may be the rate limiting step. Thus, to increase the hydrogen production rate, the most effective method is to increase the membrane surface area on the feed side or to coat the feed side membrane surface with catalysts. It is also important to decrease the membrane thickness and increase the oxygen permeability of the membrane so that the bulk diffusion of oxygen does not become the rate limiting step. The other possible cause of no flux increase during the reactive sweep gas case is that CH_4 was not ignited during the experiments. In order to find out if that was the case, experiments with more reactive sweep gas like CO should be conducted.

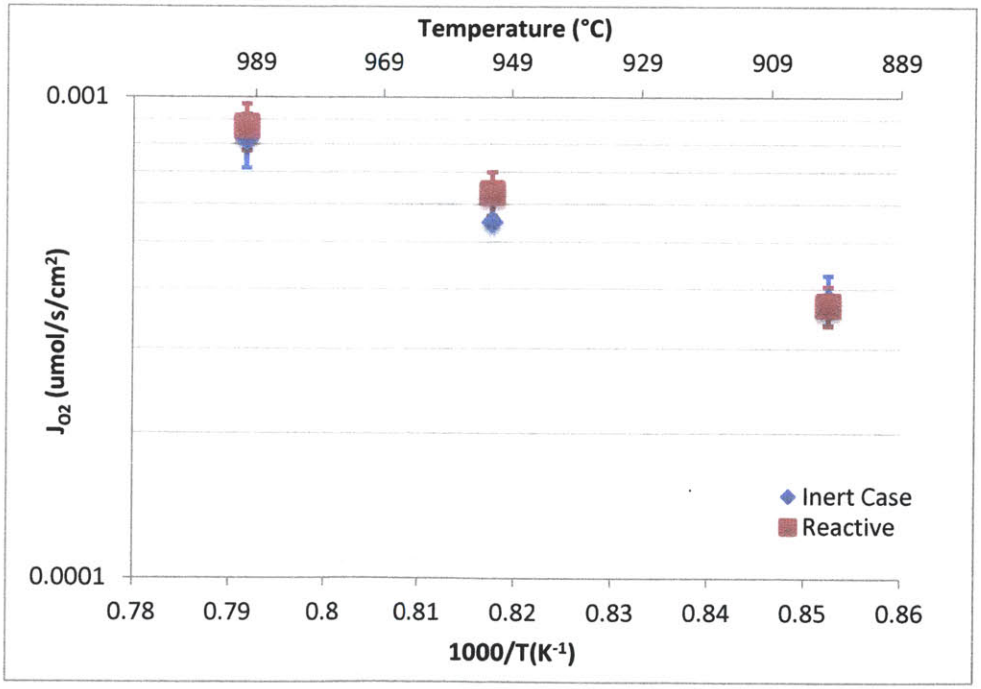

Figure 4-25. A Comparison between reactive sweep gas and inert sweep gas water splitting. The feed gas is 100sccm Ar/50vol%H_2O. The sweep gas in the inert case is 200sccm Ar. The sweep gas in the reactive case is 200sccm Ar/2.5vol%CH_4

4.4.2 He/H_2 sweep gas

To test the effect of a more reactive sweep gas on hydrogen production, H_2 was added to the sweep gas. The experiment was done with 5sccm H_2 and 95sccm He on the sweep side and 5sccm H_2O and 85sccm He on the feed side. The experiment was carried out at 990°C. As can be seen in Figure 4-26, the hydrogen concentration on the feed side of the membrane is plotted against time. At time zero, 5% hydrogen was added to the sweep side without changing the total sweep gas flow rate. The addition of hydrogen to the sweep gas initially increased the rate of hydrogen production. However, after 100min, the membrane started to fail. During the time between 170min and 205min, there was a sudden jump in the hydrogen level on the feed side, indicating a leakage of hydrogen from the sweep side to the feed side. Since there is no way to distinguish between the hydrogen produced from water splitting and the hydrogen leaked from the other side, it is not known how much hydrogen is produced before the membrane breakage. Some hydrogen may have leaked to the membrane feed side from small fractures or imperfect sealing. Another membrane tested at the same condition also failed after the introduction of hydrogen to the sweep gas. The reason behind the membrane failure is investigated in the next section. Imaging methods SEM (scanning electron microscope), XRD (X-ray diffraction) and Auger Electron Spectroscopy were used to examine the reason behind the failure of the membrane.

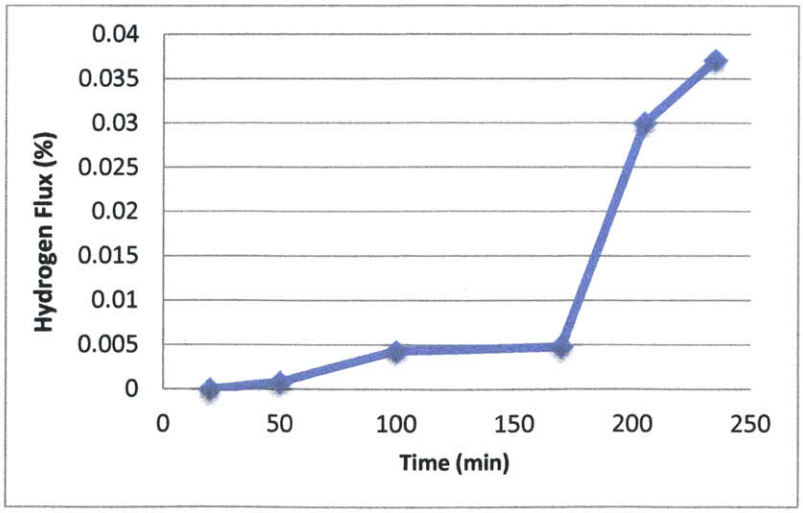

Figure 4-26. The feed side hydrogen concentration v.s. time since hydrogen introduced to the sweep side. The feed gas is 90sccm Ar/5.6vol%H_2O. The sweep gas is 100sccm He/5vol%H_2.

4.5 Post-experiment Investigations

Figure 4-27 shows two pictures of a membrane after the oxygen permeation experiments (experiments in 4.2-4.3). The gold rings were still attached to the membrane, demonstrating a good strength of seal between the membrane and the gold rings. Also the gold rings were obviously compressed under the spring force and the weight of the reactor, indicating that the gold was softened during the high temperature. The area of the membrane inside the gold ring was 12.8mm in diameter after the experiment. The reactor walls have inner radii of 12.7mm, so the effective area was not limited by the gold rings but was limited by the reactor alumina tubes. Also can be seen in the picture is that the membrane surface was clean after the experiment. The oxygen permeation tests done on the membrane include oxygen permeation with inert sweep gases CO_2 and He, and oxygen permeation with hydrogen on the sweep side. The image shows that the oxygen permeation experiments did not cause changes that could be detected by the naked eyes. Further examinations were done using XRD.

Figure 4-27 membrane sweep side (left) and membrane feed side (right). The membrane was used in the inert gas O_2 permeation experiments and the reactive O_2 permeation experiments in sections 4.2~4.3. Membrane tested for 470hr.

Figure 4-28 shows the XRD image of the membrane in Figure 4-27. The XRD of the new membrane show a single phase of $La_{0.9}Ca_{0.1}FeO$ and no other phases. No apparent change to the surface occurred. The XRD images of the sweep side and feed side after the experiment showed the same single phase structure. The Au peaks in the feed side image was due to the diffractions from the gold rings, not diffusion of gold rings into the material. The results of XRD imagines demonstrate that the membrane was stable and not affected by the

hydrogen and CO_2 in the sweep gas during oxygen permeation experiments.

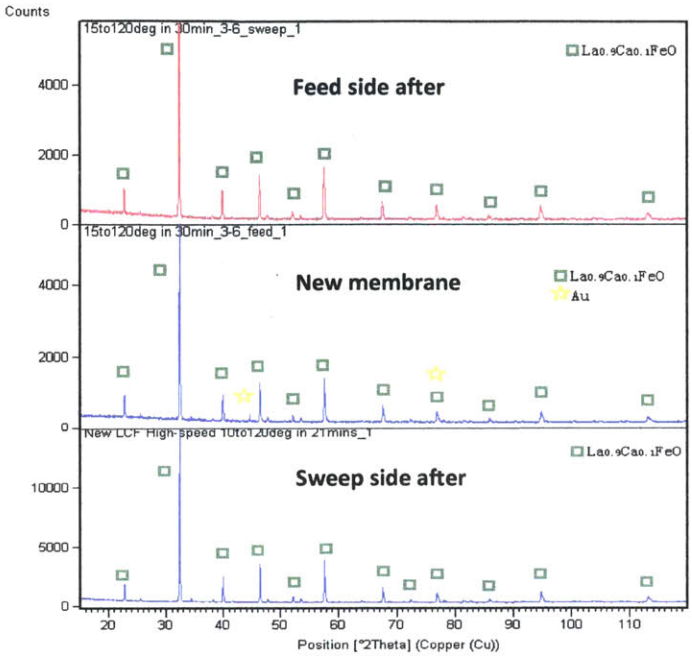

Figure 4-28 XRD imaging of the membrane after oxygen permeation experiments. The membrane was used in the inert gas O_2 permeation experiments and the reactive O_2 permeation experiments in sections 4.2~4.3. Membrane tested for 470hr.

Figure 4-29 and Figure 4-30 are SEM images of the membrane that failed after the hydrogen assisted water splitting experiment (experiments in 4.4.2). Figure 4-29 shows the pictures of the fracture surface. The grain size and structure of the membrane bulk near the surface remained the same on both the feed and the sweep sides of the membrane. The pictures of the surface structure, however, show slight changes in the grains. Figure 4-30 shows three SEM images of the membrane surface. The new membrane surface was smooth and had fine grain structures. However, the feed side and sweep surfaces after the experiment showed rough surface and wavy shape on the grains. Large grains on the surfaces were also observed. The SEM images revealed structural changes on the sweep side and the feed side of the membrane after hydrogen assisted water splitting reaction.

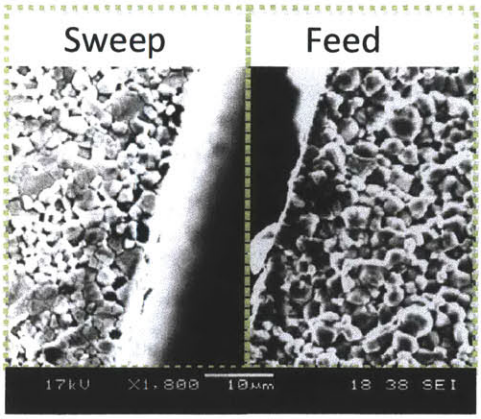

Figure 4-29 SEM of the membrane bulk structure on the failed membrane after the H_2 assisted water splitting experiments. Membrane tested for 260hr.

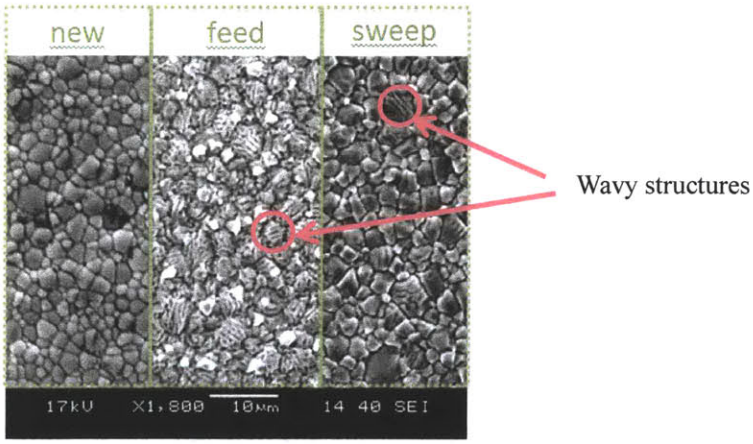

Figure 4-30 SEM imaging of membrane surfaces on the failed membrane after the H_2 assisted water splitting experiments. Membrane tested for 260hr.

In order to further understand the changes on the membrane surface, Auger Electron Spectroscopy was used to analyze the grain compositions. The Auger Electron Spectroscopy is based on the analysis of the electrons emitting from the excited atoms, a phenomenon known as the Auger effect. Figure 4-31 shows the images from the analysis. The spectrums indicate that on the feed side, there is a separation of Fe from La, but on the sweep side, the LCF structure remained intact.

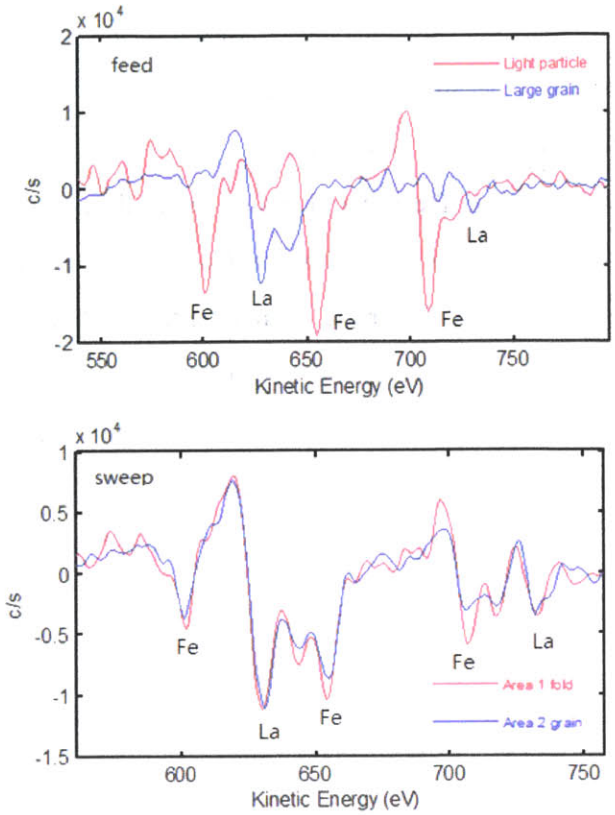

Figure 4-31. Auger Electron Spectroscopy images of membrane feed side surface (top) and sweep side surface (bottom) after the H_2 assisted water splitting experiments using 5.6%H_2/Ar as the sweep gas.

The results in Figure 4-31 show that Fe was separated from the LCF structure on the feed side surface but no structural change occurred on the sweep side. The Fe segregation on the feed side was likely caused by the water vapor in the feed gas combined with the effect of H_2 on the sweep side. However the sweep side of membrane surface did not demonstrate any changes in chemical composition. On the other hand, auger electron microscopy focusing on the wavy structures that were found in the SEM images did show different chemical composition than the other grains. The wavy structures were probably caused by thermal stresses during the heating and cooling between experiments.

The results of the material examination indicate that the Fe containing LCF is not stable under environment of water splitting with H_2 as the sweep gas because of the Fe segregation. The Fe segregation only appeared on the membrane used for reactive water

splitting experiment but not on those used for the reactive oxygen permeating experiments probably because the air provided enough oxygen to protect the membrane from reduction during the oxygen permeating experiments. However, the reason why Fe segregation was found on the water rich side rather than the H_2 rich side, where Fe is more likely to be reduced, is still unknown. On the other hand, the Fe segregation may not have been the only reason for the membrane failure, because the bulk structure was intact after the experiment according to the SEM results, which indicates that the majority of the membrane structure was stable. The failure may have been a combined effect of membrane reduction and heat concentration. To avoid membrane failure, it is recommended that the experiment should be conducted at lower temperature with less reactive fuel such as CO.

Chapter 5. Conclusions and Future Work

In this thesis, a concept of using high temperature ceramic membrane for CO_2 reuse is proposed. The key step in the CO_2 reuse concept is to produce hydrogen by dissociation of H_2O. Since the combustion product of most fuels is CO_2/H_2O, CO_2 can be resued by reacting with the H_2 produced from water splitting.

A review of hydrogen production methods including water splitting and methane reforming is presented. The review shows that although the membrane water splitting is still in its early stage of development, the concept carries three advantages. First, the membrane reactor uses low quality heat as the only energy source, thus it is less expensive than some mature technologies such as electrolysis. Second, the membrane reactor produces hydrogen by shifting the equilibrium of the water splitting reaction, thus the process is not limited by the equilibrium of the reaction. Third, the membrane reactor uses H_2O as the source of hydrogen, which is cheaper and more abundant then CH_4. To further develop the CO_2 reuse concept, careful design and simulation of the membrane reactor reactor need to be conducted.

In the lab, a stagnation flow membrane reactor was constructed to test the 0.89m thick $La_{0.1}Ca_{0.9}FeO_{3-\delta}$ disk membrane. The LCF membrane demonstrated the highest oxygen permeation rate of 0.1μmol/s/cm^2 at 990°C when 400sccm He was used as the sweep gas and 90sccm air was used as the feed gas. The analysis shows that the oxygen permeation is mainly controlled by the bulk diffusion when He is used as the sweep gas. The results also show that the LCF membrane is stable when CO_2 is used as the sweep gas. Although a slight decrease in the oyxgen permeation flux was observed with CO_2 sweep gas, the decrease in the flux is reversible if the sweep gas is switched back to He. As discussed in Chapter 4, the cause of the decreased oxyge flux under CO_2 sweep gas is the increased surface reaction resistance. On the other hand, when H_2 is added to the sweep gas, the oxygen permeation through the membrane increases significantly. The highest flux observed was 0.63μmol/s/cm^2 at 990°C when 90sccm air was used as the feed gas and 100sccm Ar/20vol%H_2 was used as the sweep gas.

The results from the water splitting experiments on the LCF membrane show that H_2 producion from water splitting can be enhanced by the membrane. The hydrogen production

rate found in the experiments was much higher than one would expect from water thermal dissociation. The highest hydrogen production rate was 0.0016μmol/s/cm^2 when 200sccm Ar/50vol%H_2O was used as the feed gas and 200sccm Ar was used as the sweep gas. The change in the sweep gas flow rate did not have a significant effect on the hydrogen production rate during water splitting. The addition of mehane to the sweep gas also did not yield higher hydrogen flux. The results indicate that the water splitting reaction is catalyzed by the membrane surface on the feed side. It is also concluded that the heterogeneous water splitting reaction on the feed side of the membrane is the rate limiting step. Thus improving the reaction on the feed side (water splitting side) by adding catalyst and increasing surface area should increase the rate of hydrogen production.

Water splitting experiments were also done with H_2/He as the sweep gas. It was found that the membrane failed at 990°C when using 90sccm He/5.6vol%H_2O on the feed side and 100sccm He/5vol%H_2 on the sweep side. Investigations on the membrane material change show that the membrane was not damaged on the sweep side where H_2 was introduced, but iron segregation was found on the feed side surface. The cause of iron segregation was likely the low O_2 concentration on the feed side and H_2 on the sweep side, but the mechanism of the change is still unknown. The membrane failure during water splitting experiment using H_2 reactive sweep gas was probably due to the combined effect of heat concentration and stress caused by the material change.

In the future, it is recommended to conduct a water splitting experiment with CO on the sweep side. This experiment should be conducted to examine the effect of sweep gases that are more reactive than CH_4. The use of H_2 in the sweep gas may lead to false measurements of hydrogen production because of possible leakage. It is also recommeded that the reactive water splitting experiments should be conducted at lower temperatures to avoid membrane failure.

To increase the hydrogen production rate, membranes with more reactive material, higher feed side surface area and lower thickness should be used. One recommandation is to use the 200μm thick $La_{0.1}Ca_{0.9}FeO_{3-\delta}$ dense membrane supported on 700μm $La_{0.1}Ca_{0.9}FeO_{3-\delta}$ porous layer. Ru or Ni can be used to coat the porous surface. The higher feed side surface area and the catalysts should enhance the water splitting reaction on the feed side. The lower thickness

is to prevent the bulk diffusion resistance from limiting the hydrogen production rate.

To understand the reaction mechanism of the water splitting on the membrane feed side, simulations of the membrane assisted water splitting reaction should be conducted and compared to the experimental results. One can further understand the mechanism of membrane assisted water splitting by obtaining the diffusivity D_v, and the surface reaction rate constants k_r and k_f of the membrane. Simulations of the water splitting hydrogen production on a commercial scale should also be conducted. The results of the simmulations will be used to set a target hydrogen production rate for the membrane reactors to be cpmmerciallyy viable.

References

[1] AEO2013 Early Release Overview. U.S. Energy Information Administration. 2013

[2] CO_2 Emissions from Fuel Combustion Highlights 2012. International Energy Agency. 2012

[3] Inventory of U.S. Greenhouse Gas Emissions and Sinks 1990-2011. U.S. Environmental Protection Agency. April, 2013

[4] U. Balachandran , T.H. Lee and S.E. Dorris. Hydrogen production by water dissociation using mixed conducting dense ceramic membranes. International Journal of Hydrogen Energy. 2007. 32: 451-456

[5] Heqing Jiang, Fangyi Liang, Oliver Czuprat, Konstantin Efimov, Armin Feldhoff, Steffen Schirrmeister, Thomas Schiestel, and Haihui Wang. Hydrogen Production by Water Dissociation in Surface-Modified $BaCo_xFe_yZr_{1-x-y}O_{3-\delta}$ Hollow-Fiber Membrane Reactor with Improved Oxygen Permeation. Chemistry a Europe Journal. 2010. 16: 7898-7903

[6] A. Evdou, L. Nalbandian, V.T. Zaspalis. Perovskite membrane reactor for continuous and isothermal redox hydrogen production from the dissociation water. Journal of Membrane Science. 2008. 325: 704-711

[7] J. Sunarso, S. Baumann, J. Serra, W. Meulenber, Y. Lin and J.C. da Costa. Mixed ionic-electronic conducting (MIEC) ceramic-based membranes for oxygen separation. Journal of Membrane Science. 2008. 320: 13-41

[8] V.M. Goldschmidt. Geochemische Verterlungsgesetze der Elemente, Norske Videnskap, Oslo, 1927

[9] J.E. ten Elshof, H.j.M Bouwmeester, H. Verweij. Oxidative coupling of methane in a mixed-conducting perovskite membrane reactor. Applied Catalysis A: A General 1995. 130: 195-212

[10] Naitao H, Arashi H. Hydrogen production from direct water splitting at high temperature using a ZrO_2-TiO_2-Y_2O_3 membrane. Solid State Ionics. 1995. 79: 366-70

[11] U. Balachandran, T.H. Lee, S. Wang, S.E. Dorris. Use of mixed conducting membranes to produce hydrogen by water dissociation. International Journal of Hydrogen energy. 2004. 29: 291-296

[12] U. Balachandran, T.H. Lee, S.E. Dorris. Hydrogen production by water dissociation using mixed conducting dense ceramic membranes. Internationa Journal of Hydrogen Energy. 2007. 32: 451-456

[13] A.Evdou, L. Nalbandian, V.T. Zaspalis. Perovskite membrane reactor for continuous and isothermal redox hydrogen production from the dissociation of water. 2008. 325: 704-711

[14] Heqing Jiang, Fangyi Liang, Oliver Czuprat, Konstantin Efimov, Armin Feldhoff, Steffen Schirrmeister, Thomas Schiestel, Haihui Wang, and Jurgen Caro. Hydrogen production by water dissociation in surface-modified $BaCo_xF_yZr_{1-x-y}O_{3-\delta}$ hollow-fiber membrane reactor with improved oxygen permeation. Chemistry a European Journal. 2010.16: 7898-7903

[15] Haibing Wang, Srikanth Gopalan, Uday B. Pal. Hydrogen generation and separation using $Gd_{0.2}Ce_{0.8}O_{1.9-\delta}$ – $Gd_{0.08}Sr_{0.88}Ti_{0.95}Al_{0.05}O_{3\pm\delta}$ mixed ionic and electronic conducting membranes. Electrochemica Ecta. 2011. 56:6989-6996.

[16] Kai Zeng, Dongke Zhang. Recent progress in alkaline water electrolysis for hydrogen production and applications. Progress in Energy and Combustion Science. 2010. 36: 307-326
[17] Alfredo Ursua, Luis M. Gandia, Pablo Sanchis. Hydrogen production from water electrolysis: current status and future trends. Proceedings of the IEEE. 2012. 100
[18] V.M. Rosa, M.B.F. Santos and E.P. Da Silva. New Material for water electrolysis diaphrams. Int. J. Hydrogen Energy. 1994. Int. J. Hydrogen Energy. 1995. 20: 697-700
[19] C. Graves, S. D. Ebbesen, M. Mogensen, K. S. Lackner. Sustainable hydrocarbon fuels by recycling CO2 and H2O with renewable or nuclear energy. 2011. 15: 1-23
[20] P.M. Dieguez, A. Ursua, P. Sanchis, C. Sopena, E. Guelbenzu, L.M. Gandia. Thermal performance of a commercial alkaline water electrolyzer: Experimental study and mathematical modeling. Int. J. Hydrogen Energy. 2008. 33: 7338-7354
[21] R.Rivera-Tionco, C. Mansilla, C. Bouallou. Competitveness of hydrogen production by high temperature electrolysis: Impact of the heat source and identification of key parameters to achieve low production costs. Energy Convers. Manage. 2010. 51: 2623-2634
[22] R. Hino, K. Haga, H. Aita, K. Sekita. R&D on hydrogen production by high-temperature electrolysis of steam. Nuclear Engineering and Design. 2004. 233: 363-375
[23] W. Doenitz, R. Schmidberger, E. Steinheil. Hydrogen production by high temperature electrolysis of water vapour. Int. J. Hydrogen Energy. 1980. 5: 55-63
[24] W. Doenitz, G. Dietrich, E Erdle and S. Streicher. Electrochemical high temperature technology for hydrogen production or direct electricity generation. Int. J. Hydrogen Energy. 1988. 13: 283-287
[25] J.E. O'Brien, C.M. Stoots, J.S. Herring, J. Hartvigsen. Hydrogen production performance of a 10-cell planar solid-oxide electrolysis stack. Journal of fuel cell science and technology. 2006. 3:213-219
[26] A. Brisse, J. Schefold, M. Zahid. High temperature water electrolysis in solid oxide cells. Intl. J. Hydrogen energy. 2008. 33:5375-5382
[27] J. Schefold, A. Brisse, M. Zahid, J.P. Ouweltjes, J.U. Nielsen. Long term testing of short stacks with solid oxide cells for water electrolysis. 2011. 35: 2915-2927
[28] G. Tao, B. Butler, and A. Virkar. Hydrogen and power by fuel-assisted electrolysis using solid oxide fuel cells. Ecs Trans. 2011. 35: 2929-2939
[29] S.D. Kim, J.H. Yu, D.W. Seo, I.S. Hand and S.K. Woo. Hydrogen production by high temperature electrolysis using solid oxide electrolyzer cells. ECS Trans. 2011. 35:2957-2960
[30] R. Xing, Y. Wang, S. Liu, C. Jin. Preparation and characterization of $La_{0.75}Sr_{0.25}Cr_{0.5}Mn_{0.5}O_{3-\delta}$-yttria stabilized zirconia cathode supported solid oxide electrolysis cells for hydrogen generation. J. Power Sources. 2012. 208:276-281
[31] F. Marangio, M. Pagani, M. Santarelli, M. Cali. Concept of a high pressure PEM electrolyser prototype. Intl. J. Hydrogen Energy. 2011. 36: 7807-7815
[32] A. Goni-Urtiaga, D. Presvytes, K. Scott. Solid acids as electrolyte materials for proton exchange membrane (PEM) electrolysis: Review. Intl. J. Hydrogen Energy. 2012. 37: 3358-3372
[33] H. Ito, T. Maeda, A. Nakano, H. Takenaka. Properties of Nafion membranes under PEM water electrolysis conditions. Intl. J. Hydrogen Energy. 2011: 10527-10540
[34] I. Jang, O. Kweon, K. Kim, G. Hwang, S. Moon, A. Kang. Covalently cross-linked sulfonated poly(ether ether ketone)/tungstophosphoric acid composite membranes for water

electrolysis application. Journal of Power Sources. 2008. 181:127-134
[35] R. Kötz and S. Stucki. Oxygen evolution and corrosion on ruthenium-iridium alloys. J. Electrochem. Soc. 1985. 132: 103-107
[36] E. Rasten, G. Hagen, R. Tunold. Electrocatalysis in water electrolysis with solid polymer electrolyte. Electrochimica Acta. 2003. 48: 3945-3952
[37] S. Song, H. Zhang, X. Ma, Z. Shao, R. Baker, B. Yi. Electrochemical investigation of electrocatalysts for the oxygen evolution reaction in PEM water electrolyzers.
[38] A.T. Marshall, S. Sunde, M. Tsypkin, R. Tunold. Performance of a PEM water electrolysis cell using $Ir_xRu_yTa_zO_2$ electrocatalyst for the oxygen evolution electrode. Intl. J. of Hydrogen Energy. 2007. 32: 2320-2324
[39] X. Wu, K. Scott. RuO_2 supported on Sb-doped SnO_2 nanoparticles for polymer electrolyte membrane water electrolysers. Intl. J. Hydrogen Energy. 2011. 36: 5806-5810
[40] K. Kadakia, M. Datta, O. Velikokhatnyi, P. Jampani, S.K. Park, P. Saha, J.A. Poston. Novel (Ir, Sn, Nb)O2 anode electrocatalysts with reduced noble metal content for PEM based water electrolysis. Intl. J. Hydrogen Energy. 2012. 37: 3001-3013
[41] S.A. Grigoriev, P. Millet, V.N. Fateev. Evaluation of carbon-supported Pt and Pd nanoparticles for the hydrogen evolution reaction in PEM water electrolysers. Journal of Power Sources. 2008. 177: 281-285
[42] P. Millet, R. Ngameni, S.A. Grigoriev, N. Mbemba, F. Brisset, A. Banjbari, C. Etiévant. PEM water electrolyzers: From electrocatalysis to stack development. Intl. J. Hydrogen Energy. 2010: 5043-5052.
[43] M. Armandi, D. Drago, M. Pagani, B. Bonelli, M. Santarelli. Direct coupling of H2 production through a high pressure PEM electrolyzer and its storage by physisorption on microporous materials. Intl. J. of Hydrogen Energy. 2012. 37: 1292-1300
[44] P. Medina, M. Santarelli. Analysis of water transport in a high pressure PEM electrolyzer. Intl. J. of Hydrogen. 2010. 35:5173-5186
[45] F. Marangio, M. Pagani, M. Santarelli, M. Calì. Concept of a high pressure PEM electrolyser prototype. Int. J. Hydrogen Energy. 2011. 36: 7807-7815
[46] M.G. Walter, E.L. Warren, J.R. McKone, S.W. Boettcher, Q. Mi, E.A. Santori, NS. Lewis. Solar Water Splitting Cells. Chem. Rev. 2010. 110: 6446-6473
[47] O. Khaselev, A. Bansal, J. A. Turner. High-efficiency integrated multijunction photovoltaic/electrolysis systems for hydrogen production. Int. J. Hydrogen Energy. 2011. 26: 127-132
[48] S. Licht, N. Wang, S. Mukerji, T. Soga, M. Umeno, T. Tributsch. Efficient solar water splitting, Exemplified by RuO2-Catalyzed AlGaAs/Si Photoelectrolysis. J. Phys. Chem. B 2000. 104:8920-8924
[49] Y. Shaban, S.U.M. Khan. Photoelectrolysis of water at second generation carbon modified (CM)-n-Fe_2O_3 films in a photoelectrochemical cell under solar simulated light and sunlight illuminations. Sci. Adv. Mater. 2012. 4: 1947-2935
[50] S.Y. Reece, J.A. Hamel, K. Sung, T.D. Jarvi, A.J. Esswein, J.J.H. Pijpers, D.G. Nocera. Wirless solar water splitting using silicon-based semiconductors and earth-abundant catalysts. Science. 2011. 334: 645-648
[51] N.A. Kelly, T.L. Gibson. Design and characterization of a robust photoelectrochemical device to generate hydrogen using solar water splitting. Int. J. Hydrogen Energy. 2006. 31:

1658-1673
[52] Haihui Wang, Weishen Yang, You Cong, Xuefeng Zhu, Y.S. Lin. Structure and oxygen permeability of a dual-phase membrane. Journal of membrane science. 2003. 224:107-115
[53] C Ting, Z Hailei, X Zhixiang, X Jingcan, X Nansheng. Dense dual-phase oxygen permeation membranes. Progress in chemistry. 2012. 24: 163-172.
[54] Xiaoyao Tan, Nan Liu, Bo Meng, Jaka Sunarso, Kun Zhan, Shaomin Liu. Oxygen permeation behavior of $La_{0.6}Sr_{0.4}CO_{0.8}Fe_{0.2}O_3$ hollow fibre membranes with high concentrated CO_2 exposure. Journal of Membrane Science. 2012. 389: 216-222
[55] M. Schulz, R. Kriegel, A. Kampfer. Assessment of CO_2 stability and oxygen flux of oxygen permeable membranes. Journal of Membrane Science. 2011. 378:10-17
[56] H. Luo, Y. Wei, H. Jiang, W. Yuan, Y. Lv, J. Caro, H. Wang. Performance of a ceramic membrane reactor with high oxygen flux Ta-containing perovskite for the partial oxidation of methane to syngas. Journal of Membrane Science. 2010. 35: 154-160
[57] R. Martinez, E. Romero, C. Guimon, R. Bilbao. CO_2 reforming of methane over coprecipitated Ni-Al catalysts modified with lanthanum. Applied Catalysis A: General, 2004 274: 139 - 149
[58] X, Zhu, P, Huo, Y-P Zhang, D-P Cheng, C-J Liu. Structure and reactivity of plasma treated Ni/Al_2O_3 catalyst for CO_2 reforming of methane. Applied Catalysis B: Environmental. 2008. 81: 132-140
[59] J.R. Rostrupnielsen, J.H.B. Hansen. CO_2-Reforming of Methane over Transition Metals. J. Catal. 1993 44 [1]: 38–49
[60] Z.L. Zhang, V.A. Tsipouriari, A.M. Efstathiou, X.E. Verykios. Reforming of Methane with Carbon Dioxide to Synthesis Gas over Supported Rhodium Catalysts. Journal of Catalysis, 1996 158: 51–63
[61] Eli Ruckenstein, Yun Hang Hu. Role of Support in CO_2 Reforming of CH_4 to Syngas over Ni Catalysts. Journal of Catalysis. 1996. 162: 230–238
[62] S. Yokota, K. Okumura, M. Niwa. Suuport Effect of Metal Oxide on Rh Catalyst in the CH_4-CO_2 reforming reaction. Catalyst letters. 84: 131-134
[63] M.C.J Bradford, M.A. Vannice. CO_2 reforming of CH_4. Catalysis Reviews: Science and Engineering. 41: 1-42
[64] T. Horiuchi, K. Sakuma, T. Fukui, Y. Kubo, T. Osaki, T. Mori. Suppression of Carbon Deposition in the CO_2-reforming of CH_4 by adding basic metal oxides to a Ni/Al_2O_3catalyst. Applied Catalysis A: General 1996. 144: 111-120
[65] M. Masai, H. Kado, A. Miyake, S. Nishiyama, and S. Tsuruya, in Methane Conversion, Elsevier 1988, 67
[66] Y-G Chen, J. Ren. Conversion of Methane and Carbon Dioxide into Synthesis Gas over Alumina-supported Nickel Catalyts. Effec of ni-Al_2O_3 interations. 1994. Catal. Lett. 29: 39-48
[67] M, García-Diéguez, C Herrera, M.A. Larrubia, L.J. Alemany. CO_2-reforming of Natural Gas Components over a Highly Stable and Selective $NiMg/Al_2O_3$ nanocatalyst. Catalysis Today. 2012. 197: 50-57
[68] B. Koubaissy, A. Pietraszek, A.C. Roger, A. Kiennemann. CO_2 reforming of methane over Ce-Zr-Ni-Me mixed catalysts. Catalyst Today 2010. 157:436-439

[69] B. Pawelec, S. Damyanova, K. Arishtirova, J.L.G. Fierro, L. Petrov. Structureal and Surface Features of PtNi Catalysts for Reforming of Methane with CO_2. Applied Catalysis A: General. 2007. 333: 188-200
[70] W. Shen, K. Komatsubara, T. Hagiyama, A. Yoshida, S. Naito. Steam Reforming of Methane over Ordered Mesoporous Ni-Mg-Al oxides. ChemComm. 2009. 6490-6492
[71] B. Sarkar, R. Tiwari, R.K. Singha, S. Suman, et al. Reforming of Methane with CO_2 over Ni Nanoparticle Supported on Mesoporous ZSM-5. Catalysis Today. 2012. 198: 209-214
[72] Y. Takahashi, T. Yamazaki. Behavior of High-pressure CH_4/CO_2 Reforming Reaction over Mesoporous Pt/ZrO_2 Catalyst. Fuel. 2012. 102: 239-246
[73] LL, Xu, HL, Song, LJ, Chou. One-Pot Synthesis of Ordered Mesoporous NiO-CaO-Al_2O_3 Composite Oxides for Catalyzing CO_2 Reforming of CH_4. Acs Catalysis. 2012. 2: 1331-1342.
[74] SG. Liu, LX, Guan, JP, Li, N. Zhao et al. CO_2 Reforming of CH_4 over Stabilized Mesoporous Ni-CaO-ZrO_2 Composites. 2008. 87: 2477-2481.
[75] LL, Xu, HL, Song, LJ, Chou. Mesoporous nanocrystalline ceria-zirconia solid solutions supported nickel based catalysts for CO_2 reforming of CH_4. Int. J. Hydrogen Energy. 2012. 37: 18001-18020
[76] ZJ. Wang, Y. Zhao, L. Cui et al. CO_2 Reforming of Methane over Argon Plasma Reduced Rh/Al_2O_3 Catalyst: a Case Study of Alternative Catalyst Reduction via Non-hydrogen Plasmas. Green Chemistry. 2007. 9: 554-559
[77] S. Shang, GH. Liu, XY. Chai, XM. Tao, X. Li et al. Research on Ni/γ-Al2O3 Catalyst for CO_2 Reforming of CH_4 Prepared by Atmospheric Pressure Glow Discharge Plasma Jet. Catalyst Today. 2009. 148: 268-274
[78] R. Labrecque, J. Lavoie. Dry Reforming of Methane with CO_2 on an Electron-activated Iron Catalytic Bed. Bioresource Technology. 2011. 102: 11244-11248
[79] F. Gallucci, S., A. Basile. Pd-Ag Tubular Membrane Reactors for Methane Dry Reforming: A Reactive Method for CO_2 Consumption and H_2 Production. Journal of Membrane Science. 2008. 317: 96-105
[80] J Galuszka, R.N Pandey, S Ahmed. Methane Conversion to Syngas in a Palladium Membrane Reactor. Catalysis Today.1998. 46 (2 - 3): 83 - 89
[81] A.M. Adris, B.B. Pruden, et al. On the Reported Attempts to Radically Improve the Performance of the Steam Methane Reforming Reactor. The Canadian Journal of Chemical Engineering. 1996. 74.
[82] L. Barelli, G. Bidini, et al. Hydrogen Production through Sorption-enhanced Steam Methane Reforming and Membrane Technology: A Review. Energy. 2008. 33: 554-570
[83] S.O. Choi, S.H. Moon. Performance of $La_{1-x}Ce_xFe_{0.7}Ni_{0.3}O_3$ perovskite catalysts for methane steam reforming. Catalysis Today. 2009. 146. (1 - 2): 148 - 153
[84] Bjørn Christian Enger, Rune Lødeng, John Walmsley, Anders Holmen. Inactive Aluminate Spinels as Precursors for Design of CPO and Reforming Catalysts. Applied Catalysis A: General. 2010. 383 (1-2), 119-127
[85] C.J. Liu, J.Y. Ye, et al. Progresses in the Preparation of Coke Resistant Ni-based Catalyst for Steam and CO_2 Reforming of Methane. ChemCatChem. 2011. 3: 529-541
[86] M.A. Al-Nakoua, M.H. El-Naas. Combined Steam and Dry Reforming of Methane in Narrow Channel Reactors. International Journal of Hydrogen Energy. 2012. 37: 7538-7544

[87] M.A. Soria, C. Mateos-Pedrero, et al. Thermodynamic and Experimental Study of Combined Dry and Steam Reforming of Methane on Ru/ZrO_2-La_2O_3 catalyst at low temperature. International Journal of Hydrogen Energy. 2011. 36: 15212-15220
[88] S.T. Oyama, R. Hacarlioglu, et al. Dry Reforming of Methane Has No Future for Hydrogen Production: Comparison with Steam Reforming at High Pressure in Standard and Membrane Reactors. International Journal of Hydrogen Energy. 2012. 37: 0444-10450
[89] X.D. Peng. Analysis of the Thermal Efficiency Limit of the Steam Methane Reforming Process. Ind. Eng. Chem. Res. 2012, 51, 16385−16392.
[90] M.A. Rosen. Thermodynamic Investigation of Hydrogen Production by Steam-methane Reforming. Int. J. Hydrogen Energy. 1991.16: 207-217.
[91] A.E. Lutz, R.W. Bradshaw, J.O. Keller, D.E. Witmer. Thermodynamic analysis of hydrogen production by steam reforming. International Journal of Hydrogen Energy. 2003. 28:159 – 167
[92] N.D. Mancini, A. Mitsos. Ion Transport Membrane Reactors for Oxy-combustion – Part I: Intermediate – fidelity Modeling. Energy. 2011. 36: 4701-4720
[93] N.D. Mancini, A. Mitsos. Ion Transport Membrane Reactors for Oxy-combution – Part II: Analysis and Comparison of Alternatives. Energy. 2011. 36: 4721-4739
[94] S.G. Sundkvist, S. Julsrud, B. Vigeland, et al. Development and Testing of AZEP Reactor Components. International Journal of Greenhouse Gas Control I. 2007 180-187
[95] L. Pan, S. Wang. A Compact Integrated Fuel-Processing System for Proton Exchange Membrane Fuel Cells. International Journal of Hydrogen Energy. 2006. 31:447-454
[96] J. Han, I-S Kim, K-S Choi. High Purity Hydrogen Generator for on-site Hydrogen Production. International Journal of Hydrogen Energy. 2002. 27:1043-1047
[97] VE Stain, L. Aderson et al. ITM Oxygen Supply: Scaling up Toward Gasification and Energy/Industrial Applications. Air Products and Chemical, Inc. 5th International Freiberg Conference on IGCC & XtL, 2012
[98] S. Tosti, A. Basile, L. Bettinali, et al. Design and Process Study of Pd Membrane Reactors. International Journal of Hydrogen Energy. 2008. 33: 5098-5105
[99] XY. Tan, Z. Wang, B. Meng et al. Pilot-scale Production of Oxygen from Air Using Perovskite Hollow Fiber Membranes. Journal of Membrane Science. 2010. 352:189-196
[100] L. Guczi, G. Stefler, O. Geszti, et al. Methane Dry Reforming with CO_2: A Study on Surface Carbon Species. Applied Catalysis A: General. 2010. 375: 236-246
[101] F.A. Silva, C.E., Hori, A.M. Silva, et al. Hydrogen Production Through CO_2 reforming of CH_4 over $Pt/CeZrO_2/Al_2O_3$ Catalysts Using a Pd-Ag Membrane Reactor. Catalysis Today. 2012. 193: 64-73
[102] WH, Shen. H Momoi, K Komatsubara, et al. Marked Role of Mesopores for the Prevention of Sintering and Carbon Deposition in Dry Reforming of Methane over Ordered mesoporous Mi-Mg-Ag Oxides. Catalysis Today. 2011. 171:150-155
[103] YL Lee, SI Hong, DJ Moon. Studies on the Steam and CO_2 Reforming of Methane for GTL-FPSO Applications. Catalysis Today. 2011. 174: 31-36
[104] S.J.Xu, W.J. Thomson. Oxygen Permeation Rates Through Ion-conducting Perovskite Membranes. Chemical Engineering. 1999. 54:3839-3850
[105] E.V. Tsipis, M.V. Patrakeev, V.V. Kharton et al. Transport Properties and thermal expansion of Ti-substituted $La_{1-x}Sr_xFeO_{3-\delta}$ (x=0.5-0.7). Solid State Sciences. 2005. 7 355-365

[106] Chung-Yi Tsai, Anthoy G. Dixon, Yi Hua Ma et al. Dense Perovskite, $La_{1-x}A'_xFe_{1-y}Co_yO_{3-\delta}$ (A'=Ba, Sr, Ca), Membrane Synthesis, Applications, and Characterization. J. Am. Ceram. Soc. 1998. 81[6]: 1437-1444
[107] K Efimov, T Klande, N Juditzki, A Feldhoff. Ca-containing CO_2-tolerant perovskite materials for oxygen separation. Journal of Membrane Science. 2012. 389:205-215
[108] J.D. Holladay, J. Hu, D.L. King, Y. Wang. A Review of Hydrogen Production Technologies. Catalysis Today. 2009. 139: 244–260
[109] J. Lienhard, J. Lienhard. A Heat Transfer Textbook. . 4th Editoin. Phlogiston Press. 2011
[110] James Hong, Patrick Kirchen, Ahmed F. Ghoniem. Numerical Simulation of Ion Transport Membrane Reactors: Oxygen Permeation and Transport and Fuel Conversion. Journal of Membrane Science. 2012. 407-408:71-85.